High Q^2 Neutral Current interactions at H1 and an extraction of $x\tilde{F}_3$.

by

E.-E. Woehrling

Thesis submitted for a degree of
Doctor of Philosophy

Particle Physics Group,

School of Physics and Astronomy,

The University of Birmingham

September 2004

Abstract

A measurement is presented of the inclusive e^+p neutral current cross section, measured single and double differentially, as a function of Q^2 and Bjorken-x. The data used for this measurement were taken by the HERA detector H1 in the 1999-2000 data-taking period, at a centre of mass energy of $\sqrt{s} = 319$ GeV and corresponding to an integrated luminosity of $\mathcal{L} = 65.2$ pb^{-1}.

An overview of the phenomenology of deep inelastic scattering is given, the experimental apparatus is described and the measurement and analysis procedures are detailed. The neutral current cross section is measured single differentially as a function of Q^2 and x and also double differentially. The cross sections were obtained using an Object Orientated analysis framework and the results were found to be compatible with published data obtained in an independent analysis. The parity violating generalised structure function $x\tilde{F}_3$ is extracted from the measured cross section and compared to the latest published values for the measurement. The analysis results are found to be consistent with the Standard Model expectation, both in terms of QCD and electroweak effects.

In 2002 the HERA accelerator and H1 detector were upgraded. The first data after the upgrade are presented, along with a description of the HERA II data quality efforts.

A note on the author's contribution

The collaborative nature of experimental high-energy physics is such that the work presented in this thesis would not have been possible without the input of many members of the H1 collaboration. Here I would like to acknowledge specific contributions from a number of people. More general acknowledgements can be found at the end of this thesis.

The electron and hadronic calibrations and LAr alignment procedures described in chapter 6 were developed by the Inclusive Measurements and Fits working group. The generic analysis framework was the group effort of the H1UK group, all of whom contributed to the Object Oriented nature of the code. The original framework was designed by Paul Laycock.

I am also grateful to Paul Thompson, Eram Rizvi and Paul Newman for proof-reading all or part of this thesis and for making a number of helpful suggestions.

A note on Units

In this thesis a system of natural units is used, whereby $\hbar = c = 1$

This work was supported financially by the UK Particle Physics and Astronomy Research Council (P.P.A.R.C.), the University of Birmingham and the Council for the Central Laboratory of the Research Councils (C.C.L.R.C.).

"La science a eu de merveilleuses applications, mais la science qui n'aurait en vue que les applications ne serait plus de la science, elle ne serait plus que de la cuisine."
- Jules Henri Poincaré (1854-1912)

"Physics is like sex: sure, it may give some practical results, but that's not why we do it."
- Richard Feynman (1918-1988)

Contents

1 Introduction **1**

2 HERA Physics **3**

2.1 Introduction 3

2.2 Deep Inelastic Scattering 3

2.3 Neutral Current Interactions 4

2.3.1 Low Q^2 Physics 4

2.3.2 High Q^2 Physics 6

2.4 Charged Current Interactions 7

2.5 Neutral Current and Charged Current Structure Functions 8

2.5.1 NC Structure Functions 8

2.5.2 The Measurement of $\tilde{F}_2$ 9

2.5.3 The Measurement of $x\tilde{F}_3$ 9

2.5.4 The $\tilde{F}_L$ Extraction 12

2.5.5 CC Structure Functions 13

2.6 QCD and the DGLAP Evolution 13

3 The H1 Detector **16**

3.1 HERA 16

3.2 H1 18

3.3 Calorimetry in the H1 Detector . . . 21
3.3.1 The Liquid Argon Calorimeter (LAr) . . . 22
3.3.2 The (Backward) Spaghetti Calorimeter (SPACAL) . . . 23
3.3.3 The Instrumented Iron Return Yoke . . . 24
3.3.4 The PLUG Calorimeter . . . 24
3.4 Tracking in the H1 Detector . . . 24
3.4.1 The Central Tracking Detector (CTD) . . . 25
3.4.2 The Forward Tracking Detector (FTD) . . . 26
3.4.3 The Silicon Trackers . . . 26
3.5 The Muon Detectors . . . 27
3.5.1 The Instrumented Iron . . . 27
3.5.2 The Forward Muon Detector . . . 27
3.6 The Luminosity System . . . 27
3.7 The Time-of-Flight System (ToF) . . . 28
3.8 Triggering at H1 . . . 28
3.8.1 The H1 Trigger . . . 28
3.8.2 Trigger Elements Important to the NC Analysis . . . 30

4 Monte Carlo Simulation **33**

5 Kinematic Reconstruction Methods **35**

5.1 The Electron Method . . . 35
5.2 The Hadronic Method . . . 35
5.3 The Double Angle Method . . . 36
5.4 The Σ Method . . . 37
5.5 Comparing the Methods . . . 37
5.6 The $e\Sigma$ Method . . . 38

6 Event Selection **39**

6.1 Introduction . . . 39

6.2 The Electron Finder . . . 39

6.3 The Run Selection . . . 41

6.4 The Trigger Selection . . . 42

6.5 Vertex and Track Requirements . . . 46

6.6 Background Suppression . . . 48

6.7 Alignment and Calibration of Electron variables . . . 49

6.8 Calibration of Hadronic variables . . . 50

6.9 The Full NC Event Selection . . . 50

7 NC Cross Section Measurement **55**

7.1 Bin Selection . . . 55

7.2 Purity, Stability and Acceptance . . . 56

7.3 Cross Section Extraction . . . 58

7.4 Systematic Uncertainties . . . 61

8 Neutral Current Cross Section Measurement and Extraction of $x\tilde{F}_3$ **63**

8.1 Introduction . . . 63

8.2 The x and Q^2 dependence of the cross section . . . 63

8.3 The double differential Neutral Current cross section . . . 65

8.4 The $x\tilde{F}_3$ Extraction . . . 65

8.5 Conclusion . . . 69

9 Hera II Data **72**

9.1 Introduction . . . 72

9.2 The Upgrade Project . . . 72

9.2.1 The HERA Upgrade 72
9.2.2 The H1 Upgrade 73
9.3 Polarisation 74
9.4 Data Quality Tools 76
9.5 Data Quality Plots and New Data Efficiencies 77
9.6 Recent Developments 79

10 Summary **81**

A **83**

Bibliography **87**

List of Figures

2.1 Feynman diagrams of NC (left) and CC (right) deep inelastic scattering processes. 4

2.2 Comparison of the Charged Current and Neutral Current $d\tilde{\sigma}/dQ^2$ cross sections plotted against Q^2. 8

2.3 The structure function F_2, plotted as a function of Q^2 for different values of x. The H1 data and fit results are shown, along with the results of the NMC and BCDMS fixed target experiments, which found the first evidence of scaling violation. 10

2.4 The reduced cross section for e^+p and e^-p scattering (top) and the structure function $x\tilde{F}_3$(below) in bins of Q^2 as a function of x. The inner error bars represent the statistical uncertainty, while the outer error bars include the systematic errors. 11

2.5 The H1 extraction of the structure function $\tilde{F}_L$ at a fixed value of $y = 0.75$ and high Q^2. 12

2.6 Feynman diagrams describing the various quark and gluon splitting functions. 14

2.7 The H1 PDF 2000 fits for the valance quarks xu_v and xd_v, the sea quarks xS and the gluon xg. The PDFs were defined at an initial scale, $Q^2 = 4$ GeV^2, and evolved to $Q^2 = 10$ GeV^2 using the DGLAP equations. 15

3.1 The kinematic range covered by the colliding ep beam detectors (H1 and ZEUS) compared to fixed target experiments. 17

3.2 The HERA accelerator and PETRA pre-accelerator 18

3.3 The H1 Detector 20

3.4 The H1 Calorimetry system 22

3.5 The H1 Tracking Detectors 24

3.6 The H1 Triggering System (L2 components not shown) 29

3.7 A side view of the LAr in the $y-z$ plane. The thick lines show the borders of the different towers. 30

5.1 The resolution in Q^2 (left) and x (right), plotted as a function of y for different reconstruction methods. 38

6.1 The Event Yield, the number of events/nb^{-1} plotted in bins of 50 nb^{-1}. . . 41

6.2 The efficiency of trigger element LAr_el1 plotted as a function of the scattered electron energy. 43

6.3 A plot of the Q^2-x phase space. The diagonal lines show the HERA limit y=1 (full line), the y=0.9 cut (dots and dashes) and the y=0.63 cut (dotted line). The vertical (dotted) line is the Q^2=890 GeV cut and the curved (full) line is the E'_e=11 GeV limit. The requirement of an electron energy greater than 11 GeV is shown to be accounted for by a cut on both y_e and Q^2. 44

6.4 (a) A plot of the LAr_T0 Trigger Element efficiency plotted as a function of scattered electron energy and (b) the Ray_T0 Trigger Element efficiency plotted as a function of y_h 44

6.5 The LAr_el1 Trigger Element efficiency plotted as a function of z-impact (a) and ϕ (b), calculated without imposing fiducial volume cuts. 45

6.6 The z-vertex distribution before (a) and after (b) reweighting the Monte Carlo. 46

6.7 The track-cluster DCA in cm, with the number of events plotted on a log scale. The NC DIS model (red line) is compared to the combined background (green line) and they are seen to be of the same order of magnitude at a DCA greater than 12 cm. The data points are plotted up to the cut value of 12 cm. The discrepancy between the data and model points arise from a poor ability to simulate the DCA of DTRA tracks. This discrepancy is larger at low values of DCA, but this is hard to tell due to the log scale used for the y-axis. 47

6.8 Vertex fitted track efficiency plotted as a function of θ. 47

6.9 From top to bottom: Plots of the energy, polar and azimuthal angle of the scattered electron. The data are shown as points, the sum of the background Monte Carlos is shown as a green line and the sum of the model and background Monte Carlos is shown as a red line. 52

6.10 From top to bottom: Plots of the z-vertex of the event, the point in z of impact of the electron on the LAr surface for negative values of z and then for positive values of z. The data are shown as points, the sum of the background Monte Carlos is shown as a green line and the sum of the model and background Monte Carlos is shown as a red line. 53

6.11 From top to bottom: Plots of the total $E - P_z$, the kinematic variable y, calculated using the $e\Sigma$ method and the $\log_{10} Q^2$ of the event. The data are shown as points, the sum of the background Monte Carlos is shown as a green line and the sum of the model and background Monte Carlos is shown as a red line. 54

7.1 An illustration of possible bin migrations is shown above, the arrows show the path of migration of an event starting at the generated level and pointing to the position it is in at the reconstructed level. The thick blue squares are bins inside the measured phase space, and the thin red lined squares depict bins outside the binning scheme of this analysis. (a) depicts the situation where the bin number (i) of an event is not changed by the detector simulation. (b) shows a generated level event being lost from the reconstructed sample as it is reconstructed outside of the phase space measured in the analysis. (c) is an example of an event that does not fall into the analysis binning scheme at the generated level but is reconstructed in the phase-space measured in this analysis. Finally, (d) is an example of an event that changes bin number during the detector simulation. 57

7.2 Plots of the purity (top), stability (middle) and acceptance (bottom), plotted as a function of x, in bins of Q^2. 59

8.1 The single differential cross section as a function of Q^2. The points are measured using 99-00 e^+p data, with the error bars delimiting the statistical uncertainty (inner) and total uncertainty (outer) including the systematic errors added in quadrature. The solid line is the theoretical prediction of the H1 PDF 2000 fit. 64

8.2 The single differential cross section as a function of Bjorken-x. The points are measured using 99-00 e^+p data, with the error bars delimiting the statistical uncertainty (inner) and total uncertainty (outer) including the systematic errors. The solid line is the theoretical prediction of the H1 PDF 2000 fit. 64

8.3 The reduced cross section, plotted against x in bins of Q^2. The red points are the results of the object orientated analysis using 99-00 e^+p data, with the error bars delimiting the statistical uncertainty (inner) and total uncertainty (outer) including the systematic errors. The blue points are the results from the latest H1 paper, with the error bars showing the total error. The solid line is the theoretical prediction of the H1 PDF 2000 fit. The bins shown in this figure range from $Q^2 = 100$ GeV^2 to $Q^2 = 500$ GeV^2 66

8.4 The reduced cross section, plotted against x in bins of Q^2. The red points are the results of the object orientated analysis using 99-00 e^+p data, with the error bars delimiting the statistical uncertainty (inner) and total uncertainty (outer) including the systematic errors. The blue points are the results from the latest H1 paper, with the error bars showing the total error. The solid line is the theoretical prediction of the H1 PDF 2000 fit. The bins shown in this figure range from $Q^2 = 650$ GeV^2 to $Q^2 = 5000$ GeV^2 67

8.5 The reduced cross section, plotted against x in bins of Q^2. The red points are the results of the object orientated analysis using 99-00 e^+p data, with the error bars delimiting the statistical uncertainty (inner) and total uncertainty (outer) including the systematic errors. The blue points are the results from the latest H1 paper, with the error bars showing the total error. The solid line is the theoretical prediction of the H1 PDF 2000 fit. The bins shown in this figure range from $Q^2 = 8000$ GeV^2 to $Q^2 = 30000$ GeV^2 68

8.6 Top: The reduced cross section, measured in integrated bins of Q^2 plotted against x. The blue circles are the results of the Object Orientated analysis using 99-00 e^+p data. The solid line is the theoretical reduced cross section prediction of the H1 PDF 2000 fit. The dashed line is the theoretical prediction of the reduced cross section without a contribution from the $x\tilde{F}_3$ term. Bottom: The $x\tilde{F}_3$ extraction measured in integrated bins of Q^2 plotted against x. The red circles are the results of the Object Orientated analysis using 99-00 e^+p data, with the error bars delimiting the statistical uncertainty (inner) and total uncertainty (outer) including systematic errors. The blue points are the results of the latest H1 $x\tilde{F}_3$ measurement, with the error bars showing the total uncertainty. The solid line is the theoretical prediction of the H1 PDF 2000 fit. 70

9.1 The theoretical prediction for CC measurements with a polarised electron beam, for both e^+ and e^- running. The points at P $= \pm 0.6$ are simulated predictions, while the points at P $= 0$ are the measured cross section results. 75

9.2 The theoretically predicted NC Cross Section for electron and positron beams with left and right handed polarisation, compared to the unpolarised theoretical curve. 76

9.3 Top: The HERA II LAr_T0 Trigger Efficiency, plotted as a function of scattered electron energy (left) and y_h (right). Bottom: The HERA II DCRϕ_T0 Trigger Efficiency, plotted as a function of scattered electron energy (left) and y_h (right). 78

9.4 Data quality variable plots, showing the distributions for $log_{10}Q^2$ (top left), the z-vertex distribution, the scattered electron energy (bottom left) and the total $E - Pz$ (bottom right). 79

9.5 The preliminary polarised CC cross section measurements using HERA II data. 80

List of Tables

6.1 The cluster estimators, their descriptions and the cut values which are used by QESCAT. 40

6.2 A description of the subtriggers used in this analysis, including the main trigger elements used to construct the subtrigger. 42

6.3 A list of the cuts used to select the high Q^2 NC DIS event sample. The selection criteria fails to remove $\sim$ 3000 background events, the majority of which are low Q^2 DIS events and photoproduction. 49

9.1 A comparison of the design parameters for HERA I and II. 73

9.2 A list of the cuts used to monitor the data quality. 77

A.1 83

A.2 84

A.3 85

A.4 86

Chapter 1

Introduction

At the beginning of the 20th century, the general belief was that the atom was made up of electrons that flow in a positively charged matter, according to the Thomson model [1]. In 1911 Rutherford and his colleagues Geiger and Marsden collided α particles with thin gold foil, and were surprised to see that some of the particles were deflected to a large degree [2], as such a result was not in holding with the atomic model of the time. Rutherford said of this that "it was like firing a cannonball at tissue paper, and having it ricochet off". This prompted Rutherford to postulate that the force exerted on the α particle was due to a small positively charged nucleus in the centre of the atom. He further concluded that this positively charged nucleus would be approximately 10^{-15}m in size, and carried 99.9% of the atom's mass. The nucleus was later understood to be composed of neutrons and protons. In 1956 Hofstader [3] discovered that protons and neutrons have a finite size by scattering electrons off a hydrogen target.

In 1969 high energy inelastic electron-proton scattering experiments at the Stanford linear collider (SLAC) showed the first direct evidence of nucleon sub-structure [4, 5]. The scattering cross section was found to be independent of the magnitude of the squared four-momentum transfer, Q^2, other than a dependence on the propagator term $1/Q^4$, as predicted by Bjorken [6]. Feynman explained this by postulating the presence of partons within the proton [7], which were identified as the quarks postulated by Gell-Mann from the symmetry properties of the spectrum of hadrons [8].

In the Standard Model the proton consists of point-like quarks, which have spin 1/2, carry fractional charge and interact with one another via the strong force. The strong force is described by the theory of Quantum Chromodynamics (QCD), and is mediated by the exchange of massless vector bosons called gluons. When an electron interacts with a quark from the proton, as opposed to scattering off the proton as a whole, the reaction is said to be deeply inelastic. Deep Inelastic Scattering (DIS) interactions are often described in terms of Q^2 and the Bjorken scaling variable x. Bjorken-x can be interpreted as the fraction of the proton momentum carried by the struck quark, in the proton's infinite momentum frame. The evolution in x and Q^2 of the proton's structure functions provides an important test of QCD. It also allows measurements of the quark

and gluon distributions expressed as Parton Distribution Functions (PDFs), which cannot be predicted by this theory.

The establishment of weak interactions began in 1971 with the observation of neutral current neutrino scattering in the Gargamelle Bubble Chamber [9]. The electromagnetic and weak forces were united into one theory by Glashow Salam and Weinberg [10], who predicted the existence of two charged ($W^{\pm}$) and one neutral (Z^0) bosons of large mass. The observations of these particles in collider experiments [11, 12] is one of the successes of that theory, and it has yet to be contradicted by any results of high energy collider experiments. There remains to observe the Higgs boson which is held responsible for the breaking of the $SU(2)_L \times U(1)$ gauge symmetry.

In the past 35 years various DIS experiments have helped to constrain parameters of the electroweak theory and to understand the partonic structure of the proton [13−18]. These experiments were all made by colliding leptons with a stationary (fixed) target of protons or heavy nuclei, and the energy of the centre of mass system was restricted to $\sqrt{s} \lesssim 40$ GeV.

In 1992 the H1 detector, based at the Hadron Electron Ring Accelerator (HERA) in Hamburg, Germany, started data-taking. The HERA accelerator is the first electron-proton beam collider, and attains a centre of mass energy of 320 GeV, almost an order of magnitude higher than previous fixed target experiments. At HERA, proton structure can be probed in new kinematic regions, especially the low x and high Q^2 regions. Unlike the previous, fixed target, experiments, H1 is able to make detailed studies of the hadronic final state of DIS interactions, making the first measurements of this kind.

From late 2000 to mid 2002 HERA and H1 underwent extensive hardware upgrades, aimed at increasing the luminosity by a factor of ten and running with a polarised positron beam. H1 also made a number of detector upgrades and a software upgrade, aiming to replace all the old analysis and data-file production code with Object Orientated (OO) C++ code. This upgrade aimed at producing generic data files, which would be standardised throughout H1, as well as writing an Object Orientated Analysis Framework.

In chapter two of this thesis a brief overview of DIS at H1 is given, concentrating on neutral current theory and proton structure. The third chapter describes the HERA accelerator and H1 detector. Chapter 4 describes the Monte Carlo modelling of neutral current signal and backgrounds and the simulation of the H1 detector. Chapter 5 describes a number of kinematic reconstruction methods used in this analysis. The sixth chapter describes the event selection procedure used to obtain a neutral current sample, and chapter 7 describes the method used to measure the neutral current cross section using this sample. The results of the cross section measurement are presented in chapter 8. Chapter 9 details the HERA II upgrade project and outlines the early work done on data quality assessment. Finally the results are summarised in chapter 10, and a perspective is given.

Chapter 2

HERA Physics

2.1 Introduction

In this chapter the basic concepts of electron-proton (ep) Deep Inelastic Scattering (DIS) are introduced. The Neutral Current (NC) interaction, cross section and proton structure functions are described in detail, followed by a brief description of the Charged Current (CC) interaction. There follows an outline of how measuring these two interactions enables us to determine the composition of the proton, and the momentum-distribution of quarks and gluons within the proton. The chapter finishes with a brief description of the theory of strong interactions, Quantum Chromodynamics (QCD), as it relates to DIS.

2.2 Deep Inelastic Scattering

At HERA there are two kinds of DIS interactions: charged current ($ep \to \nu X$) and neutral current ($ep \to eX$), which proceed through virtual electroweak gauge boson exchange. These two interactions are depicted in the Feynman diagrams shown in figure 2.1.

Neutral current interactions (2.1(a)), proceed through either virtual photon (γ) or Z^0 boson exchange. There is an interference term between the amplitudes for these two exchanges. In charged current interactions (2.1(b)), a $W^{\pm}$ is exchanged, and an outgoing (anti)neutrino is inferred, depending on the incident electron[1] charge.

The kinematics of DIS processes are described in terms of Lorentz invariant quantities. The 4-vectors of the initial state and final state leptons are labelled k and k' respectively, p is the 4-vector of the initial state proton, while the final state hadrons are described by the 4-vector h. From the Feynman diagrams, it can be seen that $h = p + q$, where $q = k - k'$ is the 4-vector of the exchanged vector boson.

[1]The term "electron" is often used in H1 papers to refer to both positrons and electrons. This convention will be used from this point on.

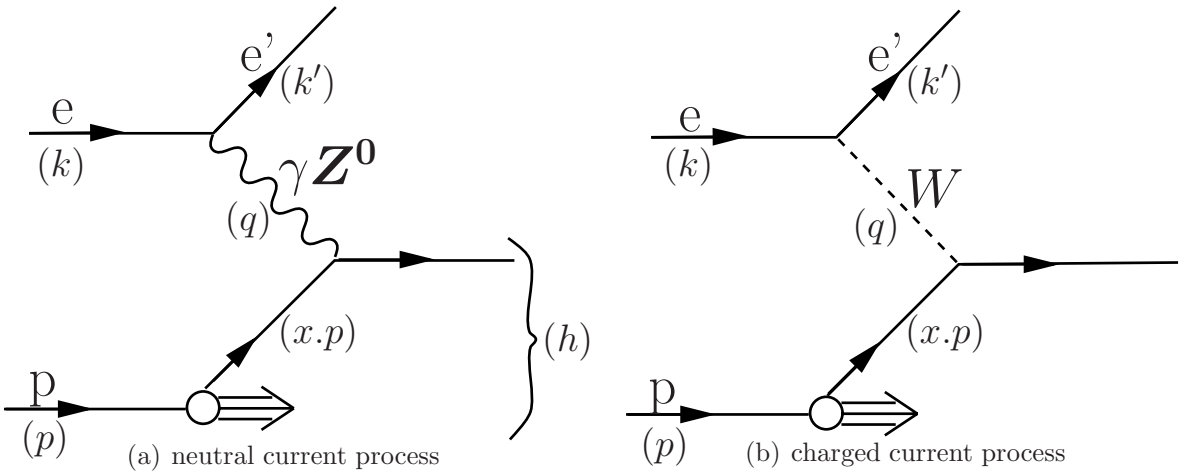

Figure 2.1: Feynman diagrams of NC (left) and CC (right) deep inelastic scattering processes.

The cross sections can be defined in terms of the kinematic variables Q^2, Bjorken x, and y, given by

$$Q^2 = -q^2, \qquad x = \frac{Q^2}{2P \cdot q}, \qquad y = \frac{P \cdot q}{P \cdot k}. \tag{2.1}$$

Q^2 is the negative squared 4-momentum transfer of the exchanged boson. Bjorken x is the fraction of the proton momentum carried by the struck parton in the proton's infinite momentum frame, and y is the fraction of the electron momentum carried by the exchanged boson in the proton's rest frame. Q^2, x, and y are related to the centre of mass energy, $\sqrt{s}$, by $Q^2 = sxy$ (neglecting the electron and proton masses). For the data used in this analysis the centre of mass energy is ~ 320 GeV.

The wavelength of the exchanged boson, λ, is related to Q^2 by $\lambda \sim 1/Q^2$, and thus probing at higher values of Q^2 resolves the finer structure of the proton. Nuclear scattering experiments demonstrate that the effective diameter of the proton is $\simeq 1$ fm [19] which corresponds to $Q^2 \sim 1$ GeV^2. Therefore at higher values of Q^2 the exchanged boson can be thought of as resolving the proton's sub-structure, and coupling to a constituent of the proton, referred to as a parton. This is known as the DIS regime.

2.3 Neutral Current Interactions

2.3.1 Low Q^2 Physics

In low Q^2 ep collisions the NC interaction is dominated by γ exchange, with the Z^0 exchange suppressed due to the large mass of the propagator. The cross section is pro-

portional to the amplitude squared [20]:

$$\frac{d^2\sigma(e^{\pm}p)}{dxdy} \propto |A|^2 = \frac{1}{q^4} L_{\mu\nu} W^{\mu\nu}, \tag{2.2}$$

where

$$A = \frac{1}{q^2} j_\mu J^\mu. \tag{2.3}$$

The $1/q^2$ term describes the exchanged photon propagator, j_ν and J^ν are the electron and hadronic currents, respectively, and likewise $L_{\mu\nu}$ and $W^{\mu\nu}$ are their respective tensors. The leptonic contribution is entirely determined by QED, while the hadronic part depends on the interaction of the electronic current with the proton target.

Using theoretical assumptions (such as parity and time reversal invariance) and a generalised combination of momenta it is possible to simplify equation 2.2 and express the cross section as [19, 21]

$$\frac{d^2\sigma(e^{\pm}p)}{dxdy} = \frac{4\pi\alpha^2(s-M^2)}{Q^4} \left[\left(1 - y - \frac{M^2 xy}{s - M^2} \right) F_2 + \frac{y^2}{2} 2xF_1 \right] \tag{2.4}$$

where α is the fine structure constant, M is the mass of the proton and $2xF_1$ and F_2 are proton structure functions. The total cross section can be described as the sum of the contributions from the two polarised states of the mediating photon, transverse and longitudinal, $\sigma_{tot} = \sigma_T + \sigma_L$. The transverse part of the cross section is described by $2xF_1$, while F_2 describes the sum of both polarisation types. To describe the purely longitudinal polarised contribution, we introduce a third structure function, F_L which is related to the other two structure functions via

$$F_L = \left(1 + \frac{4M^2x^2}{Q^2} \right) F_2 - 2xF_1, \tag{2.5}$$

which, if substituted into equation 2.4 for $2xF_1$, leaves us with a cross section in terms of F_2 and F_L

$$\frac{d^2\sigma(e^{\pm}p)}{dxdy} = \frac{2\pi\alpha^2(s-M^2)}{Q^4} \left[\left(1 + (1-y)^2 + \left[2\frac{xy}{s} - \frac{xy}{s - M^2} \right] \right) F_2 - y^2 F_L \right]. \tag{2.6}$$

This equation can be further simplified by taking into account that at H1 $s \gg x, y, M$, and using the relation $Q^2 = sxy$ to convert the cross section to

$$\frac{d^2\sigma(e^{\pm}p)}{dxdQ^2} = \frac{2\pi\alpha^2}{xQ^4} \left[\left(1 + (1-y)^2 \right) F_2 - y^2 F_L \right]. \tag{2.7}$$

2.3.2 High Q^2 Physics

At HERA, the high Q^2 regime is reached, and Z^0 exchange contributes to the neutral current cross section (both purely, and also interfering with the amplitude of the photon exchange). A third structure function is needed to describe the effect of the Z^0 on the cross section. The cross section equation is then written as,

$$\frac{d^2\tilde{\sigma}(e^{\pm}p)}{dxdQ^2} = \frac{2\pi\alpha^2}{xQ^4}\left[Y_+\tilde{F}_2 - y^2\tilde{F}_{_L} \mp Y_-x\tilde{F}_3\right]. \tag{2.8}$$

defining $Y_\pm = 1 \pm (1-y)^2$. $\tilde{F}_2$ and $x\tilde{F}_3$ can be defined in terms of the exchanged boson contributions to the structure functions

$$\tilde{F}_2 = F_2 - v_e\frac{k_wQ^2}{Q^2 + {M_Z}^2}F_2^{\gamma Z^0} + (v_e^2 + a_e^2)\left[\frac{k_wQ^2}{Q^2 + {M_Z}^2}\right]^2 F_2^{Z^0} \tag{2.9}$$

$$x\tilde{F}_3 = -a_e\frac{k_wQ^2}{Q^2 + {M_Z}^2}xF_3^{\gamma Z^0} + 2a_ev_e\left[\frac{k_wQ^2}{Q^2 + {M_Z}^2}\right]^2 xF_3^{Z^0}. \tag{2.10}$$

The tildes on the structure functions indicate that they now depend on the Z^0 exchange and γZ^0 interference terms, as well as on the γ contribution. F_2 is the purely electromagnetic contribution to the exchange, while the terms arising from the photon-Z^0 boson interference are marked with the γZ^0 superscript, and the pure Z^0 contribution is superscripted accordingly. v_e and a_e are the vector and axial vector couplings of the Z^0 to the electron, respectively, which are related to the weak isospin I_{3e}. M_Z is the mass of the Z^0 and k_w is a function of the weak mixing angle, θ_W

$$a_e = -I_{3e} = \frac{1}{2}, \quad v_e = I_{3e} + 2\sin^2\theta_W \simeq 0.04, \quad k_w = \frac{1}{4\sin^2\theta_W\cos^2\theta_W} \simeq 1.39. \tag{2.11}$$

As $a_e \gg v_e$, and the propagator term $k_wQ^2/(Q^2 + {M_Z}^2)$ typically suppresses the contribution heavily, it is deduced that the photonic contribution dominates in $\tilde{F}_2$ while $x\tilde{F}_3$ is dominated by the γZ^0 interference term for most of the accessible phase space. At higher values of Q^2, however, an increased sensitivity to the Z^0 and γZ^0 terms is achieved.

The double differential NC cross section can be presented in the form of the "reduced cross section"

$$\tilde{\sigma}^{\pm}_{NC} = \frac{xQ^4}{2\pi\alpha^2}\cdot\frac{1}{Y_+}\cdot\frac{d^2\tilde{\sigma}}{dxdQ^2} = \tilde{F}_2 \mp \frac{Y_-}{Y_+}x\tilde{F}_3 - \frac{y^2}{Y_+}\tilde{F}_{_L} \tag{2.12}$$

which is closely related to the structure function terms. The ± superscript indicates the charge on the electron. The double differential NC cross section can be converted into the reduced cross section with the only external input being the well measured fine structure constant, α.

2.4 Charged Current Interactions

The Charged Current cross section may be expressed in a similar way as the NC case as

$$\frac{d^2\tilde{\sigma}(e^{\pm}p)_{CC}}{dxdQ^2} = \frac{G_F^2 {M_W}^4}{2\pi x}\left[\frac{1}{Q^2+{M_W}^2}\right]^2 (Y_+\tilde{W}_2^{\pm} - y^2\tilde{W}_L^{\pm} \mp Y_- x\tilde{W}_3^{\pm}) \tag{2.13}$$

where M_W is the mass of the W boson and G_F is the Fermi constant which is proportional to $(g/M_W)^2$, where g is the electroweak coupling constant. The CC structure functions $\tilde{W}_2$, $\tilde{W}_L$ and $x\tilde{W}_3$ are defined analogously to the NC structure functions (generalised, longitudinal and parity violating structure functions, respectively).

Figure 2.2 depicts the comparison between NC and CC interactions, which can be easily understood from the cross sections for the two reactions (equations 2.8 and 2.13). The NC cross section is proportional to $(e^2/Q^2)^2$, while the CC cross section is proportional to $(g^2/(Q^2 + {M_W}^2))^2$. The cross sections' Q^2 dependences arise from their propagator terms, which are $1/Q^2$ in the case of NC interactions by γ exchange, and $1/(Q^2 + {M_Z}^2)$ or $1/(Q^2+{M_W}^2)$ for the NC and CC electroweak interactions, respectively. While the NC cross section decreases very rapidly with increasing Q^2, the CC cross section falls less steeply until $Q^2 \approx {M_W}^2 (\approx {M_Z}^2)$, the electroweak unification scale.

Since the Standard Model relates the weak and electromagnetic coupling constants according to

$$g^2 = e^2/\sin{\theta_W}^2 \approx 4e^2 \tag{2.14}$$

the NC and CC cross sections can be expected to be of similar size above the electroweak unification scale, $Q^2 \gtrsim {M_W}^2 \approx {M_Z}^2$, as long as the structure function contributions to both cross sections are of similar magnitude.

From figure 2.2 we see that at low Q^2 the NC cross section is three orders of magnitude larger than the CC cross section. As Q^2 increases, the CC and NC cross sections approach a similar value, with the e^-p CC cross section higher than that for the NC at $Q^2 >$ 10,000, although the e^+p CC cross section remains smaller than that for NC events. These differences arise from the different couplings to different quark flavours depending on the lepton charge.

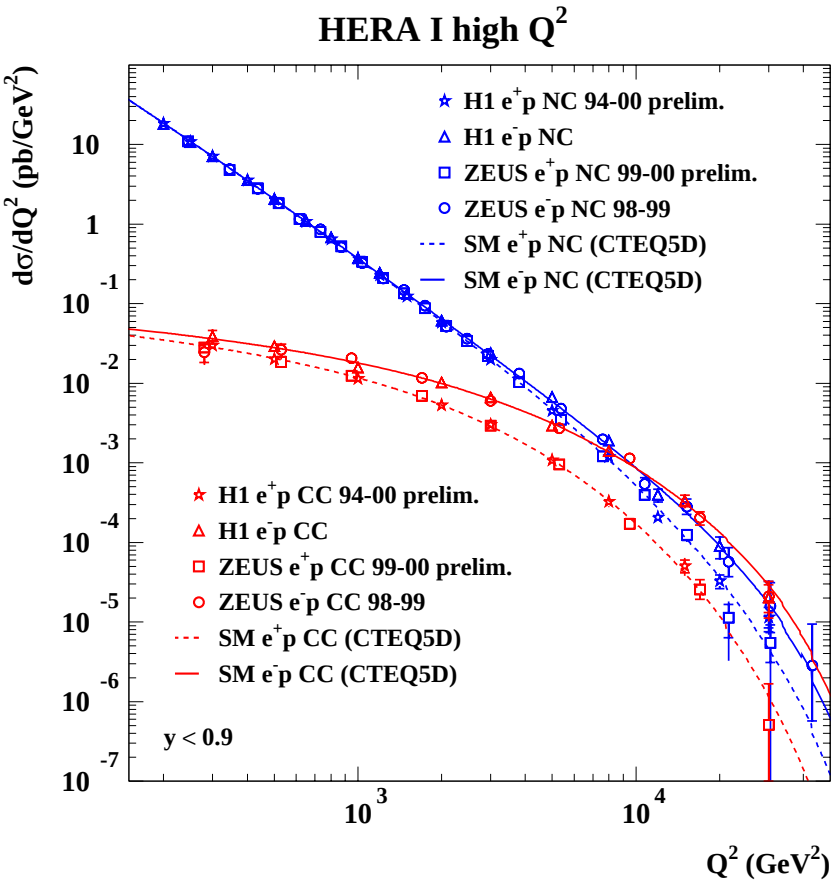

Figure 2.2: Comparison of the Charged Current and Neutral Current $d\tilde{\sigma}/dQ^2$ cross sections plotted against Q^2.

2.5 Neutral Current and Charged Current Structure Functions

2.5.1 NC Structure Functions

In the Quark-Parton Model (QPM), NC DIS is interpreted as the scattering of the electron off a quark constituent of the proton. It is therefore possible to use the QPM to describe the proton structure functions $\tilde{F}_2$ and $x\tilde{F}_3$ in terms of parton distribution functions (PDFs)

$$\tilde{F}_2 = \sum_i A_i(e_{q,i})x\left[q_i(x) + \bar{q}_i(x)\right] \tag{2.15}$$

$$x\tilde{F}_3 = \sum_i B_i(e_{q,i})x\left[q_i(x) - \bar{q}_i(x)\right] \tag{2.16}$$

where the sums are over all six quark flavours. Here the PDFs $xq(x)$ and $x\bar{q}(x)$ represent the probability of finding a quark q, or antiquark $\bar{q}$, carrying a momentum fraction x and A and B are current-fermion coupling terms, which are dependent on the square of the charge carried by the quark, $e_{q,i}$. From these equations we see that $\tilde{F}_2$ is a measure of the total quark and antiquark content of the proton, while $x\tilde{F}_3$ is sensitive to the difference between the quark and antiquark distributions, i.e. it is sensitive to the valance quarks. In addition to the *uud* proton valence there is also a contribution from "sea quarks", which appear in $q + \bar{q}$ pairs and thus do not contribute to the total proton quantum numbers.

Unlike the other structure functions, $\tilde{F}_L$ does not depend on either quark or antiquark distributions. The Callan-Gross relation states that $F_2 = 2xF_1$, and if this relation is substituted into equation 2.5 we find $F_L = 0$. This is due to the fact that the spin 1/2 quarks cannot absorb a longitudinally polarised vector boson. This holds true for the Leading Order (LO) interpretation of the strong interaction in QCD. At Next to Leading Order (NLO), however, the quarks can radiate gluons (the gauge bosons of the strong interaction), allowing them to absorb longitudinally polarised vector bosons, and leading to a non-zero but small size of $\tilde{F}_L$. For this reason $\tilde{F}_L$ is entirely dependent on the gluonic structure of the proton. The theory of Quantum Chromo Dynamics is described in section 2.6

2.5.2 The Measurement of $\tilde{F}_2$

In the QPM the quarks are considered point-like entities and therefore $\tilde{F}_2$ is not expected to vary with the resolving power, Q^2, suggesting that $\tilde{F}_2$ should be scale invariant. In figure 2.3 the experimental measurement of F_2 from HERA and lower energy fixed target data is shown as a function of Q^2 for different values of x. F_2 is seen to exhibit deviations from scaling across a wide range of x and Q^2, called scaling violations. F_2 also rises with Q^2 at low x and, to a lesser degree, falls with Q^2 at high x. The rise of $\tilde{F}_2$ at low x is due to the contribution of the sea quarks, which arise from gluons (see section 2.6) which produce quark-antiquark pairs. For the majority of the $x - Q^2$ phase-space, F_2 has been measured with uncertainties at the percentile level.

2.5.3 The Measurement of $x\tilde{F}_3$

In the top of figure 2.4 [22], the published reduced cross section results obtained for e^+p data are compared with the results from e^-p data taking, as a function of x in bins of Q^2. For $Q^2 \simeq 1500$ GeV^2 the two cross sections are very similar. The two cross sections start to diverge thereafter as Q^2 increases, with the e^+p data points being suppressed, and the e^-p data points being boosted. This effect is due to the $x\tilde{F}_3$ term in equation 2.12.

$x\tilde{F}_3$ can be measured by subtracting the e^+p neutral current cross section from that obtained from e^-p scattering data [23]. This is due to the $\mp$ sign, dependent on lepton charge, of the $x\tilde{F}_3$ term in equation 2.12, which gives rise to the expression

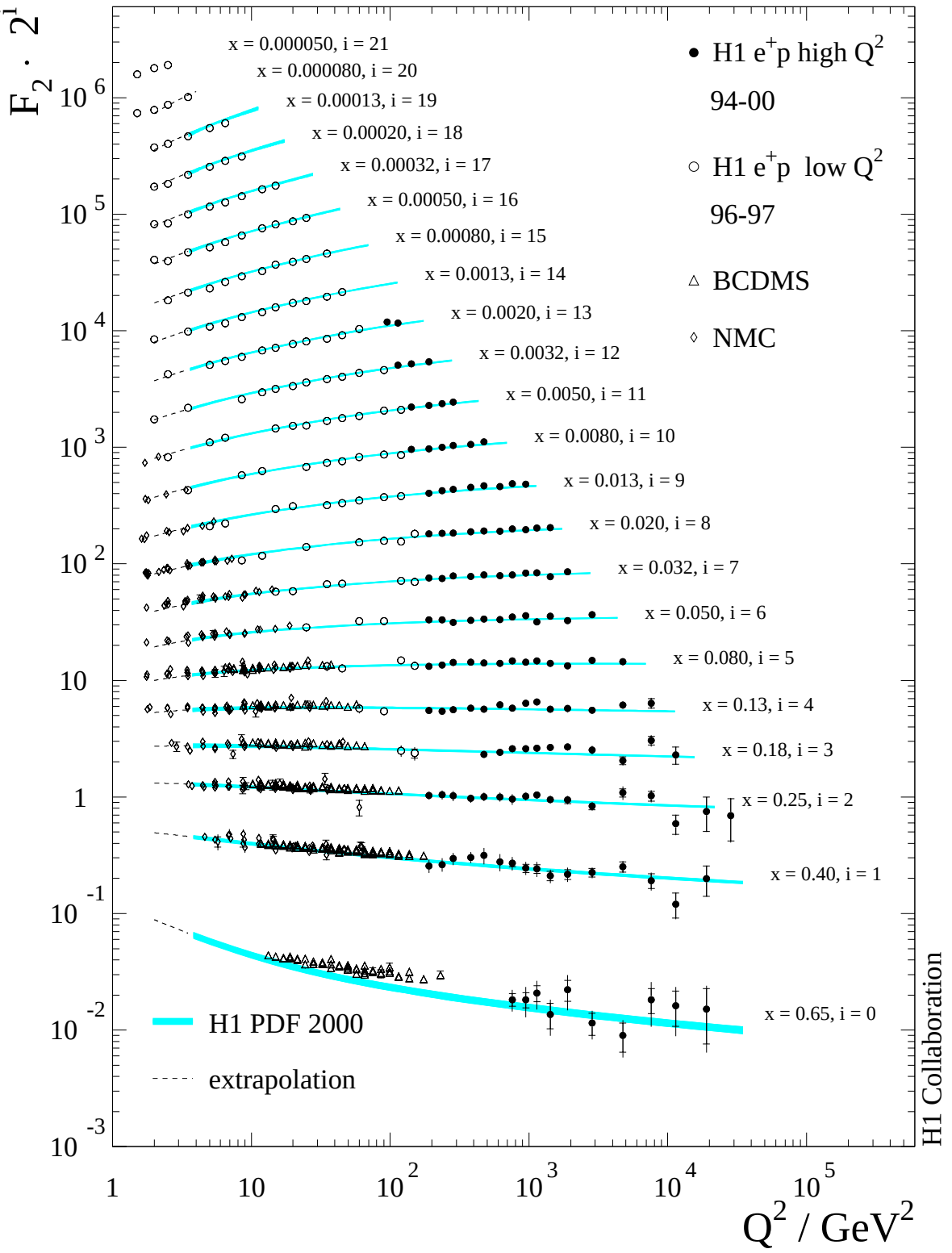

Figure 2.3: The structure function F_2, plotted as a function of Q^2 for different values of x. The H1 data and fit results are shown, along with the results of the NMC and BCDMS fixed target experiments, which found the first evidence of scaling violation.

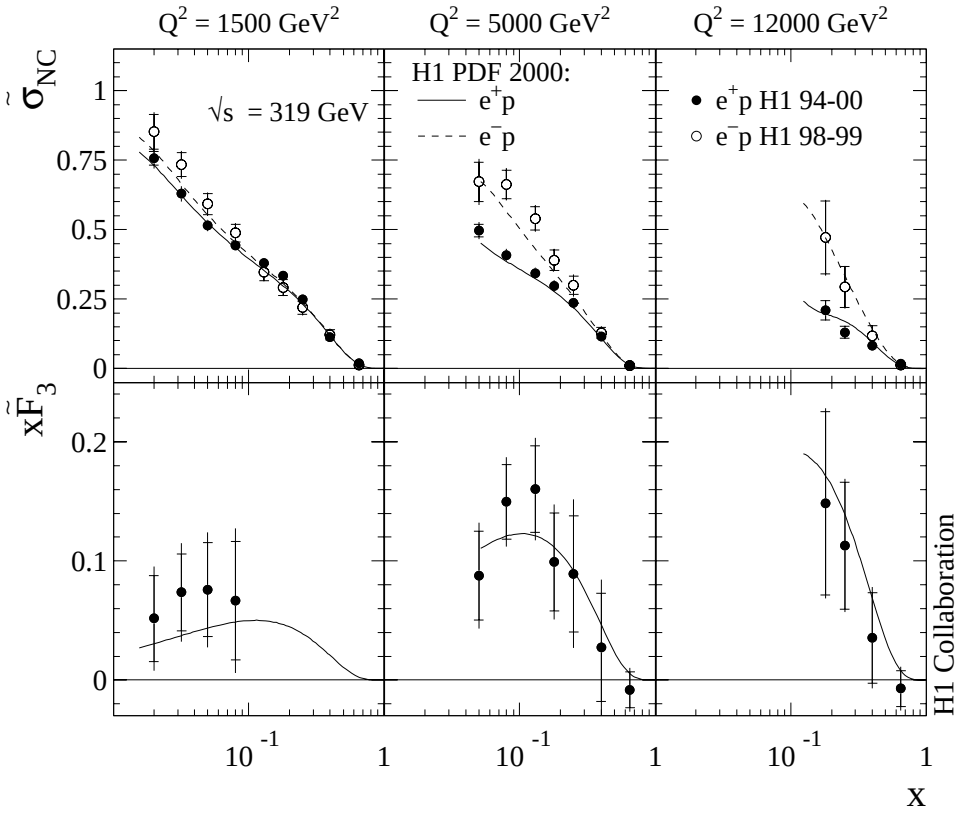

Figure 2.4: The reduced cross section for e^+p and e^-p scattering (top) and the structure function $x\tilde{F_3}$(below) in bins of Q^2 as a function of x. The inner error bars represent the statistical uncertainty, while the outer error bars include the systematic errors.

$$x\tilde{F_3} = \frac{Y_+}{2Y_-}\left[\tilde{\sigma}^{NC}(e^-p) - \tilde{\sigma}^{NC}(e^+p)\right]. \tag{2.17}$$

The measurement is statistically limited, as $x\tilde{F_3}$ only contributes significantly to the cross section at $Q^2 \gtrsim M_Z^2$. A measurement has, however, been done using the whole data sample collected at H1 [22], the result of which is shown in the lower bins of figure 2.4.

The measurement of $x\tilde{F_3}$ is compatible with the theoretical prediction, which is derived from valence quark densities constrained by the measurement of F_2 and CC data (see section 2.6). The large errors on the data points are largely due to the low statistics of the e^-p cross section measurement, where only 16 pb^{-1} of data are available, in comparison to the 110 pb^{-1} of positron data.

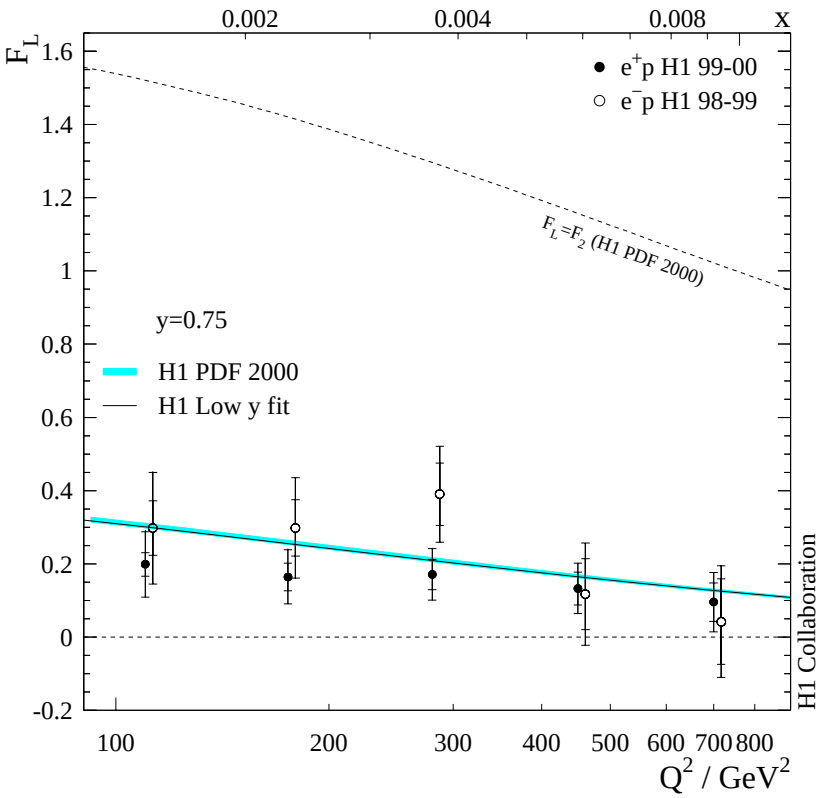

Figure 2.5: The H1 extraction of the structure function $\tilde{F}_L$ at a fixed value of $y = 0.75$ and high Q^2.

2.5.4 The $\tilde{F}_L$ Extraction

Another method to unfold particular structure functions from the cross section is to subtract theoretical predictions of the other structure functions from the measured cross section. In the case of the NC cross section, a value for the longitudinal structure function, $\tilde{F}_L$, has been extracted by using the very good understanding of the generalised structure function, $\tilde{F}_2$, and choosing a region of phase space where there is little contribution from $x\tilde{F}_3$ [22]. The method chosen to extract $\tilde{F}_L$ is to extrapolate the fit results for $\tilde{F}_2$ to the high y region, which is equivalent to evolving from low Q^2 to higher values of Q^2 for a fixed value of x. To avoid a possible influence on the $\tilde{F}_2$ extrapolation from high y data, the NLO QCD fit is repeated using only low y data, $y < 0.35$ and the resulting parton distributions are then extrapolated using the DGLAP equation (described in section 2.6) to obtain $\tilde{F}_2$ in the high y region. The results [22] are shown in figure 2.5 [22] for both e^+p and e^-p data. The extraction of $\tilde{F}_L$ has large errors, because its contribution to the cross section in the measured region is small. However, $\tilde{F}_L$ is seen to be significantly different from zero and is well described by NLO QCD.

It would be possible to measure $\tilde{F}_L$ directly if there was a period of low centre of mass energy running, so that a measurement could be made at the same Q^2 and x values for

different values of y.

2.5.5 CC Structure Functions

For unpolarised particles in the QPM, the generalised CC structure functions are related to the quark densities by

$$\tilde{W}_2^+ = x\left[(d+s)+(\bar{u}+\bar{c})\right] \tag{2.18}$$
$$\tilde{W}_2^- = x\left[(u+c)+(\bar{d}+\bar{s})\right] \tag{2.19}$$
$$x\tilde{W}_3^+ = x\left[(d+s)-(\bar{u}+\bar{c})\right] \tag{2.20}$$
$$x\tilde{W}_3^- = x\left[(u+c)-(\bar{d}+\bar{s})\right] \tag{2.21}$$

and thus the e^+p and e^-p charged current reduced cross sections σ_{CC}^+ and σ_{CC}^- behave as

$$\sigma_{CC}^+ \propto x\left[\bar{u}+\bar{c}\right]+(1-y)^2x[d+s] \tag{2.22}$$
$$\sigma_{CC}^- \propto x[u+c]+(1-y)^2x[\bar{d}+\bar{s}]. \tag{2.23}$$

This can be compared to the NC reduced cross section dependence on parton densities

$$\sigma_{NC}^{\pm} \propto F_2 = x\left[\frac{4}{9}(u+c+\bar{u}+\bar{c})+\frac{1}{9}(d+s+\bar{d}+\bar{s})\right], \tag{2.24}$$

neglecting the contributions from Z^0 exchange and $\tilde{F}_{_L}$. It can be seen that the NC cross section is mostly sensitive to the u-quark density, while the CC cross section is sensitive to the d-quark density in low y (high x) e^+p collisions, and to the u-density in high y e^-p collisions.

2.6 QCD and the DGLAP Evolution

Parton interactions beyond the QPM can be described by Quantum Chromodynamics, the theory of strong interactions. QCD is a non-abelian (non-commutative) gauge theory, which is invariant under $SU(3)$ colour transformations. The gauge bosons of the strong interaction are called gluons, and they couple to the quark colour charge. Quarks can carry one of three colour charges, while there are eight different colour charge combinations for gluons. As with the gauge boson of the electromagnetic force, the photon, the gluon is massless. However, in contrast to the photon, the gluon can interact with other gluons. The gluon-gluon interactions lead to a strong dependence of the coupling strength, α_s, on the scale, Q^2.

At large distances the coupling strength between two colour charges increases, which is why quarks and gluons are not "free", but can only be found bound in hadrons. At small distances (high Q^2) the coupling between the quarks and gluons becomes small, and the quarks and gluons behave as free fermions within bound hadrons. This is known as "asymptotic freedom". α_s is thus a function of Q^2, and is described by the equation

$$\alpha_s(Q^2) = \frac{12\pi}{(33 - 2n_f)\ln Q^2/\Lambda^2_{QCD}} \tag{2.25}$$

to leading order, where n_f is the number of quark types with a mass less than Q^2 and Λ_{QCD} is a scale parameter that has to be determined from experiments [24].

At high Q^2, α_s is small enough that QCD can be treated perturbatively. The parton densities cannot be calculated in perturbative QCD (pQCD), but at higher Q^2 ($> \Lambda^2_{QCD}$) it is possible to test the pQCD predictions of the Q^2 evolution of these parton densities. The evolution of the quark and gluon densities, $q(x, Q^2)$ and $g(x, Q^2)$, as a function of Q^2 is given by the DGLAP [25] equations

$$\frac{dq(x,Q^2)}{d\log Q^2} = \frac{\alpha_s(Q^2)}{2\pi}\int_x^1 \frac{dy}{y}\left[q(y,Q^2)P_{qq}\left(\frac{x}{y}\right) + g(y,Q^2)P_{qg}\left(\frac{x}{y}\right)\right] \tag{2.26}$$

$$\frac{dg(x,Q^2)}{d\log Q^2} = \frac{\alpha_s(Q^2)}{2\pi}\int_x^1 \frac{dy}{y}\left[q(y,Q^2)P_{gq}\left(\frac{x}{y}\right) + g(y,Q^2)P_{gg}\left(\frac{x}{y}\right)\right] \tag{2.27}$$

In these equations $P_{ab}(x/y)$ are the splitting functions, describing the probability of a parton a with momentum y producing a parton b with momentum x as Q^2 increases. The four different splitting functions are described by Feynman diagrams, in figure 2.6.

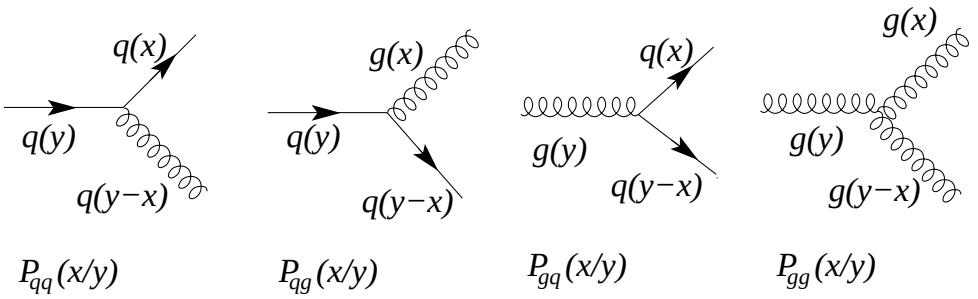

Figure 2.6: Feynman diagrams describing the various quark and gluon splitting functions.

The parton densities of the proton may be extracted by performing a NLO QCD fit to the H1 NC and CC data. The parton densities are parameterised using polynomial functions in x at an initial scale Q_0^2. The parton densities are then evolved in Q^2 using the NLO DGLAP equations at $Q_0^2 = 10$ GeV^2 and fitted to the experimental data. The results of the H1 PDF 2000 fit are shown in figure 2.7. The gluon and sea quark densities are seen to dominate at low x (they are shown scaled down by a factor of 20 in the plot). The

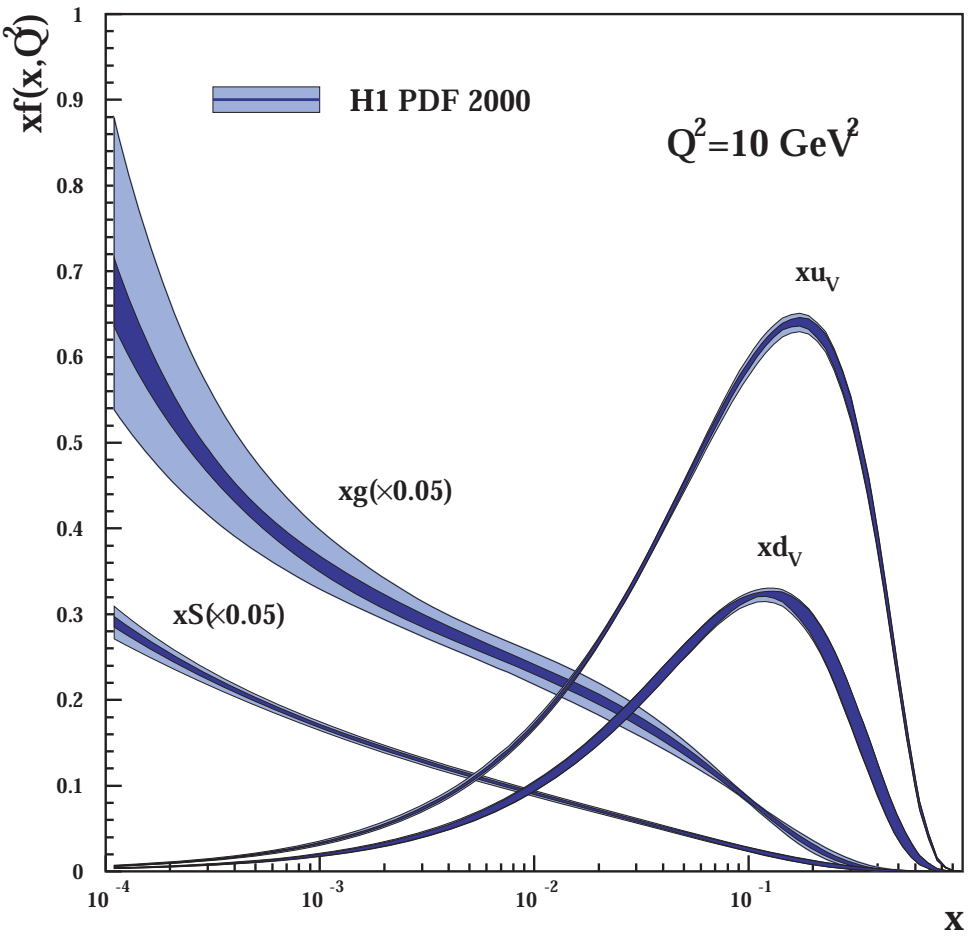

Figure 2.7: The H1 PDF 2000 fits for the valance quarks xu_v and xd_v, the sea quarks xS and the gluon xg. The PDFs were defined at an initial scale, $Q^2 = 4$ GeV^2, and evolved to $Q^2 = 10$ GeV^2 using the DGLAP equations.

valance quark can be seen to contribute at high x ($\sim 0.2 - 0.3$). The bands represent estimates of the experimental and theoretical uncertainties.

Chapter 3

The H1 Detector

In this chapter the HERA accelerator is introduced, followed by an overview of the H1 detector. Further detail is then given of the H1 detector components relevant to this analysis. The final part of the chapter describes the Data Acquisition and Triggering systems.

3.1 HERA

HERA, the world's only lepton-proton beam collider, is based at the DESY (Deutsches Elektronen Synchrotron) site in Hamburg. HERA was completed in 1992, with the purpose of studying Deep Inelastic Scattering (DIS) interactions.

The proton and electron beams are accelerated and stored in beam pipes with a circumference of 6.3km. HERA has been run with both positrons and electrons of 27.6 GeV energy. It originally ran with 820 GeV protons, until 1998, when the proton energy was raised to 920 GeV. The latter beam energies yield a centre of mass energy of 319 GeV, accessing a new kinematic region (see figure 3.1). The unique kinematics at HERA make it possible to study electroweak neutral and charged currents at high momentum transfer and to observe the hadronic recoil (in contrast to fixed target experiments).

The layout of HERA and the pre-accelerator facilities are shown in figure 3.2. The electrons and protons are injected into HERA from PETRA (a pre-accelerator that was previously used as an e^+e^- collider) with energies of 14 GeV and 40 GeV respectively. The electron ring consists of superconducting cavities and normal magnets to accelerate the electrons from 14 GeV up to their colliding energy of 27.6 GeV. This is the maximum electron energy currently achievable, and is limited by the maximum available RF (radio frequency) voltage. The proton ring is made of conventional RF cavities and superconducting magnets (which yield a magnetic field of 4.68 Tesla) and accelerates the protons, injected from PETRA at 40 GeV, up to 920 GeV.

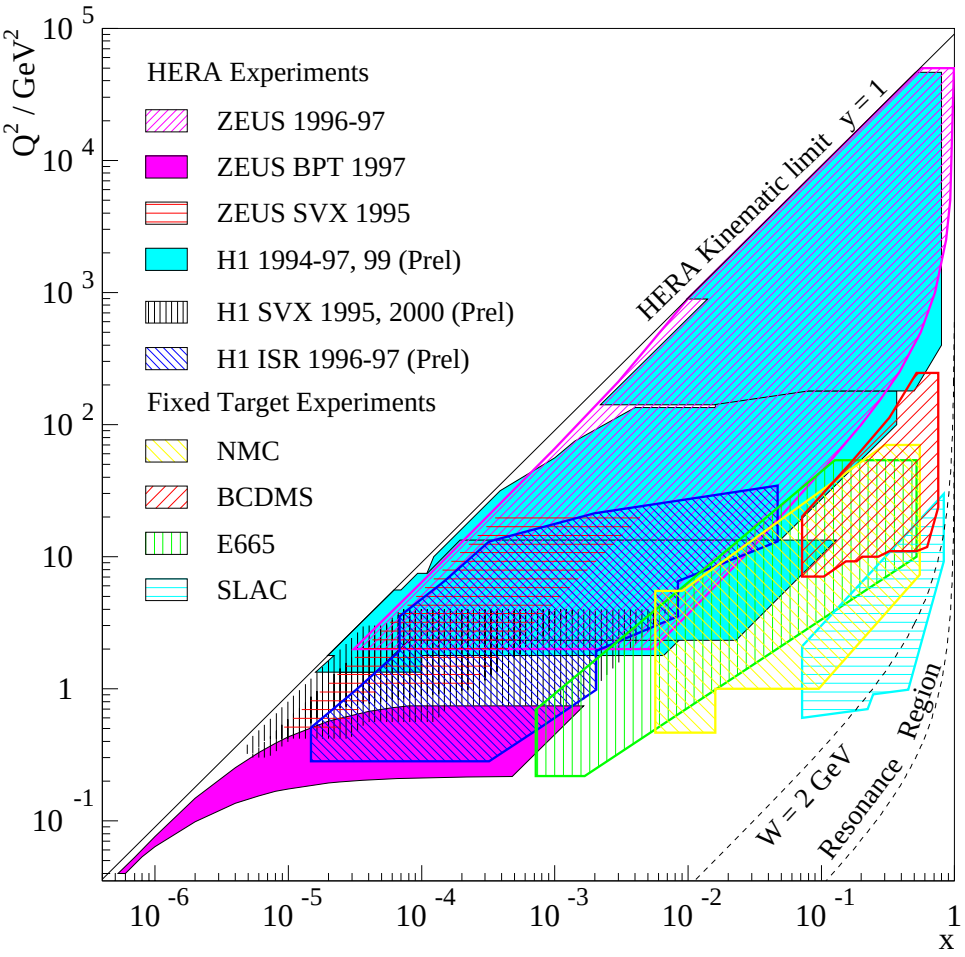

Figure 3.1: The kinematic range covered by the colliding *ep* beam detectors (H1 and ZEUS) compared to fixed target experiments.

The electrons and protons are stored in up to 220 bunches in the two rings with $\simeq 175$ used in collisions. In addition to these "colliding bunches" there are "pilot bunches" which are left unpaired, and are used to determine beam related background. Every bunch consists of $\sim 10^{11}$ particles, which is equivalent to a 50 mA electron beam current and a 100 mA proton beam current, with a Gaussian distribution of width $\sigma \simeq 11$ cm. The proton bunch has a complicated structure which leads to several "satellite bunches" accompanying consecutive bunches. Consecutive bunch crossings are separated in time by 96 ns, which can be compared to the LEP interaction interval of 22 μs and the LHC planned collision interval of 25 ns.

HERA has four interaction points spaced evenly around its 6.3 km circumference. Beam collisions occur at north and south interaction points on the ring, inside the H1 [26] and ZEUS [27] detectors respectively. H1 and ZEUS are both multi-purpose detectors which are used to study all aspects of *ep* collisions. The two greatest differences between the H1 and ZEUS detectors are their central calorimeters and the location of the superconducting coil. H1 uses a liquid-argon calorimeter (described further in section 3.3.1), while ZEUS

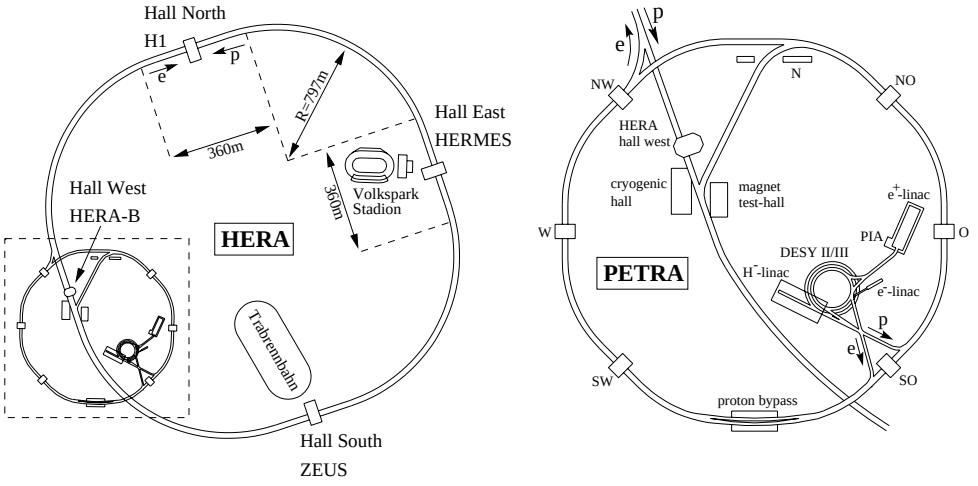

Figure 3.2: The HERA accelerator and PETRA pre-accelerator

uses a uranium scintillator, compensating calorimeter, which has a good hadronic and time resolution. In ZEUS the superconducting coil is located between the trackers and the calorimeter, while in H1 it is outside the calorimeter.

The east and west interaction points are home to the HERMES [28] and HERA-B [29] experiments, respectively, which are both fixed target experiments. HERMES utilises spin rotators to obtain a longitudinally polarised electron beam, which collides with polarised gas targets to investigate the proton and neutron spin structure functions. HERA-B inserts tungsten wires into the proton beam halo with the aim of producing b-quarks to study CP violation.

In late 1999 and early 2000 HERA ran with positrons, and H1 collected 65 pb^{-1} of positron-proton data, which, combined with previous positron data collected in the 1994-1997 period, brings the total e^+p luminosity to over 100 pb^{-1}. This luminosity increase in the later years is due to an increase in beam currents and an increased expert familiarity with both the detector and the accelerator.

From September 2000 HERA and the H1 detector both underwent extensive upgrades, with the aim of running with polarised lepton beams at a much increased luminosity (a factor of 4-5 in peak instantaneous luminosity) [30]. The upgrade project is described in greater detail in section 9.2. The following text describes the H1 detector as it was prior to the upgrade.

3.2 H1

The H1 detector is situated at the north interaction point of the HERA accelerator, with the aim of studying high energy electron-proton DIS. The detector (which is 12 m$\times$10 m$\times$ 15 m with a mass of 2800 tonnes) is designed to identify particles originating from the

collision and also to determine their momenta and energy.

The reference frame used by the H1 experiment is based on a rectangular Cartesian co-ordinate system, with the origin defined by the nominal interaction point. The z-axis lies along the outgoing proton direction, also known as the forward direction, the x-axis then points towards the centre of the ring and the y-axis points vertically upwards. In spherical polar co-ordinates, the outward radial distance is denoted r, the polar angle θ is defined relative to the z-axis so that $\theta = 0^\circ$ along the proton beam direction, and $\theta = 180^\circ$ along the electron direction. Finally, ϕ is the azimuthal angle which is measured from the x-axis such that $\phi = \tan^{-1} y/x$.

The focus on DIS leads to several important requirements being placed on the detector. It is required that the resolution and efficiency for the detection of electrons be high over a large angular range in order to reconstruct the inclusive kinematic variables from the energy and angle of the scattered electron (see section 5.1). The calorimeters are hermetic, in order to accurately measure missing transverse momentum in order to identify and reconstruct charged current DIS (described in section 2.4), and have a high granularity for accurate final state reconstruction. For particle identification and measurement of charged particle momenta and multiplicities, a large angular coverage is required for the trackers. For heavy flavour processes and searches for signatures of exotic particle production, muon detection is required over the whole 4π solid angle. A greater degree of detector instrumentation is required in the forward direction due to the asymmetric beam energies. Finally an advanced pipelined triggering system is required because the detector readout time (~ 800 μs) is greater than the bunch crossing time (96 ns).

A three-dimensional representation of the H1 detector can be seen in figure 3.3. Each subdetector is cylindrically symmetric and centred on the beam pipe. The subdetectors are arranged in layers according to type, and often each layer can be associated with the detection of one type of particle.

Since the centre of mass of the electron-proton collisions is boosted along the forward direction, the H1 detector is asymmetric and highly segmented in this direction. The beampipe [1] is surrounded by the central [2] and forward [3] tracking detectors. Situated around the trackers is the Liquid Argon calorimeter (LAr), which is made up of an electro-magnetic section [4] and an hadronic section [5]. The LAr is in turn surrounded by a superconducting solenoid magnet [7] which provides an axial field of 1.5 T. The instrumented iron return yoke of the magnet [10] is used to detect muons and hadronic showers that escape the LAr. The Forward Muon Detector [11] covers small angles with the beam pipe in the direction of the outgoing protons. The very forward and backward directions are covered by the PLUG [13] and SPACAL [12] calorimeters, respectively, which are situated outside the trackers. The Proton Remnant Tagger (PRT), a detector used in diffractive studies, is situated 24 m down the beam pipe, in the forward direction. The Forward Proton Spectrometer (FPS) is made of four Roman Pots (insertions to the beam pipe, housing scintillating fibre hodoscopes) located between 50 m and 100 m in the forward direction. The pots are used to detect intact final state protons. The Electron Tagger (ET) and Photon Detector (PD) are positioned down the beampipe in the $-z$ direction for the determination of luminosity by measuring the rate of Bethe-Heitler

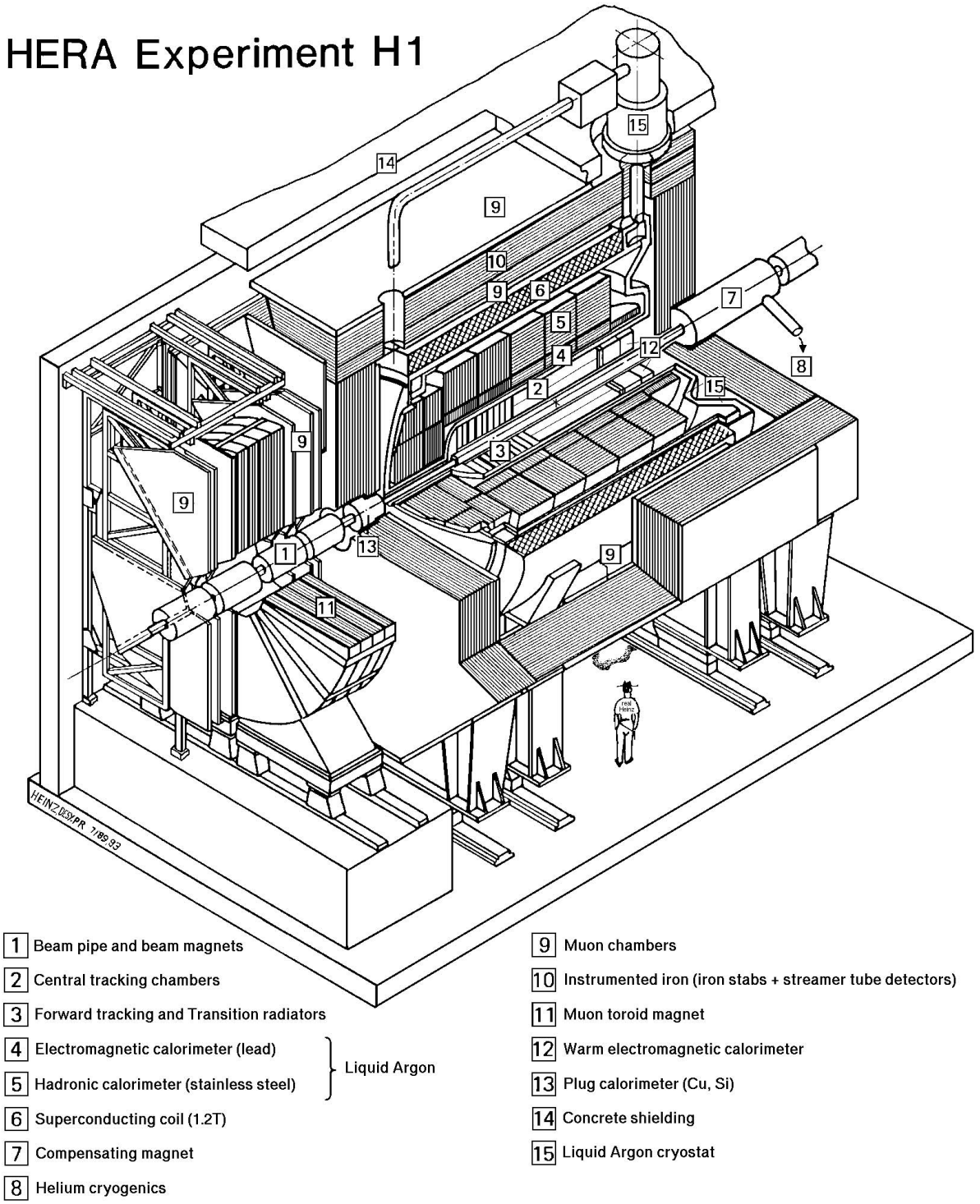

Figure 3.3: The H1 Detector

$ep \to ep\gamma$ interactions. The ET is also used to tag photoproduction ($Q^2 \sim 0$) events. Finally the Very Low Q^2 spectrometer (VLQ) is situated at $z = -2.95$ m and covers the region between the ET and the SPACAL.

A more detailed description of the H1 detector can be found in [26]. In the following sections attention is mostly placed on the components important to this analysis.

3.3 Calorimetry in the H1 Detector

The calorimetry system, shown in figure 3.4, plays a vital role in particle detection and energy measurement in H1. The calorimeters are important as not only can they detect neutral particles, but they can also distinguish electrons and photons from hadrons. Calorimeters function by absorbing the total energy of a particle in layers of passive material (referred to as "absorber") where the particle loses energy by producing a cascade or "shower" of other particles. The energy deposition of the cascade is measured in a sampling material and proportionally converted into a measurable electronic signal.

Electro-magnetic calorimeters are comprised of alternate layers of dense absorbers in which electrons and photons undergo Bremsstrahlung ($e \to e\gamma$) and subsequent pair production ($\gamma \to e^+e^-$) processes, and sampling material in which the subsequent shower of electrons causes further ionisation which is then collected on anode plates as a measurable electronic signal. As an electromagnetic particle rapidly loses energy in the absorbing medium, particles produced by Bremsstrahlung and pair production undergo the same processes themselves, causing a cascade of electromagnetic particles. Ultimately the full energy of the initial electromagnetic particle is deposited. Thus a measurement of the total ionisation energy in the sampling material will lead to a measurement of the incident particle's energy. The radiation length, X_0 is the mean distance which an electromagnetic particle will travel through a medium and decelerate to $1/e$ of its initial energy.

When a hadron passes through the medium of a hadronic calorimeter it interacts both elastically and inelastically with the nuclei of the medium. This results in secondary hadrons being produced which brings about a hadronic shower. The interaction length, λ, is the length analogous to the electromagnetic radiation length, but is typically much larger. In liquid argon $\lambda \simeq 0.8$ m, while $X_0 \simeq 0.14$ m, and the liquid argon calorimeter (LAr) therefore comprises $5 - 8\lambda$ and $20 - 30X_0$. Hadronic showers typically contain both hadronic and electromagnetic components because neutral pions produced in the showering can decay to photons, initiating an electromagnetic shower. The elements of the H1 calorimetry system are the LAr, SPACAL and PLUG calorimeters, the Instrumented Iron and the VLQ (not shown in figure 3.4).

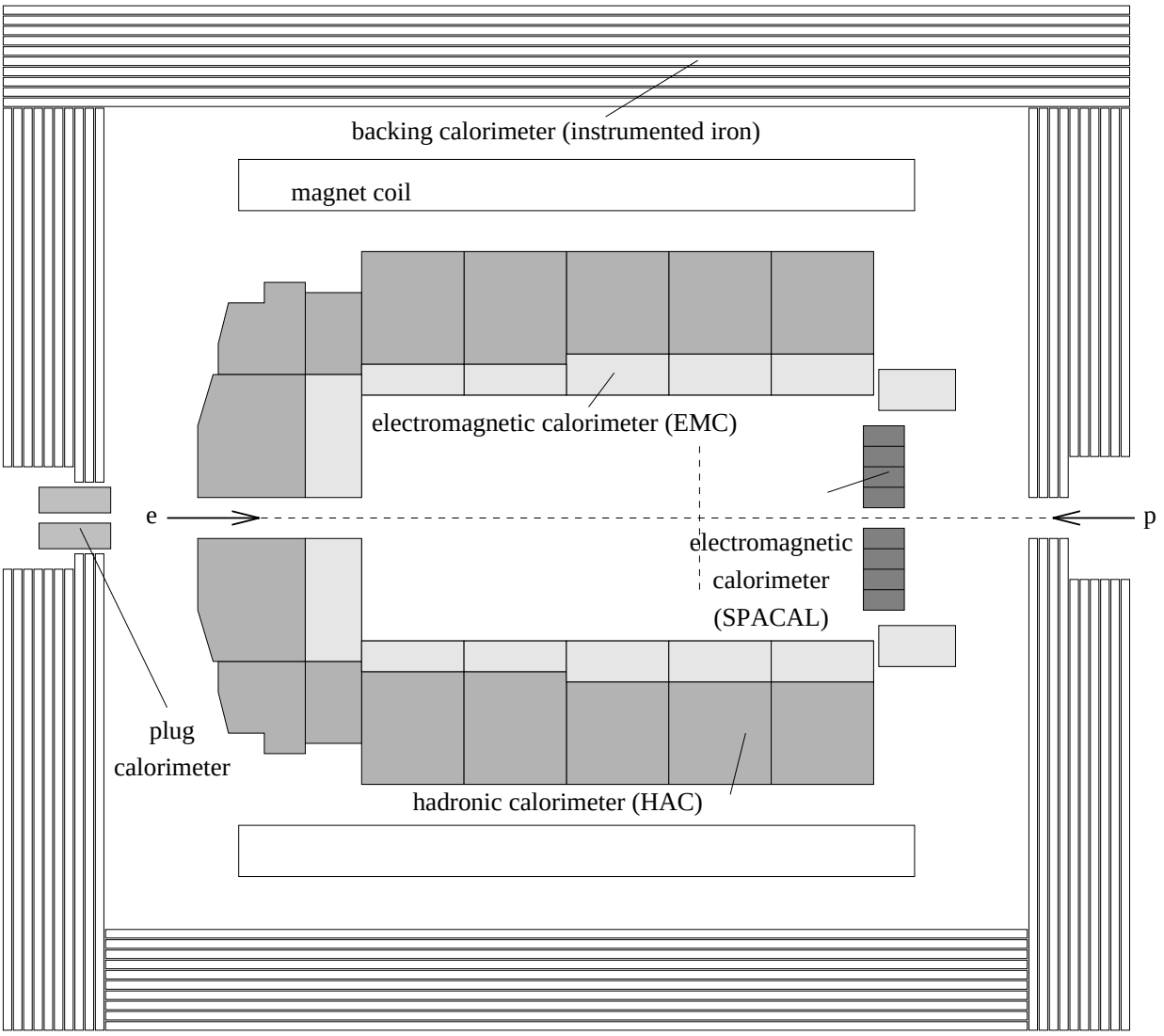

Figure 3.4: The H1 Calorimetry system

3.3.1 The Liquid Argon Calorimeter (LAr)

The liquid argon calorimeter covers the central part of the H1 detector, $4 < \theta < 153°$. It consists of an inner (EMC) section for the measurement of electromagnetic showers, and an outer (HAC) section for the measurement of hadronic showers. It is built out of eight different "z-wheels" (see figure 3.4) which are each divided into ϕ octants. The most backward wheel ($146 < \theta < 153°$) is the Backward Barrel Electromagnetic calorimeter (BBE), and consists of three electromagnetic calorimeter layers and no hadronic layers. Increasing in z are the Central Barrel calorimeter modules (CB1, CB2 and CB3), then the Forward Barrel calorimeters (FB1 and FB2) and finally the Inner and Outer Forward calorimeters (IF and OF), the latter consisting only of two hadronic calorimeter layers. There are insensitive regions between the wheels (z-cracks, indicated with lines in figure 3.4) and between the ϕ octants (ϕ-cracks), which are regions where energy is lost in the measurement.

The LAr calorimeter comprises a total of 45 000 cells, ensuring a good spatial resolution. Each cell is composed of absorber plates, complemented by high voltage and readout electrodes. The sampling medium between the absorber plates is liquid argon, which was chosen for its stability, ease of calibration, homogeneity of response, its fine granularity for e/π separation and because it was cheaper than other noble gases. The EMC uses lead absorber plates, while the HAC uses stainless steel. The absorber plates vary in orientation with z so that the particles originating from the vertex always impact with an angle greater than 45° so as to maximise the path length in the absorber material. The electromagnetic section consists of three cell layers in each wheel, except for FB2 which has four layers, IF which has seven and OF which has none. The cell sizes vary and are optimised to measure the extension of the electromagnetic showers which are used to identify the scattered electron. The mean noise per cell ranges from 10 to 30 MeV. The depth of the EMC corresponds to 20-30 radiation lengths, and the total depth of the EMC and HAC combined varies between 4.5 and 8 interaction lengths.

The LAr energy resolution has been measured using test beams [31, 32], and is $\frac{\sigma(E)}{E} \sim \frac{0.12}{\sqrt{E}} \oplus 0.01$, for electron showers and $\frac{\sigma(E)}{E} \sim \frac{0.50}{\sqrt{E}} \oplus 0.02$ for a hadronic shower (where E is in GeV, the symbol $\oplus$ indicates addition in quadrature and 0.01 and 0.02 are the intrinsic resolutions for electron and hadronic showers, respectively). The LAr is a non-compensating calorimeter, which means that the energy response to hadrons is typically 30% lower than for electrons. This difference in response is corrected by algorithms in the reconstruction software [33] which also optimise the energy resolution [34, 35]. The reconstruction of energies in the LAr is described in detail in [36] and more details on the LAr performance can be found in [37].

3.3.2 The (Backward) Spaghetti Calorimeter (SPACAL)

The SPACAL[1] is a very compact high resolution lead/scintillating fibre calorimeter which provides coverage of the region close to the beam pipe in the θ-range 154 to 177°. Similarly to the LAr, the SPACAL is divided into electro-magnetic and hadronic sections. The hadronic section has a depth of two interaction lengths and contains an integrated timing function to veto proton induced beam background interactions (see section 3.8.2). The electromagnetic and hadronic energy resolutions were measured in test beam experiments [38], and were found to be $\frac{\sigma(E)}{E} \sim \frac{0.13}{\sqrt{E}} \oplus 0.04$ for electrons and $\frac{\sigma(E)}{E} \sim \frac{0.56}{\sqrt{E}} \oplus 0.20$ for hadrons. Additionally, the SPACAL has a very high granularity (1192 cells) which yields a spatial resolution of $\sim$ 2 mm. The SPACAL is mostly used to measure the energy of electrons in NC interactions with $Q^2 < 120$ GeV^2, and in this analysis it is used for the measurement of hadronic energies in the backward region.

[1]The calorimeter is named after the long thin scintillating fibres used as the active layer and for read-out, hence "Spaghetti" Calorimeter

3.3.3 The Instrumented Iron Return Yoke

The LAr and SPACAL are both contained within the Instrumented Iron Return Yoke, a detector that is built up of 16 layers of limited streamer tubes (LSTs), 11 of which are equipped with readout electrodes. From the digital readout "iron tracks" are reconstructed, and used in muon identification (see section 3.5.1). The Iron is also used to identify the tails of hadronic showers that leak out of the LAr by measuring ionisation energies of particles passing through the chambers. For this reason the system is also referred to as the "Tail Catcher". The Iron's energy resolution is $\frac{\sigma(E)}{E} \sim \frac{100}{\sqrt{E}}$.

3.3.4 The PLUG Calorimeter

The PLUG calorimeter is made of eight 7.5 cm thick layers of copper absorber alternated with nine layers of silicon sampling sheets. It is used to minimise missing hadronic momentum in the forward direction. The angular range of the PLUG covers the region between the LAr and the beam pipe, providing acceptance over $0.75 < \theta < 3.4°$.

3.4 Tracking in the H1 Detector

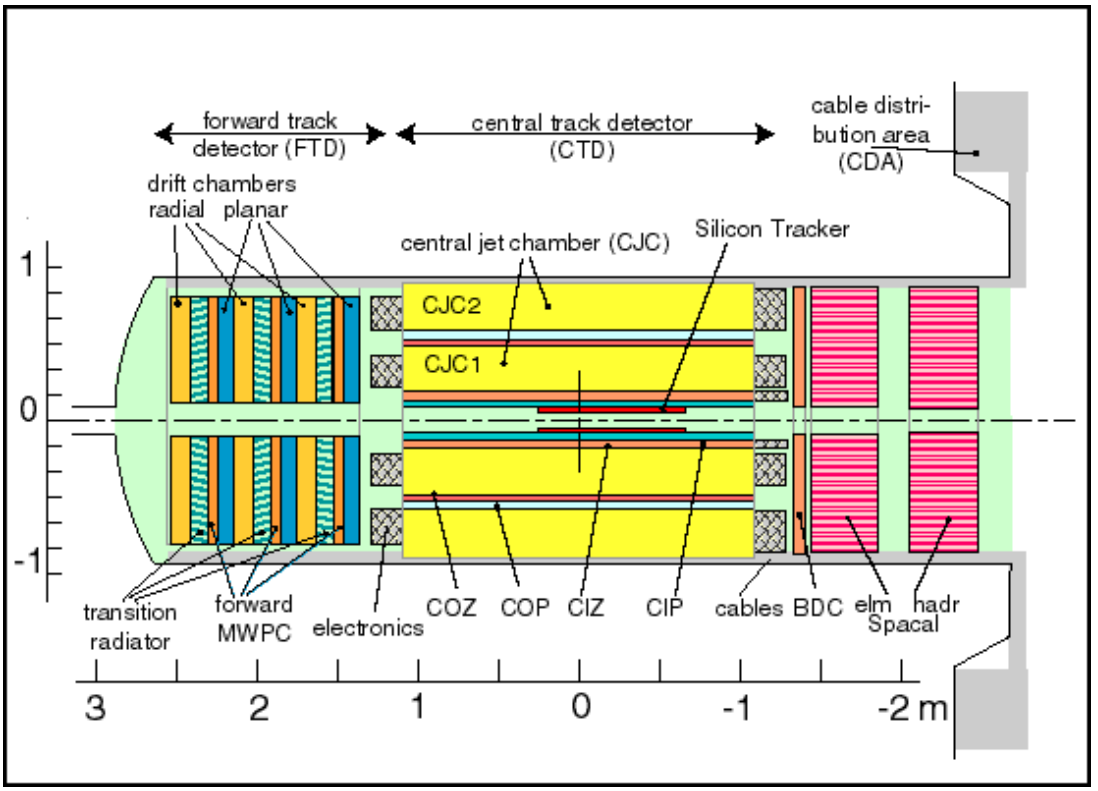

Figure 3.5: The H1 Tracking Detectors

The goal of the tracking system, illustrated in figure 3.5, is to precisely reconstruct tracks associated with charged particles, in order to measure their momenta. The two most important H1 trackers are the Central Tracking Detector (CTD) which covers the angular region $15 < \theta < 165°$ and the Forward Tracking Detector (FTD) ($7 < \theta < 25°$) both of which consist of drift chambers and multi-wire proportional chambers (MWPCs). In addition to these trackers there is the backward drift chamber (BDC) which provides an angular coverage of $135 < \theta < 177.5°$ (not used in this analysis), and the Silicon Trackers which aid the identification of primary and secondary vertices.

MWPCs, instruments for measuring particle positions with fast response times, are comprised of anode wires spread evenly between cathode plates. In the resulting electric field, charged particles crossing the MWPC produce ionisation in the form of electrons, which accelerate to the nearest anode. Hence knowing which wire produces the corresponding signal allows position determination. Wire spacing is, however, limited by the electrostatic forces involved. Their fast response times promote their use as triggering devices.

Drift chambers, tracking devices with high spatial resolution, contain remotely spaced anode wires which lie between two parallel rows of cathode wires, enclosed by screening electrode plates. The electric field is approximately uniform so track position can be determined from the known time of the *ep* interaction yielding the track, the arrival time of the signal at the anode and the near constant velocity at which the ionisation drifts towards the anode. Particle momenta are deduced from the degree of curvature observed in the detector (due to the magnetic field) and particles are identified by determining characteristic energy losses ($\frac{dE}{dx}$) which occur whilst passing through the chamber.

3.4.1 The Central Tracking Detector (CTD)

The central tracking detector provides tracking for the central region defined as $25 < \theta < 155°$. It is comprised of two Central Jet drift Chambers (CJC1 and 2), two MWPCs (CIP and COP), and two concentric z drift chambers (CIZ and COZ).

CJC 1 and 2 are 2200 mm long drift chambers, which start at z = -1125 mm and lie along the z axis. The inner chamber (CJC1) comprises 30 cells, with 24 sense wires running parallel to the z axis. CJC2 has 60 cells and 32 sense wires, also parallel to z. The CJC cells are aligned at 30° to the radial direction, so that ionisation electrons drift almost perpendicularly to the high momentum tracks. The CJCs have a radial resolution of $\sigma_{r\phi} = 170$ μm and a z resolution of $\sigma_z = 22$ mm. The poorer z resolution is due to the fact that the z measurements can only be made by charge division for the wires which are parallel to z. From the drift time the event timing can be determined to within 1ns, and from this the interaction time (T_0) can be determined. The momentum of charged particles can be calculated from the curvature of the track in the solenoid's magnetic field. The resolution of the transverse momentum is $\sigma_{p_T}/p_T < 0.01\ p_T$ in GeV, while the dE/dx resolution is around 7% for a minimum ionising particle [39].

The Inner (CIZ) and Outer (COZ) z chambers are drift chambers with sense wires per-

pendicular to the z axis. The CIZ consists of 15 12 cm long four layer concentric rings around the beam axis. The COZ consists of 24 9 cm long four layer concentric rings. The z chambers are used to obtain a good polar angle determination due to their precise determination of the particle positioning in z. The z-position is determined from the drift time with a resolution of $\sigma_z = 0.26$ mm.

The Central Proportional Chambers (CIP and COP) are MWPCs providing a fast timing signal with a time resolution of 21 ns. Since this resolution is much smaller than the bunch crossing interval they are used to accurately determine bunch crossings. A combination of wires hit in the CIP, COP, and forward proportional chamber (FWPC) is used to trigger on charged particles from the interaction point.

3.4.2 The Forward Tracking Detector (FTD)

Because of H1's highly asymmetric beam conditions, enhanced tracking equipment is required in the forward direction. Up to the 2000-2002 upgrade, the FTD comprised three super-modules each consisting of 12 layers of planar drift chambers, a layer of MWPCs, passive transition radiators and 12 layers of radial drift chambers [40]. In the planars, the sense wires are positioned in parallel in the r-ϕ plane, and the planar drift chambers are staggered by 60^o in ϕ with respect to one another for accurate spatial co-ordinate measurements. The radial chambers contain 48 sense wires strung radially and provide accurate azimuthal angle measurements. The single hit resolutions of the planar and radial drift chambers are 170 μm and 200 μm respectively.

3.4.3 The Silicon Trackers

In order to improve the identification of primary and secondary vertices, two silicon trackers [41], the Central Silicon Tracker (CST) and the Backward Silicon Tracker (BST), were added to the H1 tracking system in 1996.

The CST, which consists of 2 layers of silicon strip detectors covering the range $20 < \theta < 150°$, provides information on the primary vertex by accurately measuring the tracks of charged particles close to the vertex as well as aiding in the identification of heavy flavour particles via observation of the secondary vertices produced in their decays. The BST, consisting of eight planes of silicon discs, is used in the reconstruction of backward scattered electrons in the region of the SPACAL with polar angles of $162 < \theta < 176°$.

3.5 The Muon Detectors

3.5.1 The Instrumented Iron

The Iron Return Yoke (introduced in section 3.3.3) is also used to detect muons. The central muon trigger searches for track segments using 5 of the 16 layers in each of the six regions (inner, outer, forward and backward end-cap, and forward and backward barrel) to reconstruct the iron tracks used to identify muons.

3.5.2 The Forward Muon Detector

The Forward Muon Detector (FMD) is situated outside the Instrumented Iron, and provides coverage for the region $3 < \theta < 17°$, which is the highly active region of the outgoing proton. The FMD allows muon identification both independently and from extrapolated FTD tracks, by taking advantage of the fact that most hadrons do not penetrate the iron to reach the FMD.

The FMD is comprised of six double layer drift chambers, three either side of a toroid magnet which provides a magnetic field of 1.5 Tesla. The magnetic field from the toroid curves the muons tracks, allowing a momentum measurement that is independent of the other trackers. The FMD can measure momenta in the range of $5 - 100$ GeV. The lower limit is due to multiple Coulomb scattering, with muons loosing on average 3 GeV in the main detector and 1.5 GeV in the toroid. The upper limit is set by the angle through which a high momentum muon can be deflected by the toroid.

The drift chambers are made up of drift cells, each cell being 20 mm deep and 120 mm wide with a sense wire located in the middle. The cells have a spatial resolution of ≈ 250 μm if using drift time, and ≈ 4 cm from charge division. The two layers of each chamber section are offset with respect to the other so as to eliminate the ambiguity of which side of the sense wire the muon has passed.

Four of the six drift chambers, two either side of the toroid, have their sense wires strung tangentially to the beampipe, to accurately measure θ. The other two chambers, one on each side of the toroid, have sense wires strung azimuthally, to accurately measure ϕ.

3.6 The Luminosity System

The Lumi System is comprised of an electron tagging calorimeter (ET) and a photon detecting calorimeter (PD). The ET is located next to the electron beam pipe at $z = -33.4$ m, and consists of 49 crystals covering a total area of 154×154 mm^2. The PD is built out of 25 crystals and covers an area of 100×100 mm^2, a depth of 22 radiation lengths, and is situated at $z = -102.9$ m. The luminosity is measured using the PD only,

to determine the rate of Bethe-Heitler ($ep \rightarrow ep\gamma$) events (a precisely calculated QED interaction with a high cross section). It is verified by using events with coincident signals in the ET and PD. The PD is protected by a lead filter and a water Cherenkov Veto Counter (VC). The lead filter protects the PD from the high rate of synchrotron radiation. The Lumi System provides a fast on-line luminosity measurement with a precision of 2% at nominal beam conditions. An offline correction to the luminosity is made to take into account the luminosity from satellite bunches [42].

Electrons from photoproduction interactions in the elasticity range of $0.3 \leq y \leq 0.7$ are also measured in the ET, and it is thus also used to study photoproduction background contamination in this analysis. The Lumi system is also used to measure the luminosity with an accuracy of 1.5%, to provide electron beam monitoring for the HERA machine and energy measurement of photons from initial state radiation and electrons scattered under small angles. There are two additional electron taggers situated at $z = -44$ m and $z = -8$ m which are used to measure electrons of higher and lower energies (respectively) than the ET at $z = -33.4$ m for photoproduction studies. They are not used in this analysis.

3.7 The Time-of-Flight System (ToF)

The ToF is comprised of three scintillators positioned along the beamline and two scintillator walls ("Veto Walls"). The Veto Walls are positioned at z = -810 cm and $z = -650$ cm, while the backward ToF (BToF) is at z = -275 cm, the plug ToF (PToF) is at $z = 540$ cm and the forward ToF (FToF) is positioned at $z = 790$ cm. All the scintillators have a good time resolution of around 1 ns and are used to reject beam induced background which arrives out of time in the H1 detector.

3.8 Triggering at H1

3.8.1 The H1 Trigger

The HERA bunch crossing interval is 96 ns (roughly a frequency of ~ 10 MHz) and is more than an order of magnitude smaller than the time needed by the H1 detector to write out information from its various components. Additionally, the majority of events detected by H1 are background, mostly caused by synchrotron radiation, cosmic muons and muons from proton halos and proton induced background (proton-beam wall interactions, and proton-gas particle interactions, referred to as "beam-wall" and "beam-gas" interaction respectively). Since background processes have a rate 10^4 times higher than proton-electron collisions, it is essential to trigger on interesting collisions in a manner that minimises deadtime. For this purpose, the H1 detector uses a pipelined, multi-layered, trigger system, illustrated in figure 3.6.

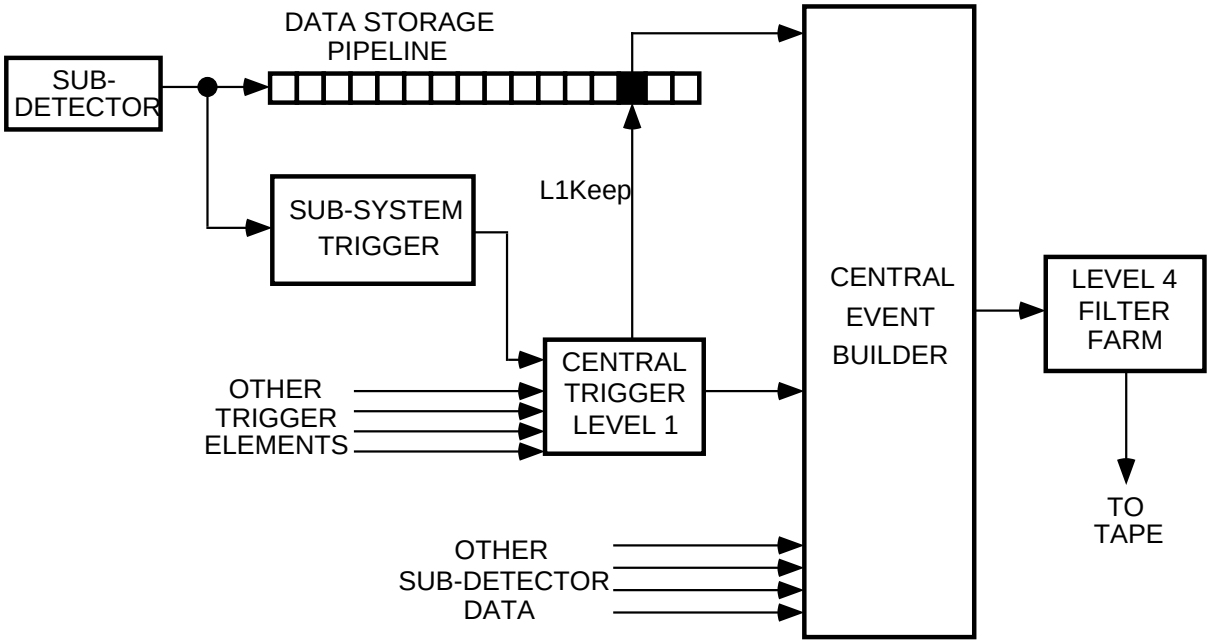

Figure 3.6: The H1 Triggering System (L2 components not shown)

A first trigger level (L1) decision is taken in 2 μs, and events are selected using information provided by the different subdetectors (the subdetector information is referred to as "trigger elements". A selection of trigger elements which are important to this analysis are described in section 3.8.2). The Central Trigger Logic (CTL) combines the $\sim$ 200 trigger elements into 128 different subtriggers. The L1 readout time is 24 times slower than the rate of Bunch Crossings. Therefore the detector readout information is pipelined until the CTL makes its decision, such that the detector can remain sensitive to new collisions. If any of the L1 subtrigger conditions are met (any of the L1 subtriggers fire) the pipeline is stopped and the event is passed to the level 2 trigger. The L1 trigger level is deadtime free, as rejected events are simply overwritten in the pipeline after the CTL decision is made. Deadtime only begins when a L1 decision is made to keep the event, and it is passed on to the second trigger level.

The second trigger level (L2) operates during the readout deadtime. The L2 trigger uses more detailed information sent by each subdetector. The increase in time taken to make a L2 decision, 20μs, allows subtriggers to be combined to form a topological trigger (L2TT) [43], which employs pattern recognition using a 2D projection of the event in θ and ϕ, and a neural network trigger (L2NN) [44]. At L2 it is possible to end the deadtime and reactivate the pipeline through a L2 kill decision, or to keep the event (L2 keep) at which point the event is sent to the Central Event Builder (CEB). Once the event is written to the CEB deadtime ends and further filtering takes place asynchronously to the bunch crossing. The overall H1 deadtime is usually about 10% for normal operation.

From the conception of H1, it was planned to have a third level trigger (L3) that would make a decision in $\sim$2 ms. This trigger level was not implemented during the HERA-I running (1994-1999), but will be used by the Fast Track Trigger (FTT) [45], a part of the

HERA-II/H1 upgrade program [46] which is detailed in chapter 9.

The fourth trigger level (L4) is run asynchronously to the HERA machine on a filter farm of 30 PCs, which make use of the full event information to perform a partial reconstruction. At this level an entirely software based trigger verifies the L1 decision using the additional information. Algorithms similar to offline analysis are used to select events. Events that pass the L4 trigger are written to tape (referred to as "Raw Data") at a rate of 10-20 Hz.

The fifth trigger level (L5) runs completely offline, and is applied to the Raw Data before it is stored in an analysis-ready format. At L5 the Raw Data files go through a full event reconstruction using the full detector information and events are subdivided into physics event classes. Only events which have been allocated to a physics class are written to DST or ODS, the data-files used for physics analysis in FORTRAN and C++ respectively. Approximately 1% of all events rejected by the L4 and L5 triggers are retained for monitoring purposes.

3.8.2 Trigger Elements Important to the NC Analysis

In the following paragraphs a non-exhaustive selection of important NC trigger elements is briefly descried. The LAr trigger elements (LAr_el1&2, LAr_T0, LAr_Etmiss and LAr_BR) are described first, followed by the track-based trigger elements (zvtx_T0, FwdRay_T0, DCRϕ_T0 and DCRϕ_TC) and finally the veto conditions (Veto_Wall, Fwd_ToF, VLQ_ToF, RZ_veto, CIP_no_SPACAL and SPACAL_ToF).

The LAr Trigger Elements.

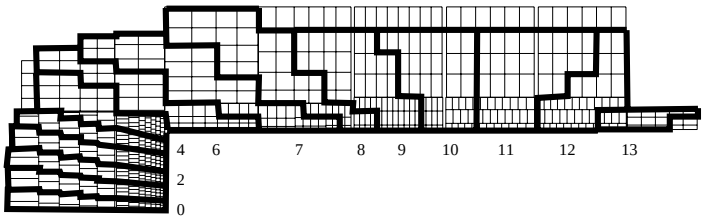

Figure 3.7: A side view of the LAr in the $y-z$ plane. The thick lines show the borders of the different towers.

The LAr provides signals to the central trigger which are used for the triggering of NC events. The signals of 16 neighbouring LAr cells are combined into trigger cells (TCs). These TCs are combined to form trigger towers in such a way that the trigger tower points towards the nominal vertex, as shown in figure 3.7. The analog signals of up to four neighbouring trigger towers are summed and then digitised using FADCs (flash analog to digital converter). These FADCs are then summed into Big Towers. A detailed description of the LAr trigger and its performance can be found in [47].

The LAr_el trigger elements fire if the energy in one trigger tower exceeds a threshold value. In the backward region these thresholds are set to a minimum of 6 GeV for the

LAr_el1 and 7.5 GeV for the LAr_el2 trigger elements. The thresholds are increased in the forward region because of the large beam-induced background.

The LAr_T0 TE provides a timing signal which is determined from the trigger tower signals. The trigger tower T_0s are combined to form the Big Tower T_0, with the LAr_T0 firing when at least one Big Tower T_0 is set.

The LAr_Etmiss trigger element fires on events with a missing transverse energy, measured by the Big Towers, in excess of 6 GeV.

The LAr_BR (LAr Big Ray) trigger element combines the energy measurement in a trigger tower with a track candidate from the DCRϕ trigger (described below). LAr_BR fires if the trigger tower energy exceeds 1 GeV and is matched in polar and azimuthal angle by a DCRϕ track candidate.

The Track-Based Trigger Elements.

The CJCs, CIP/COP, CIZ/COZ and FWPC all provide information to the CTL.

The zvtx_T0 trigger element [48] is based on signals from the MWPCs. As every particle track in the central region passes through at least four layers of MWPC, track candidates can be formed from the chamber signals and allow a fast determination of the event vertex. All track candidates corresponding to real tracks have a common vertex, whereas the origins of track candidates formed by random coincidences are broadly distributed along the z-axis.

The FwdRay_T0 trigger element is similar to the zvtx_T0, but uses only signals from the FWPC. The FwdRay_T0 is usually used in combination with the zvtx_T0, with the logical OR of the two forming the Ray_T0.

The DCRϕ_T0 and DCRϕ_TC trigger elements use signals from the CJC. The TC trigger element fires when three track candidates with a transverse energy greater than 420 MeV are reconstructed. The T0 trigger element fires on one or more track candidates with both a transverse momentum larger than 420 MeV and a timing verification of the track candidate coincidences in the CJC layers, called a "prompt bit" [49].

The Veto Conditions

Veto Conditions are applied to all of the NC subtriggers. They are used to reject background from beam-gas and beam-wall interactions. The Veto Conditions fire on suspected background and are therefore used with a logical NOT in the construction of subtriggers.

Because the scintillators have a very good time resolution, the Veto_Wall, Fwd_ToF and VLQ_ToF can fire to reject beam induced background which arrives out of time in the detector.

The RZ_veto uses CIZ and COZ information to reject events for which the vertex is not reconstructed in the nominal vertex region.

The CIP_no_SPACAL fires on events which have high track multiplicity in the backward region of the CIP but no energy deposit in the SPACAL. The SPACAL_ToF rejects events with energy deposits in the SPACAL that occur in a time window that does not coincide with the interaction.

Chapter 4

Monte Carlo Simulation

To study different physics models and in particular to compare these models to experimental data, stochastic techniques are employed. These techniques, which use random numbers and probability distributions are termed Monte Carlo (MC) methods. Simulated event samples are generally required to be several times the size of the data samples in order to ensure that the statistical error of the simulated sample can be, to a good approximation, ignored.

The simulation of real physics processes can be divided into two parts, the simulation of generator (Gen) level events and reconstructed (Rec) level events. Firstly, event generators produce all final state partons for the given interaction, using all relevant diagrams and parton distribution functions (PDFs). Hadronisation, whereby the partons produced fragment and form hadrons, is further simulated until only long lived stable particles exist. In this analysis hadronisation is performed using the JETSET [50] programme, which uses the LUND string model of hadronisation [51]. The Monte Carlo "event" then consists of a list of 4-vectors describing the final state particles. This is termed a Generator Level event.

To make a useful comparison to the data, the interaction of the generator level final state within the H1 detector is modelled using the H1SIM package [52] based on the simulation package GEANT3 [53]. H1SIM models the interaction of the particles in each of the subdetectors. Finally, a full reconstruction of the event is carried out using the reconstruction software package H1REC to provide a level of simulation that is directly comparable to the recorded DST data (see section 3.8). The outcome of this process is a Reconstructed Level event and at this point the MC sample is ready to undergo the same selection criteria as the data. The differences between the two levels of simulation provide a method of correcting the data for detector acceptances and resolution effects (see section 7.2).

In the case of NC DIS, Monte Carlo "model" events are generated using the DJANGO programme [54], simulating $\sim$ 400,000 events for this analysis. DJANGO is an interface between the HERACLES [55] *ep* event generator, which includes QED radiative effects, and the ARIADNE [56] implementation of the Colour Dipole Model [56 – 59], used to

simulate QCD radiation. The input PDFs used were extracted from a next to leading order QCD DGLAP fit to previous measurements of NC data made with the H1 detector [60].

Several datasets were generated so that the statistical error on the MC prediction is smaller than that for the data for all values of x and Q^2. At low Q^2 an integrated luminosity of ~ 100 pb^{-1} was generated, while at higher Q^2 additional MC datasets are included amounting to up to 350 times the data luminosity.

Several background MC were used, to describe the different types of backgrounds that can be present in the NC selection. Background can arise from both ep and non-ep interactions. The most common sources of ep background are photoproduction, low Q^2 DIS, QED-Comptons, photon-photon interactions, and W and Z boson production.

Photoproduction events are an important background source which arise from ep interactions at very low Q^2 ($Q^2 \sim 0$ GeV^2). Generally the electron is scattered through a very small angle so that it is not detected in the central part of the H1 detector, but this process can be misidentified as DIS, for example when a π^0 from the hadronic final state fakes a LAr electron. Photoproduction events are generated by PYTHIA [61] using GRV LO [62] parton distributions for the proton and photon. More details on photoproduction can be found in [63].

In "low" Q^2 DIS events, $Q^2 \leq 100$ GeV^2, the electron is scattered through a small angle and detected in the SPACAL. Events with SPACAL scattered electrons are rejected in this analysis (see section 6.2). However a highly energetic π^0 can fake an electron in the LAr, which can be misidentified as the scattered electron. Low Q^2 DIS is generated by DJANGO.

Elastic QED-Comptons ($ep \to ep\gamma$) are treated as background since the exchange photon has a very low virtuality ($Q^2 \approx 0$). The final state electron and photon can be scattered through a large angle into the LAr if the intermediary electron is highly virtual. These events are used in the calibration of the electron energy measurement. The inelastic part of the QED-Compton cross section, where the proton does not remain intact, is treated as part of the signal. QED-Comptons are generated by the COMPTON programme [64].

Photon-photon interactions ($\gamma\gamma$) contribute to the background due to the mechanism $\gamma\gamma \to l^+l^-$. When the final state lepton pair is e^+e^- this background can contribute to the NC channel. These events are also used in electron energy calibration. $\gamma\gamma$ interactions are generated using LPAIR [65].

Finally, real W and Z bosons are produced at HERA with a very low cross section ($\sigma \approx 1$ and 0.1 pb^{-1} for W and Z production respectively). The scattered electron is usually undetected, but if the boson decays leptonically the event may be misidentified as a NC event, and is therefore treated as a background source. These events are generated using the EPVEC programme [66], but do not contribute significantly to the NC sample.

Chapter 5

Kinematic Reconstruction Methods

To accurately measure the cross section a precise reconstruction of the kinematic variables (Q^2, x, y) is needed. The cross section can be described using any two of these variables. In this analysis Q^2 and x are chosen. H1 records final state information for both the electron and the hadronic system, either of which can be used to determine the kinematic variables. H1 kinematics are thus over-constrained. The different kinematic reconstruction methods have different sensitivities to the QED radiation effects of the incoming and scattered electron. The reconstruction methods used in this analysis are outlined below:

5.1 The Electron Method

The electron method [67] determines the kinematic variables using the initial electron energy, E_e, the scattered electron energy, E'_e and the polar angle of the scattered electron, θ_e.

$$Q^2{}_e = 4E_e E'_e \cos\left(\frac{\theta_e}{2}\right)^2 \qquad y_e = 1 - \frac{E'_e}{E_e}(1 - \cos\theta_e) \qquad x_e = \frac{Q^2{}_e}{y_e s} \tag{5.1}$$

The x and y resolutions degrade significantly at low y as there is a $1/y$ dependence to the derivative of y_e determined with respect to either E_e or θ_e. The $Q^2{}_e$ resolution is, however, good over the full kinematic range.

5.2 The Hadronic Method

The hadronic method [68], also called the Jacquet-Blondel method [69], uses hadronic final state information and the incoming electron energy to determine the kinematics.

The Hadronic final state is described in terms of the total transverse momentum of the hadronic final state, $P_{T,h}$, the sum of the energy minus the z component of the momentum of all final state hadronic particles, Σ, and the hadronic polar angle, γ_h:

$$P_{T,h} = \sqrt{(\sum_i p_{x,i})^2 + (\sum_i p_{y,i})^2} \qquad \Sigma = \sum_i (E_i - p_{z,i}) \qquad \gamma_h = 2\tan^{-1}\frac{\Sigma}{P_{T,h}} \tag{5.2}$$

where $E_i, p_{x,i}, p_{y,i}$ and $p_{z,i}$ are the energy and momentum components (in the x, y and z Cartesian co-ordinates) of the hadronic particle i. The summation is over all the final state particles, except the scattered lepton, and particle masses are neglected.

The kinematic variables are determined from hadronic information according to

$$y_h = \frac{\Sigma}{2E_e} \qquad {Q^2}_h = \frac{P_{T,h}^2}{1-y_h} \qquad x_h = \frac{{Q^2}_h}{sy_h}. \tag{5.3}$$

The hadronic method is used in the CC analysis, but is not the best kinematic method for NC cross section measurement because the Q^2 and x resolutions degrade rapidly with increasing y and Σ and $P_{T,h}$ are poorly resolved compared to the electron quantities. It is only used in this analysis for control plots, to ensure that the Monte Carlo model accurately describes the hadronic system.

5.3 The Double Angle Method

The double angle (DA) method [70] determines the kinematic variables using only the hadronic and electron angles, γ_h and θ_e

$$\begin{aligned} y_{DA} &= \frac{\sin\theta_e(1-\cos\gamma_h)}{\sin\gamma_h + \sin\theta_e - \sin(\theta_e - \gamma_h)} \\ {Q^2}_{DA} &= \frac{4E_e^2 \sin\gamma_h(1+\cos\theta_e)}{\sin\gamma_h + \sin\theta_e - \sin(\theta_e - \gamma_h)} \\ x_{DA} &= \frac{{Q^2}_{DA}}{sy_{DA}}. \end{aligned} \tag{5.4}$$

As this method uses only the angles of the final state particles, and not their momenta, it is energy independent and therefore insensitive to energy scale uncertainties. The DA kinematics can be used to determine the energy of the scattered electron, and this E_{DA} is thus used in the energy calibration of the LAr. It is calculated from

$$E_{DA} = \frac{2E_e \sin\gamma_h}{\sin\gamma_h + \sin\theta_e - \sin(\theta_e - \gamma_h)}. \tag{5.5}$$

The DA method does suffer from a degradation in Q^2 and x resolution at both small and large angles. It is however good at medium values of y, where all the final state information is well contained in the LAr.

5.4 The Σ Method

Another method that uses both electron and hadronic final state information is the Σ method [71], which defines the kinematic variables as

$$y_\Sigma = \frac{\Sigma}{E - p_z} \qquad {Q^2}_\Sigma = \frac{(E'_e \sin\theta_e)^2}{1 - y_\Sigma} \qquad x_\Sigma = \frac{{Q^2}_\Sigma}{s y_\Sigma} \tag{5.6}$$

where $E - p_z = \Sigma + E'_e(1 - \cos\theta_e)$, the summed energy minus the longitudinal momentum of all the particles (including the scattered electron), which is expected to be $2E_e$ in a perfectly hermetic detector (ignoring QED radiation effects). The advantage of this method is that as both the y and Q^2 determinations are independent of the incident electron beam energy, there is less sensitivity to radiative effects. The y resolution nears that of the hadronic method at low y, and that of the electron method at high y, and is therefore reasonable for the entire y range.

5.5 Comparing the Methods

The y dependences of the Q^2 and x resolution of the different kinematic reconstruction methods are compared in figure 5.1 [72] (obtained using the DJANGO MC). The best Q^2 resolution is obtained using the electron method. The Σ method also has a good Q^2 resolution, while the hadronic method has a poor Q^2 resolution.

The x_e resolution is poor at low y due to the $1/y$ dependence described above. The Σ method has a good resolution in x across the entire y range, increasing at low y, but not to the level of the electron method resolution. The x_h resolution is as good as that of the Σ method for the lowest values of y, but is inappropriate at high y where the hadronic resolution is up to six times worse than that of the electron and Σ methods.

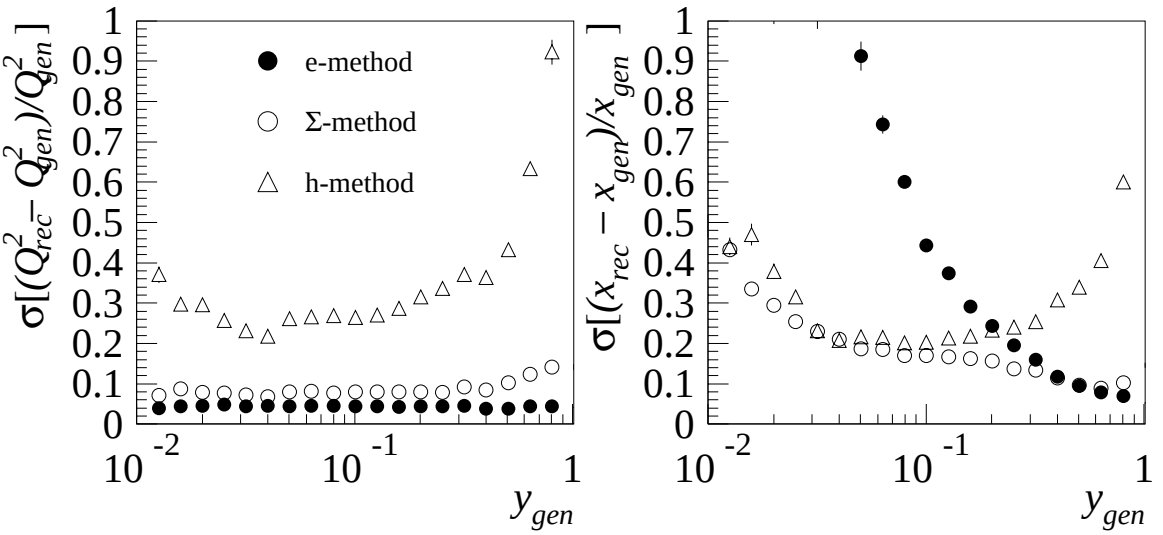

Figure 5.1: The resolution in Q^2 (left) and x (right), plotted as a function of y for different reconstruction methods.

5.6 The $e\Sigma$ Method

The $e\Sigma$ method [73] uses the best method available for determining x and Q^2, as illustrated in figure 5.1, and combines them to determine a value of y:

$$Q^2{}_{e\Sigma} = Q^2{}_e \qquad x_{e\Sigma} = x_\Sigma \qquad y_{e\Sigma} = Q^2{}_e/sx_\Sigma \tag{5.7}$$

As this method yields the very best determination of the kinematic variables, it is the method used for measurements in this analysis.

Chapter 6

Event Selection

6.1 Introduction

In this chapter the methods used to select high Q^2 NC DIS events and reduce backgrounds, are presented. The fundamental requirement of the high Q^2 NC event sample is a high energy electron candidate in the LAr. Additional kinematic, fiducial, run-based and trigger efficiency cuts are then imposed. This section begins by describing the electron finding algorithm used. Next the selection of data periods in which the detectors are fully functioning is presented, as are the trigger requirements for the neutral current sample. Following this, the vertex and track-cluster linking requirements are outlined, which both greatly reduce background contamination in the sample. Further background reduction techniques are discussed and the full set of NC cut criteria are summarised. Finally the calibration techniques applied to the electron and hadronic energy and polar angle measurements are described and a selection of plots comparing the data and simulation distributions for important kinematic variables are presented.

6.2 The Electron Finder

The criteria for identifying a high Q^2 electron are based solely on calorimeter topology, looking for a compact and isolated energy deposit in the electromagnetic part of the LAr, with little or no deposit in the part of the hadronic LAr directly behind the electron candidate. This analysis uses the electron finder QESCAT [74], which employs estimator variables that quantify the shower-shape properties of the electron candidate and then performs a selection based on these variables.

The seven estimator variables are NCEL, EAEM, EAHN, EATR, EAIF, EAHD and EATOT. They are used to specify the requirements for a compact cluster with limited transverse and longitudinal dispersion. The total energy of the electron candidate cluster, EATOT, is required to be greater than 5 GeV and NCEL, the number of cells assigned

to the candidate, must be greater than 3. It is further required that the fraction of the total energy which is contained in the first two layers of the EMC (first three layers in the forward region), EAEM, be large; and that the fraction of the energy in the four most energetic cells, EAHN, also be large. Finally, the transverse dispersion of the cluster, EATR, is constrained to be small. EATR is defined as

$$\mathrm{EATR} = \sqrt{\sum \left(\frac{E_i R_i}{V_i}\right)^2 - \left(\sum \frac{E_i R_i}{V_i}\right)^2}, \tag{6.1}$$

where E is the energy in the cell, R is the radius of the cell, V is the volume of the cell and the summation is over all cells of the electron candidate.

Once the initial electron candidate has been identified an isolation cone, defined in $\eta - \phi$ space, is used to sample the calorimeter deposits surrounding the cluster. The energies of all hadronic cells within a radius of $\sqrt{(\eta_{clus} - \eta_{cell})^2 + (\phi_{clus} - \phi_{cell})^2} = 0.25$ are summed up to define EAHD, which is required to be small. Conversely the ratio of the total energy of the electron candidate to the isolation cone energy, EAIF, should be large. The exact values of the selection criteria are outlined in table 6.1.

Estimator variable	*Description*	*Cut value*
EATOT	total cluster energy	must be > 5 GeV
EAEM	energy fraction in first 2 (3 in IF) layers of the EMC	$>0.94 + 0.05\cos 2\theta$
EAHN	energy fraction in the four most energetic cells	>0.4 (0.8 in fwd region)
EATR	transverse dispersion	<7.5 (<3 in fwd region)
NCEL	Number of cells assigned to electron candidate	>3
EAIF	Electron candidate energy fraction in isolation cone of radius 0.25	>0.98
EAHD	Hadronic energy in isolation cone	$\leq$ 300MeV

Table 6.1: The cluster estimators, their descriptions and the cut values which are used by QESCAT.

These selection criteria are loosened in the forward region of the LAr, due to the limited resolution in that region. If there is more than one electron candidate identified by QESCAT, the most energetic is considered to be the scattered electron.

The efficiency of finding high energy electrons using QESCAT is found to be $> 99\%$ [72], except for the regions where an electron can directly enter the hadronic part of the calorimeter without interacting with the electromagnetic section. Electrons found in these detector regions, mostly the cracks between calorimeter octants, are removed from the event sample. These cuts are refered to as the phi-cracks cuts. The probability of misidentifying a hadronic cluster as an electron, determined by using a simulation of NC

events, is found to be less than 2% [72]. This is further reduced by requiring that there be a track that points to the electromagnetic cluster, as described in section 6.5

6.3 The Run Selection

A selection was imposed upon the data used in this analysis, requiring that the essential subdetectors were fully functioning during data-taking. The essential subdetectors are the LAr and SPACAL calorimeters, the CTD, the luminosity system and the ToF. The LAr, SPACAL and CTD are used to accurately measure the final state, as well as helping to reduce backgrounds. The luminosity system is needed for an accurate luminosity measurement and the ToF is vital in reducing backgrounds. A full description of background reduction can be found in section 6.6. The high Q^2 NC triggers, outlined in the next section, were required to be fully operational and periods of data-taking where the triggers were not functioning have been removed.

Finally a check of the number of observed events per unit of luminosity (nb^{-1}), the "NC event yield", has been performed. Figure 6.1 shows the event yield, plotted in bins of equal luminosity. In cases where the event yield of a bin is more than 6σ smaller than the average, the appropriate run period is excluded. This is usually a sign that there was a problem with the data taken during that period of data-taking, defined as a luminosity fill. The event yield can be seen to be roughly constant throughout the luminosity fills, which combine to an integrated luminosity of 65.2 pb^{-1}.

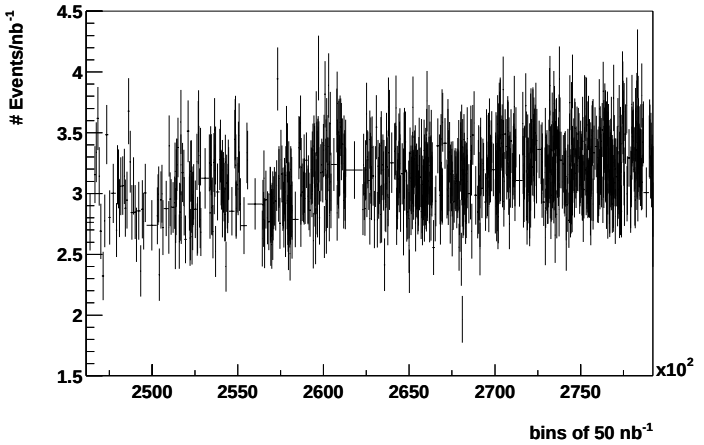

Figure 6.1: The Event Yield, the number of events/nb^{-1} plotted in bins of 50 nb^{-1}.

6.4 The Trigger Selection

The subtriggers (STs) used to select high Q^2 NC events for the 99/00 positron running were ST67, ST71, ST75 and ST77. These subtriggers are combinations of the trigger elements (TEs), defined in section 3.8, relating to electron energy (LAr_el1 and LAr_el2), timing (LAr_T0 and Ray_T0), track conditions and background veto conditions. In simple terms, ST67 fires on an energy deposit in the EMC; ST71 looks for a hadronic cluster in the LAr with a condition on associated tracks and requires a central vertex; ST75 fires if it detects an energy deposit in the EMC and has additional track conditions; and ST77 triggers if it detects missing transverse energy in the LAr. ST77 is an effective trigger because it takes into account that when an electron's energy exceeds the dynamic range of the FADCs it is interpreted as missing energy. The NC subtriggers, their trigger criteria and their trigger element components are listed in table 6.2. The veto conditions have not been included in this table and can be found in [75].

Subtrigger	*Description*	*Trigger Elements*
ST67	Energy in EMC >3.8 GeV	LAr_el1 && (Ray_T0 || LAr_T0)
ST71	Central Vertex && $\geq$ 3Central Tracks with $p_T > 420$MeV && A Track Combined with a Cluster in the LAr	Ray_T0&&LAr_BR&&DCRϕ_TC
ST75	Energy in EMC >2.8GeV && $\geq$ 1 Central Track with $p_T > 420$MeV	LAr_el2 && Ray_T0
ST77	Missing Transverse Energy in the LAr	LAr_etMiss && Ray_T0

Table 6.2: A description of the subtriggers used in this analysis, including the main trigger elements used to construct the subtrigger.

The efficiency of these subtriggers can be determined by measuring the efficiencies of their component trigger elements, for example

$$Eff(\text{ST67}) = Eff(\text{LAr\_el1}) * Eff(\text{Ray\_T0}||\text{LAr\_T0}), \tag{6.2}$$

where the efficiency of $(A||B)$ for independent triggers A and B is determined by

$$Eff(A||B) = Eff(A) + [\{1 - Eff(A)\} * Eff(B)]. \tag{6.3}$$

The efficiency of the trigger elements is obtained from counting the number of events that cause the trigger to fire and comparing these with events that cause an independent monitor trigger (MT) to fire, using

$$Eff(\text{TE}) = \frac{\text{number of events triggered by the [MT\&\&TE]}}{\text{number of events triggered by the MT}}. \tag{6.4}$$

The trigger efficiency of the LAr_el TEs is calculated using ST71 as the monitor trigger. The T0 trigger efficiencies are calculated using the logical AND of ST67 and the Ray_T0 to monitor LAr_T0, and ST67 and the LAr_T0 to monitor the Ray_T0.

The LAr_el Trigger Efficiency

The efficiency of LAr_el1, calculated as a function of the scattered electron energy, is plotted in figure 6.2. There is an obvious threshold near 6 GeV, after which the trigger efficiency increases with energy and plateaus to 100% at $E'_e > 11$ GeV. For this reason, as well as for reasons of background reduction discussed in section 6.6, a cut is imposed on the scattered electron energy, requiring it to be greater than 11 GeV.

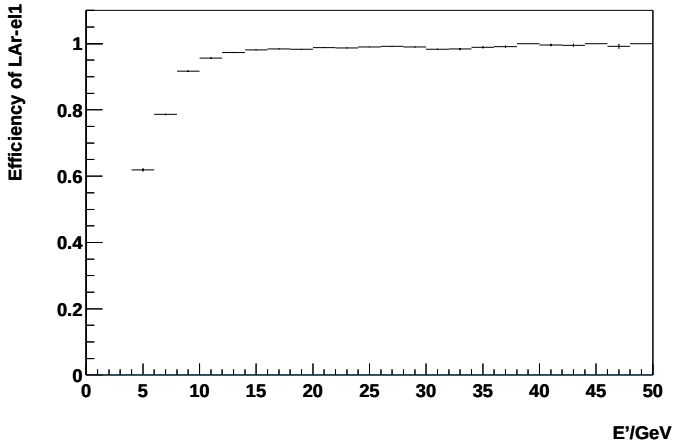

Figure 6.2: The efficiency of trigger element LAr_el1 plotted as a function of the scattered electron energy.

In fact, due to the Q^2-x binning scheme used in this analysis, the electron energy cut is replaced with a requirement in Q^2 and y_e, rejecting events with both Q^2 less than 890 GeV and y_e greater than 0.63. This cut rejects all events with $E'_e < 11$ GeV and also excludes entire bins from the scheme, eliminating the problematics of partially filled bins. This effect is clearly shown in figure 6.3, a plot of the Q^2-x phase-space.

The T0 Trigger Efficiencies

The efficiency of the LAr_T0 and Ray_T0 trigger elements as a function of E'_e and y_h are plotted in figure 6.4. The LAr_T0 TE is strongly dependent on the scattered electron energy, reaching 95 % at 30 GeV. The Ray_T0 efficiency shows a strong dependence on y_h, which is due to the acceptance of the proportional chambers. It is constant at around 98 %, dropping to 95% at low values of y_h, where the hadronic final state is not measured in the central region of the detector. High values of y_h correspond to low values of the scattered electron energy and therefore a region of low LAr_T0 efficiency.

From equation 6.3 it is possible to determine the combined efficiency of the LAr_T0 and Ray_T0 triggers and this is found to be greater than 99% for most of the kinematic range.

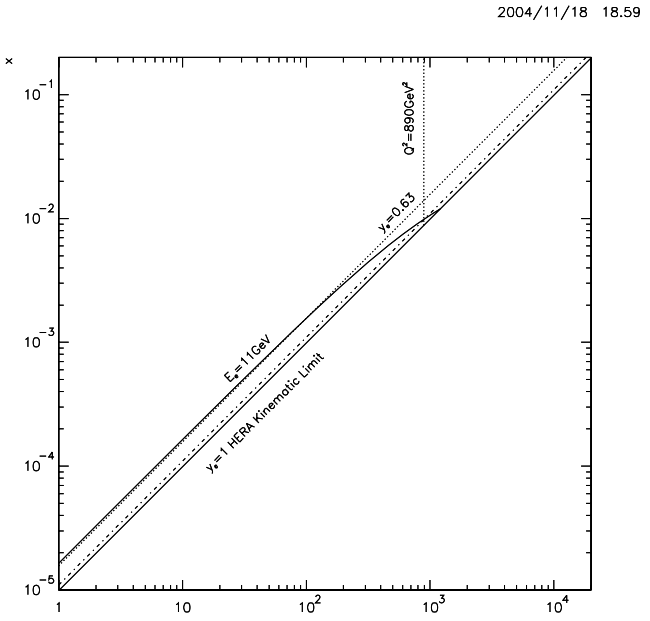

Figure 6.3: A plot of the Q^2-x phase space. The diagonal lines show the HERA limit y=1 (full line), the y=0.9 cut (dots and dashes) and the y=0.63 cut (dotted line). The vertical (dotted) line is the Q^2=890 GeV cut and the curved (full) line is the E'_e=11 GeV limit. The requirement of an electron energy greater than 11 GeV is shown to be accounted for by a cut on both y_e and Q^2.

The remaining small inefficiency at low y_h and scattered electron energy is corrected in the simulation by reweighting the Monte Carlo accordingly.

The total subtrigger inefficiency can be calculated from the energy and timing trigger elements' individual efficiencies using equation 6.2. Due to the energy cut imposed, the

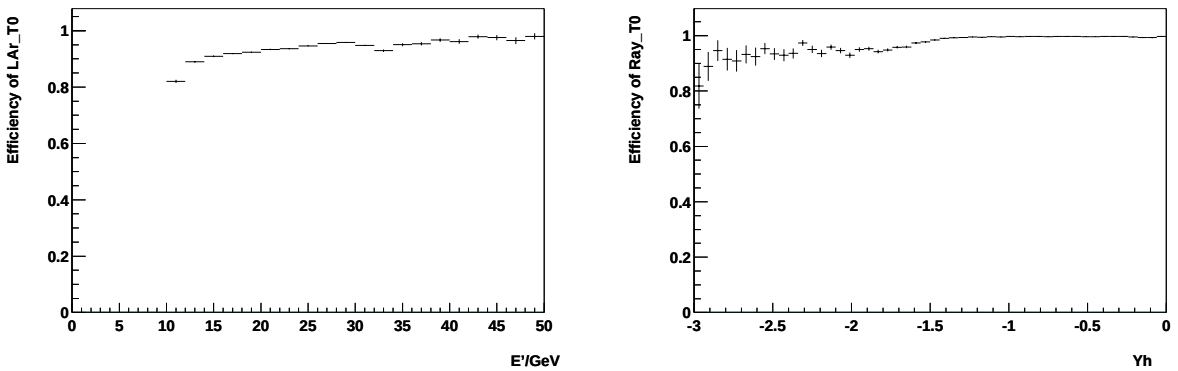

(a) (b)

Figure 6.4: (a) A plot of the LAr_T0 Trigger Element efficiency plotted as a function of scattered electron energy and (b) the Ray_T0 Trigger Element efficiency plotted as a function of y_h

efficiency of the energy trigger elements can be considered to be 100%. The subtrigger efficiency, ignoring the veto contribution, can therefore be considered to be that of the timing trigger elements.

The Veto Conditions

There are two veto conditions applied to all subtriggers, BToF and FToF. The efficiencies of these conditions were studied using short dedicated data taking periods without the conditions applied. The BToF veto was found to have an inefficiency of 0.1%± 0.003% [76] and the FToF an inefficiency of 0.4%±0.4%. The other veto conditions, the veto-wall, RZ-veto, PToF, CiPB-noSPCL and SPACAL-AToF can be studied in greater depth as they are only applied to certain subtriggers. While some of these veto conditions can result in a high ($\sim$ 3%) inefficiency, they are always supported by subtrigger 67 which does not contain these vetoes. Therefore, as the veto-related errors are either very small, or only affect some of the subtriggers, their contribution to the total subtrigger uncertainty is small. To cover these effects, a systematic uncertainty of 0.5% is assigned to the NC trigger efficiency.

The Trigger Efficiency Fiducial Volume Cuts

The trigger element efficiency can also be calculated as a function of ϕ and z, see figure 6.5. The efficiency should not be dependent on z or ϕ (other than in the cracks mentioned above). The reduced trigger efficiency in these z and ϕ regions is due to a missfunctioning of parts of the detector in certain data-taking periods. Therefore, these parts of the detector are removed from the NC sample, for those problematic periods. After applying the trigger efficiency fiducial volume cuts the trigger efficiency can be considered to be 100%.

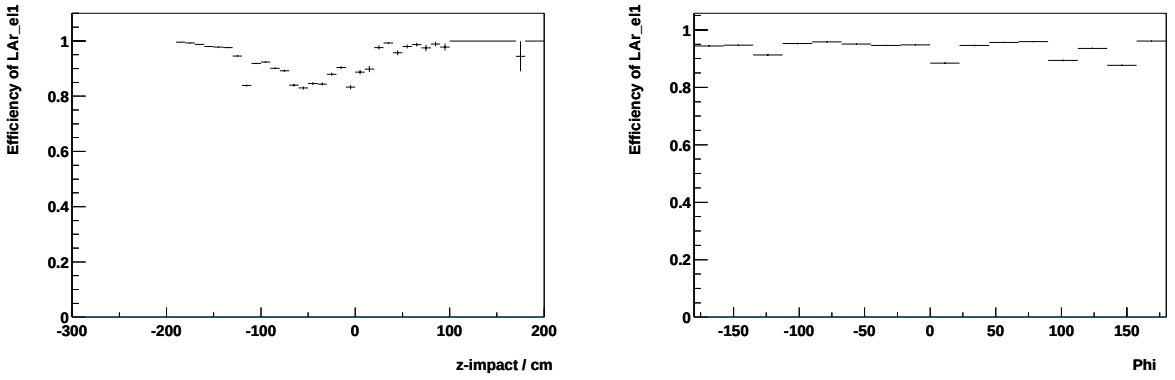

(a) (b)

Figure 6.5: The LAr_el1 Trigger Element efficiency plotted as a function of z-impact (a) and ϕ (b), calculated without imposing fiducial volume cuts.

6.5 Vertex and Track Requirements

A well reconstructed primary interaction vertex is required for the precise measurement of the event kinematics and to reduce non-ep backgrounds. Either a central or a forward vertex is required to ensure high vertex reconstruction efficiency. As there is a shift between the data and Monte Carlo z-vertex distributions, plotted in figure 6.6(a), the Monte Carlo distribution is reweighted to fit the data and the corrected distribution is plotted in figure 6.6(b). A cut of ± 35 cm is applied about the nominal z-vertex position at 1 cm, to ensure a Gaussian-like behaviour. Outside this range the distribution becomes too difficult to model as it includes contributions from satellite bunches which cause large tails.

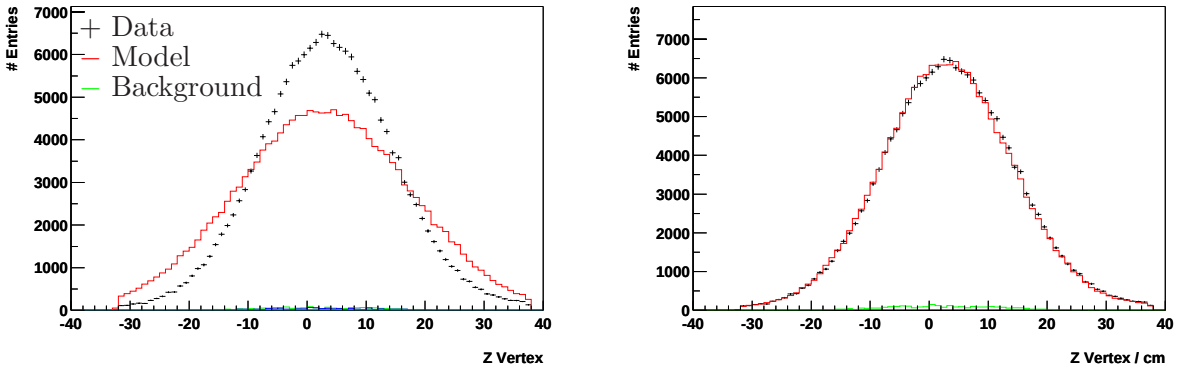

(a) (b)

Figure 6.6: The z-vertex distribution before (a) and after (b) reweighting the Monte Carlo.

To reduce the misidentification of hadrons and photons as electrons, a track-cluster link is required for electrons identified in the central region, $\theta_e > 35°$. The distance of closest approach, DCA, of a track to the electron cluster is used to aid in rejecting misidentified electrons and this value is plotted in figure 6.7 comparing values for data with Model and Background Monte Carlo vertex fitted (DTRA) tracks. At low values of DCA, the background contribution is less than 1%, but this proportion increases as the track-cluster separation increases.

A rather loose cut of DCA < 12cm is chosen, so as to maintain a high selection efficiency. To calculate the selection efficiency a "clean NC sample" selection was used, in which the DCA cut was replaced by a cut of $45 < E - P_z < 65$ GeV and a requirement on the transverse momentum balance, $0.6 < p_{T,h}/p_{T,e} < 1.2$. The efficiency of the DCA cut is shown as a function of polar angle (θ_e) for vertex fitted tracks in figure 6.8.

The average efficiency is 96% for data and 98% for the simulation. This efficiency can be increased by also allowing non-vertex fitted (DTNV) tracks that originate no further than 5 cm from the vertex. The efficiency for either non-vertex or vertex-fitted tracks is found to be just short of 100% for both data and simulation, with the remaining difference applied as a correction to the simulation.

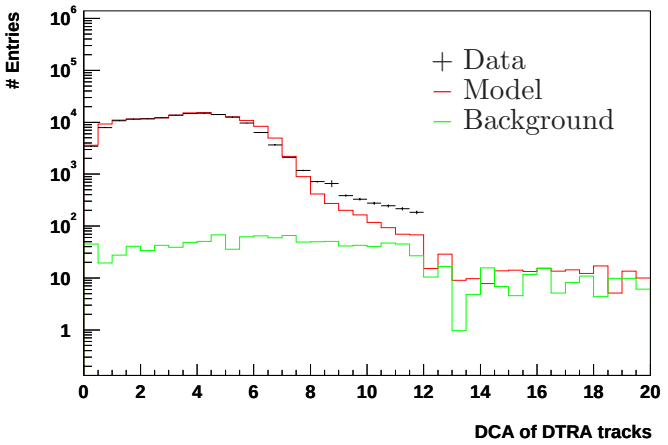

Figure 6.7: The track-cluster DCA in cm, with the number of events plotted on a log scale. The NC DIS model (red line) is compared to the combined background (green line) and they are seen to be of the same order of magnitude at a DCA greater than 12 cm. The data points are plotted up to the cut value of 12 cm. The discrepancy between the data and model points arise from a poor ability to simulate the DCA of DTRA tracks. This discrepancy is larger at low values of DCA, but this is hard to tell due to the log scale used for the y-axis.

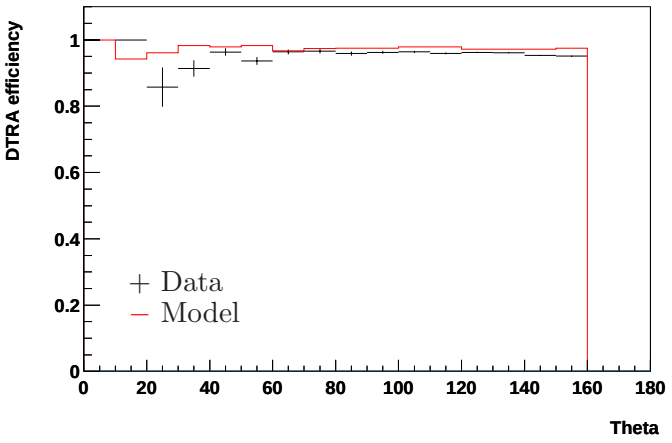

Figure 6.8: Vertex fitted track efficiency plotted as a function of θ.

A small drop in efficiency at low values of θ_e can be seen in figure 6.8. At these low angles the electron passes through the end-wall of the CJC and into the FTD. The large amount of inactive material can result in the electron showering, distorting the track angle measurement. Therefore for $\theta_e < 35°$ the DCA cut is not applied. This increases the efficiency for events at very high Q^2.

6.6 Background Suppression

The types of background that can contribute to the NC event sample fall into two categories, non-ep and ep backgrounds. Non-ep backgrounds occur for example when a cosmic or beam-halo muon is misidentified as a final state electron. Photoproduction, $\gamma\gamma$, low Q^2 DIS, QED-Comptons and W and Z^0 boson production are all ep backgrounds. Further discussion on the different sources of background can be found in chapter 4.

Non-ep backgrounds are heavily reduced by the vertex and track-cluster linking requirements. These events can also be eliminated by requiring the CJC timing information to be consistent with an ep event. Events that do not occur within ± 20 ns of a bunch crossing are rejected. The inefficiency of this cut can be studied using the "clean NC sample", defined in section 6.5, and amounts to 0.26 ± 0.02 %. Finally, this background can be reduced to negligible levels [72] by the application of dedicated background finders [77]. The background finders are only applied if the event does not have a vertex fitted track matched to the electron, if there is a significant imbalance in the event's transverse momentum ($p_{T,h}/p_{T,e} < 0.5$ or > 2), or for small values of $\eta_{max} < 3$, where η_{max} is the maximum value of pseudo-rapidity of any cluster with an energy > 400 MeV. The η_{max} cut is close to the limit of the LAr acceptance, $\eta_{max} \simeq 3.4$, for NC DIS events. The inefficiency of the background finder rejection, used within the limits defined, is not significant.

Photoproduction and low Q^2 DIS background, where the electron escapes the confines of the detector and a hadron is misidentified as the electron, are generally only found at high values of y and low values of E'_e. Therefore the energy cut imposed as described in the context of the trigger efficiency studies already reduces this background and is complemented by a cut on $y < 0.9$. The track-cluster link requirement also significantly reduces this background. Additionally, a cut on the total $E - P_z$ can be used to reduce these backgrounds, using our knowledge of the detector kinematics. A perfectly measured NC event will have a total $E - P_z$ value of 55 GeV, twice the electron beam energy. Photoproduction and low Q^2 DIS however, due to the escaping final state electron, will typically have a much lower value of $E - P_z$. Therefore, a further requirement that $E - P_z > 35$ GeV is placed on all events.

Any remaining photoproduction background is removed by identifying events with electron candidates that have a track with opposite charge to that of the incident electron. It is assumed that the number of hadrons faking an electron which have a negative charge is equal to the number that fake an electron with positive charge. Therefore, the total number of photoproduction events in the sample is taken to be twice the number of opposite-sign charge events and the background is subtracted from the number of events that pass the cuts on a bin by bin basis. At scattered electron energies greater than 18 GeV, this technique becomes rather inefficient due to the difficulty of measuring the charge on high p_T tracks. However, the photoproduction contribution at these energies is known to be negligible, for example from studies with the PYTHIA photoproduction simulation. This technique is therefore only used for $E'_e < 18$ GeV and the systematic uncertainty is estimated to be that due to the largest subtracted value in any affected

bin.

QED-Compton events and $\gamma\gamma$ background events are rejected by looking for their distinctive final state of two electromagnetic clusters with no hadronic deposits and only one or two tracks. DIS events typically have a large energy deposit in the hadronic section of the calorimeters. Thus events where the hadronic part of the calorimeter contributes a small fraction of the total energy $E_{had}/E_{tot} < 10\%$ are considered to be background if there are less than three tracks in the event. In the case of events with low values of E_{had}/E_{tot}, the fraction of background events can be further reduced by rejecting events with $\eta_{max} < 3$, which is a typical signature of both QED-Comptons and $\gamma\gamma$.

The decay lepton in W and Z^0 production events can be misidentified as the scattered electron and these are therefore considered as possible sources of background. The contribution of boson production is found to be very small using the simulation and may be neglected.

The final selection cuts used to obtain the high Q^2 NC event sample are summarised in table 6.3.

Selection Description	*Requirements*	*In Section*
A good electron candidate in the LAr	See section	6.2
Run Selection	See section	6.3
High Q^2 NC triggers	ST67 || ST71 || ST75 || ST77	6.4
Electron Energy cut	$y_e < 0.63$ || $Q^2 < 890\text{GeV}^2$	6.4
Vertex Type	Require either Central or Forward	6.5
Position of vertex in z	-34$< z <$36 cm	6.5
Track pointing to the electron cluster	DCA$<$ 12 cm for DTRA tracks and DTNV tracks within 5 cm of vertex (not required in the region $\theta < 30^\circ$	6.5
Electron not in a LAr crack	Cut cracks in z between LAr wheels and cut 2° either side of octant edge	6.2
CJC timing consistent with ep event	≤ 20 ns of bunch crossing	6.6
Cut on y	$y_e < 0.9$	6.6
Cut on $E - P_z$	$E - P_z > 35$ GeV	6.6
Applied Background Finders	See Section	6.6
Not a QED-Compton or $\gamma\gamma$ event	See Section	6.6

Table 6.3: A list of the cuts used to select the high Q^2 NC DIS event sample. The selection criteria fails to remove ~ 3000 background events, the majority of which are low Q^2 DIS events and photoproduction.

6.7 Alignment and Calibration of Electron variables

In this analysis the polar angle of the scattered electron (θ_e) is determined using the position of its energy deposit (cluster) in the LAr, together with the interaction vertex

reconstructed with tracks from charged particles in the event. The relative alignment of the calorimeter and tracking chambers is determined using a sample of events with a well measured electron track, using information from the CJC and z drift chambers. Minimisation of the spatial discrepancy between the electron cluster and the extrapolated track allows the LAr and inner tracking chambers to be aligned. The residual discrepancy then determines the systematic uncertainty on the θ_e measurement, enumerated in section 7.4.

The calibration of the electromagnetic part of the LAr is performed using the method described in [60]. Briefly, the redundancy of the detector information allows a prediction of the scattered electron energy (E'_e) to be made using the DA method (defined in section 5.3). This prediction is then compared with the measured electromagnetic energy, allowing local calibration factors to be determined in a finely segmented grid in z and ϕ. The calibration procedure is also performed on the simulated data. The final calibration is obtained by application of a further small correction determined from the simulation, which accounts for small biases in the reconstruction of the γ_h. The calibration is cross checked using independent data samples from QED-Compton scattering and two-photon e^+e^- pair production processes. The resulting systematic error is described in section 7.4.

6.8 Calibration of Hadronic variables

The hadronic final state is measured using energy deposits in the LAr and SPACAL supplemented by low momentum tracks. Isolated low energy calometric deposits are classified as noise and excluded from the analysis. The detector response to hadrons is calibrated by requiring transverse momentum conservation between the precisely calibrated scattered electron and the hadronic final state in NC events, as described in [60]. The electron transverse momentum is determined from

$$p_{T,e} = \sqrt{p_{x,e}^2 + p_{y,e}^2}, \tag{6.5}$$

while the hadronic transverse momentum is defined in equation 5.2.

Extensive studies and cross checks of the hadronic response of the calorimeter have led to an improved understanding of the hadronic energy measurement [22]. The calibration procedure is cross checked by requiring conservation of the total $E-P_z$, with the reference scale taken from the double angle method, rather than the scattered electron. These studies have allowed the systematic uncertainty on the hadronic scale to be reduced with respect to previous measurements [60, 23]. The systematic uncertainty on the hadronic variables is described in section 7.4.

6.9 The Full NC Event Selection

After applying the full NC selection a total of 178604 events are obtained. The correct functioning of the analysis cuts and the simulation is demonstrated through the use of

control distributions, which test the level at which the high Q^2 NC sample is understood.

Figure 6.9 shows the electron energy, θ and ϕ distributions for the selected data events and simulation. There is good agreement between the simulation (red line) and the data (points). The electron energy plot begins at 11 GeV, in accordance with the cut imposed and peaks at 27.5 GeV, the incident electron beam energy. There are far less events at energies higher than the peak, corresponding to the statistically limited very high Q^2 region. The θ distribution shows a peak at high values, where the electron is scattered through the smallest angles. The cut at 160° is due to the cut on the impact position of the electron, outlined in section 6.2. The low statistics at low values of θ correspond to the minority of events where the electron scatters backwards, which are very high Q^2 events. This distribution is well modelled by the simulation. The ϕ distribution is essentially flat, which is to be expected, but there is some structure because of the cuts on the detector cracks and the regions cut to account for low trigger efficiency (the fiducial volume cuts). The ϕ structure is well modelled by the simulation.

The z position of the ep interaction vertex, or z-vertex, has already been discussed in section 6.5 and was shown to be well modelled after a reweighting of the Monte Carlo. The impact position of the electron on the LAr surface, measured along the z-axis, is also well described by the simulation. The z-crack at $15 < z < 25$cm and the edge of the BBE at -120 cm can be clearly seen in figure 6.10.

Figure 6.11 shows the y_Σ, $E - P_z$ and $\log Q^2$ distributions. The y distribution peaks at low values of y (corresponding to high values of θ) and the effect of the replacement electron energy cut is noticeable and well described by the simulation. The $E - P_z$ distribution peaks at twice the incident electron energy (55 GeV), as described in section 6.6. The $\log Q^2$ distribution peaks at low values of Q^2 and drops off at higher values, in accordance with the cross section dependence on the propagator, described in chapter 2.

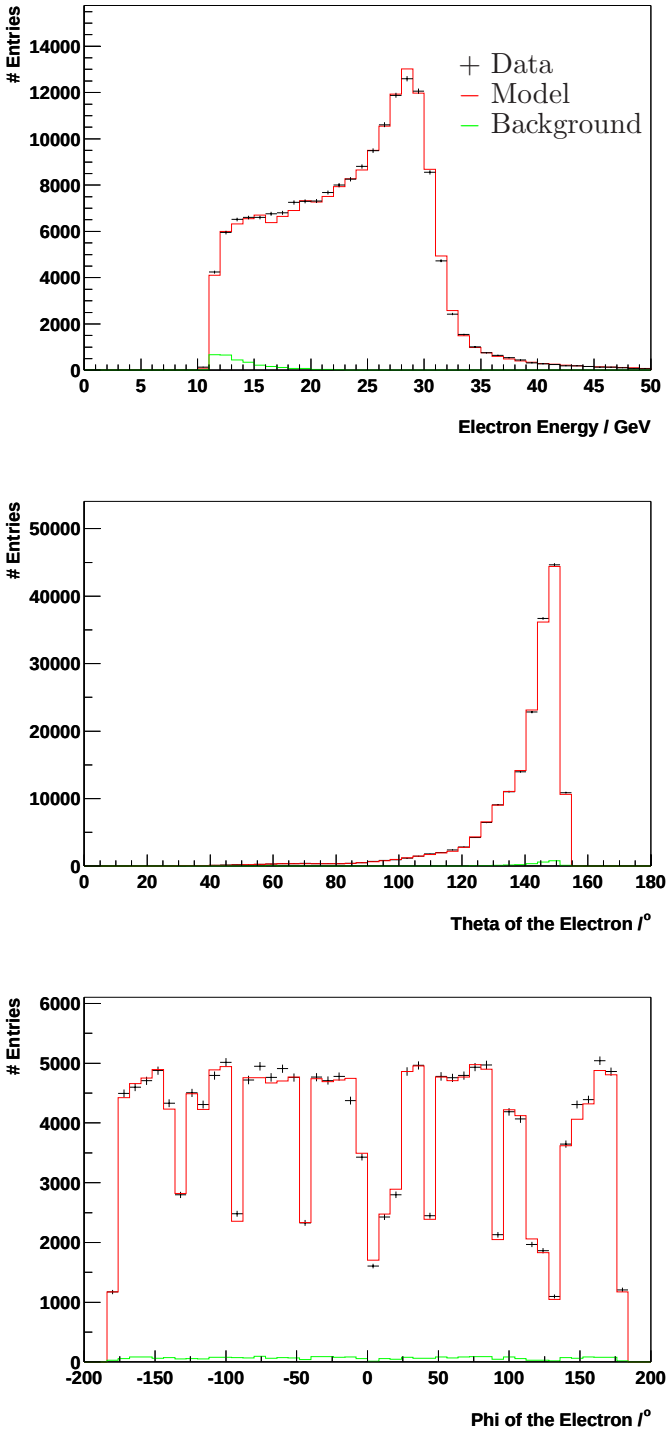

Figure 6.9: From top to bottom: Plots of the energy, polar and azimuthal angle of the scattered electron. The data are shown as points, the sum of the background Monte Carlos is shown as a green line and the sum of the model and background Monte Carlos is shown as a red line.

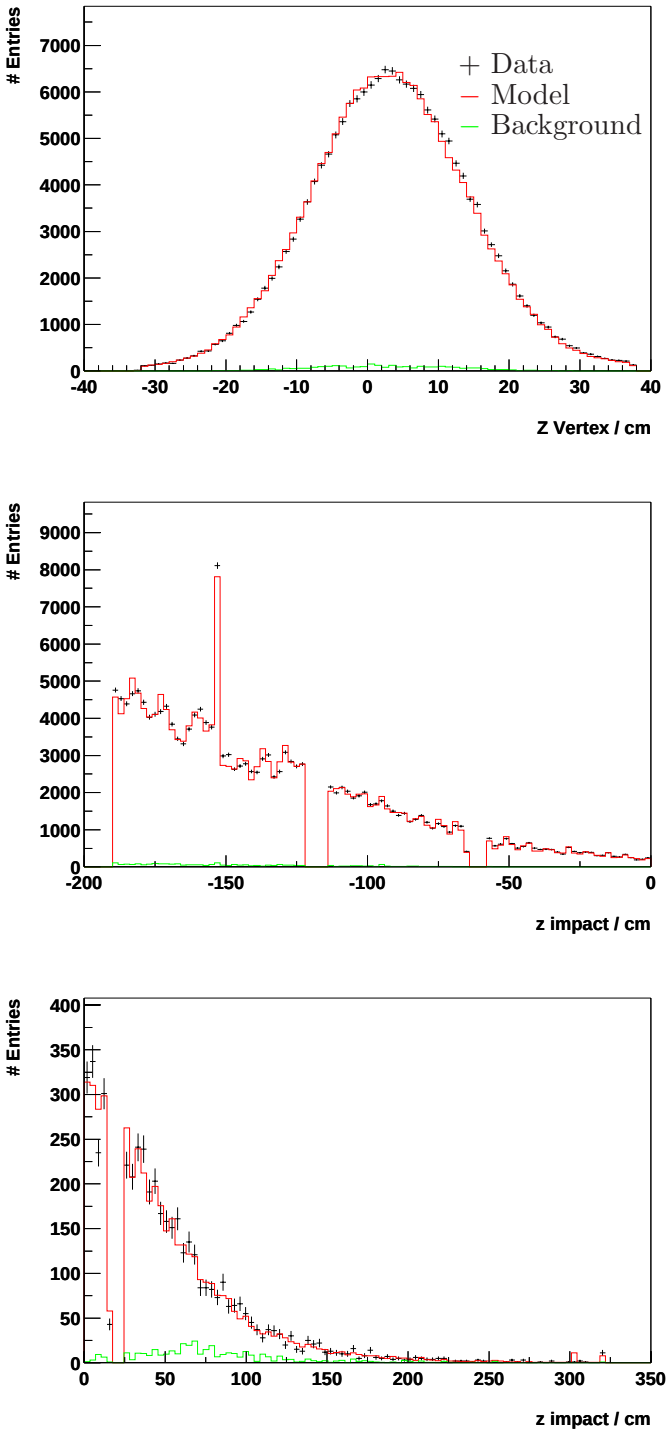

Figure 6.10: From top to bottom: Plots of the z-vertex of the event, the point in z of impact of the electron on the LAr surface for negative values of z and then for positive values of z. The data are shown as points, the sum of the background Monte Carlos is shown as a green line and the sum of the model and background Monte Carlos is shown as a red line.

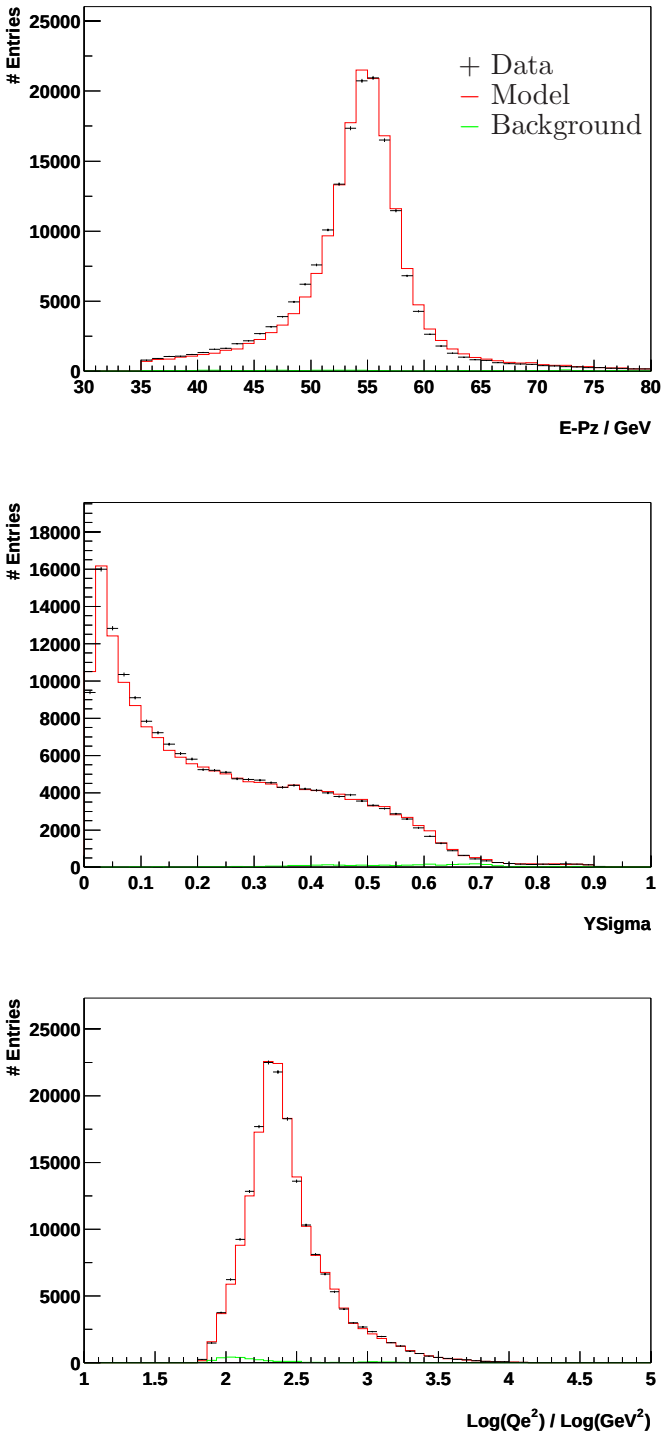

Figure 6.11: From top to bottom: Plots of the total $E - P_z$, the kinematic variable y, calculated using the $e\Sigma$ method and the $\log_{10} Q^2$ of the event. The data are shown as points, the sum of the background Monte Carlos is shown as a green line and the sum of the model and background Monte Carlos is shown as a red line.

Chapter 7

NC Cross Section Measurement

In this chapter the method used to determine the NC cross section is described. The kinematic plane is divided into bins in Q^2 and x and the number of events found in each bin are then converted into a cross section. The bin selection is presented first, followed by a description of purity, stability and acceptance, their significance and the requirements placed upon them in this measurement. This is followed by a section on the method of obtaining a cross section from numbers of events which includes a description of the radiative and bin centre corrections. The chapter ends with a section on the errors caused by systematic uncertainties in the measuring process.

7.1 Bin Selection

The cross section measurement is performed in this analysis in bins of x and Q^2. There are 24 bins in Q^2 and 14 bins in x, evenly distributed per decade. The bin boundaries are:

bin boundaries in $\log_{10}(Q^2/\mathrm{GeV}^2)$:
1.65, 1.75, 1.85, 1.95, 2.05, 2.15, 2.25, 2.35, 2.45, 2.55, 2.65, 2.75, 2.85, 2.95, 3.05, 3.15, 3.25, 3.35, 3.55, 3.7782, 4.000, 4.2222, 4.4437, 4.6659, 4.8881

bin boundaries in $\log_{10}(x)$:
-2.8, -2.6, -2.4, -2.2, -2.0, -1.8, -1.6, -1.4, -1.2, -1.0, -0.8386, -0.68, -0.5, -0.3, 0.00

The bin boundaries used are the same as those used in previous analyses on 94-97 and 99-00 e^+p data, to better compare the results of the analysis.

Additionally, in order to obtain sufficient statistics at high Q^2, there is a wider Q^2 binning scheme, called the integrated binning scheme, which is used to measure and extract a value of $x\tilde{F}_3$ (see sections 2.5.3 and 8.4). This binning scheme is only applied at high Q^2, with the bin boundaries defined as:

bin boundaries in $\log_{10}(Q^2/\mathrm{GeV}^2)$:
3.05, 3.35, 4.0, 4.8881

7.2 Purity, Stability and Acceptance

In order to extract a reliable measurement from the data, it is important to take into account detector effects, such as the detector resolution, efficiencies and geometric acceptances. This is done by comparing MC Model events, generated using DJANGO in the case of this analysis, before and after they pass through the detector simulation. The events selected before the simulation are the Generated (Gen) level events, those after the simulation are the Reconstructed (Rec) level events.

If the data are well described by the reconstructed level event properties, it is possible to use the difference between the reconstructed and generated samples to correct the data for the detector effects. If the simulation fails to correctly describe the data, which could be due to anything from poor calibration of the electron energy (see section 6.7) to incorrect modelling of a part of the detector, then the simulation can be corrected accordingly. In the case where the data-simulation discrepancy cannot be accounted for the simulation is left unchanged and the data discrepancy is considered possible new physics. The remaining data-MC discrepancy is accounted for in the systematic errors.

Detector effects are studied by looking at the relationship between generated and reconstructed level events. Cuts are imposed at both generated and reconstructed levels. There are 4 possible outcomes possible for MC events in a given bin (see figure 7.1) defined by four variables which are statistically independent:

- N_{STAY}: The number of events that have the same bin number(i) at both the reconstructed and generated level.
- N_{LOST}: The number of events with a generated bin(i) that are not reconstructed due to inefficiencies or that are reconstructed outside the phase space considered in this analysis.
- $N_{SMEAR.IN}$: The number of events that enter into a reconstructed bin (i) but that are generated outside the bin.
- $N_{SMEAR.OUT}$: The number of events that generated in a bin (i) but are reconstructed elsewhere.

The total number of reconstructed and generated events in a bin, N_{Rec} and N_{Gen} respectively, are then given by:

- $N_{Rec} = N_{STAY} + N_{SMEAR.IN}$

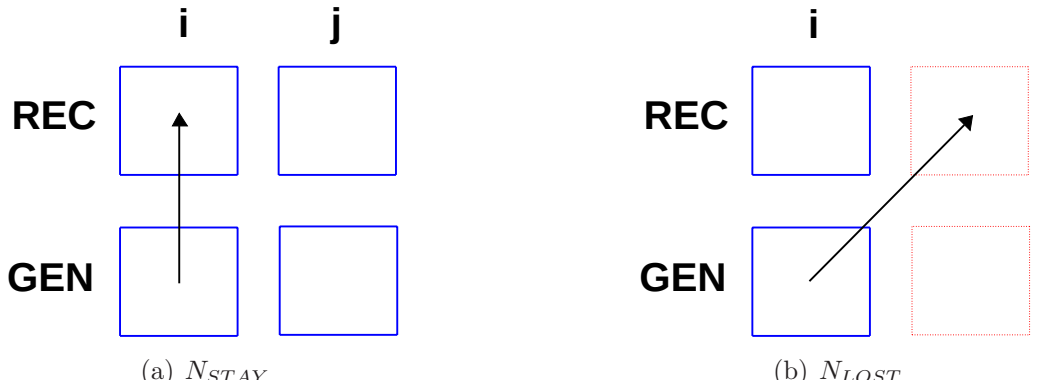

(a) N_{STAY}

(b) N_{LOST}

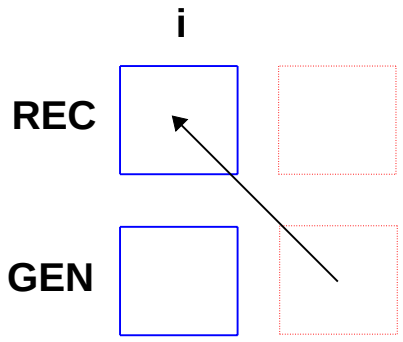

(c) $N_{SMEAR.IN}$

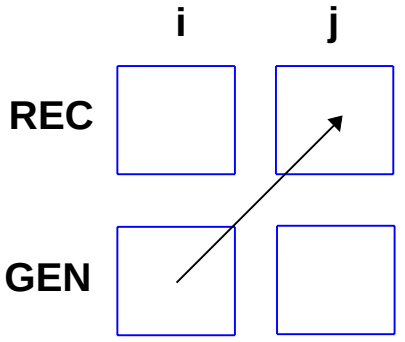

(d) $N_{SMEAR.OUT}$

Figure 7.1: An illustration of possible bin migrations is shown above, the arrows show the path of migration of an event starting at the generated level and pointing to the position it is in at the reconstructed level. The thick blue squares are bins inside the measured phase space, and the thin red lined squares depict bins outside the binning scheme of this analysis. (a) depicts the situation where the bin number (i) of an event is not changed by the detector simulation. (b) shows a generated level event being lost from the reconstructed sample as it is reconstructed outside of the phase space measured in the analysis. (c) is an example of an event that does not fall into the analysis binning scheme at the generated level but is reconstructed in the phase-space measured in this analysis. Finally, (d) is an example of an event that changes bin number during the detector simulation.

- $N_{Gen} = N_{STAY} + N_{SMEAR.OUT} + N_{LOST}$

These definitions can be used to define the variables purity, $\mathcal{P}$, stability, $\mathcal{S}$, and acceptance, $\mathcal{A}$, which are defined by the relationship between generated and reconstructed binned events and quantify the effects of detector resolution and efficiency:

$$\mathcal{A} = \frac{N_{Rec}}{N_{Gen}} \tag{7.1}$$

$$\mathcal{P} = \frac{N_{STAY}}{N_{Rec}} \tag{7.2}$$

$$\mathcal{S} = \frac{N_{STAY}}{N_{Gen} - N_{LOST}}. \tag{7.3}$$

The acceptance of a bin quantifies the overall correction which must be made for detector effects. The true number, N_{True} of events after correcting the data for detector effects is recovered by applying the acceptance correction:

$$N_{True} = N_{Data} \times \frac{N_{Gen}}{N_{Rec}} = \frac{N_{Data}}{\mathcal{A}}. \tag{7.4}$$

The effects of smearing are quantified by the purity and stability of the bin. Purity quantifies the fraction of reconstructed events that have the same bin at the generated level. The stability quantifies the fraction of generated events which do not change bin after the detector simulation. Stability does not take into account events that are lost to smearing outside of the binning scheme.

The acceptance, purity and stability are required to be greater than 30% in order to ensure that contents of the bin are well correlated with the generated values. Sample plots of the purity, stability and acceptance are shown in figure 7.2.

7.3 Cross Section Extraction

The cross section for a single x-Q^2 bin is given by the formula

$$\frac{d^2\tilde{\sigma}}{dxdQ^2} = \frac{N_{Data} - N_{BG}}{\mathcal{L} \cdot \mathcal{A}} \cdot \delta^{bc} \cdot \delta^{rc} \tag{7.5}$$

where N_{Data} is the number of data events found in the bin, N_{BG} is the luminosity normalised number of background MC events found in the bin, $\mathcal{L}$ is the Data Luminosity, δ^{bc} is a bin centre correction term, and δ^{rc} is a correction term for radiative effects.

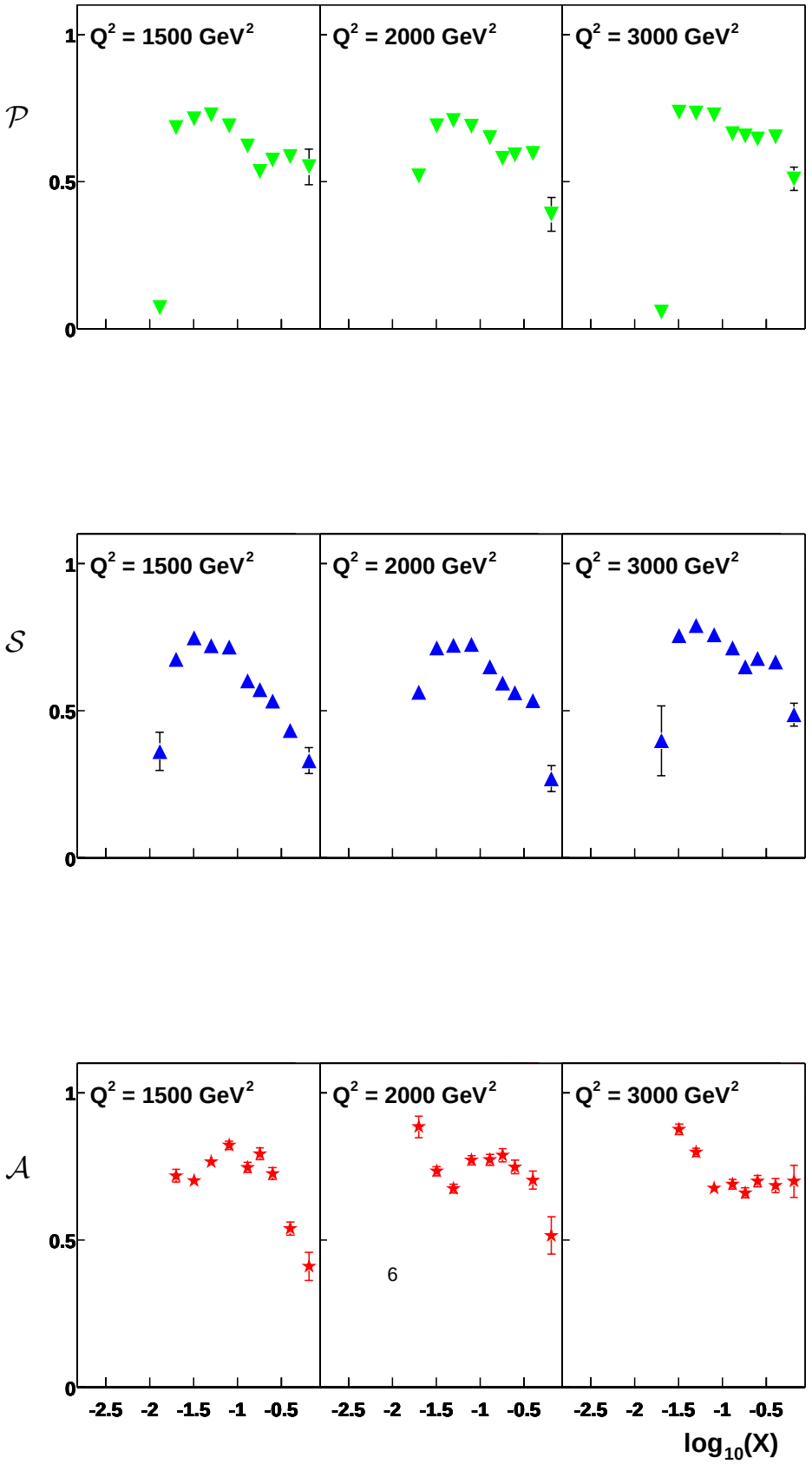

Figure 7.2: Plots of the purity (top), stability (middle) and acceptance (bottom), plotted as a function of x, in bins of Q^2.

The bin centre correction transforms the bin-integrated cross section measurement to a differential cross section measurement made at a single point in x and Q^2. The bin centre correction is defined as

$$\delta^{bc} = \frac{d^2\tilde{\sigma}^N_{Gen}}{dxdQ^2} \cdot \frac{1}{\langle\tilde{\sigma}^N_{Gen}\rangle}, \tag{7.6}$$

where $\langle\tilde{\sigma}^N_{Gen}\rangle$ is the bin-integrated Model cross section without radiative corrections and $\frac{d^2\tilde{\sigma}^N_{Gen}}{dxdQ^2}$ is the double differential Model cross section without radiative corrections, measured at the bin centre. The subscript "Gen" indicates that these are model predictions at the generated level.

The radiative correction accounts for the fact that QED radiation can change the measured kinematics from those that actually underly the event. The radiative correction is defined as

$$\delta^{rc} = \frac{\langle\tilde{\sigma}^N_{Gen}\rangle}{\langle\tilde{\sigma}^R_{Gen}\rangle}, \tag{7.7}$$

where $\langle\tilde{\sigma}^R_{Gen}\rangle$ is the bin-integrated Model cross section taking into account the radiative corrections. The radiative corrections are well understood, as they rely on our knowledge of QED.

It is possible to simplify equation 7.5 by substituting in the definitions of δ^{bc}, δ^{rc} and the definition of the acceptance, equation 7.1, while remembering that the acceptance is calculated from a Model that takes into account radiative corrections ($\mathcal{A} = N^R_{Rec}/N^R_{Gen}$) and that the Monte Carlo Model has been normalised to the data luminosity:

$$\begin{aligned}
\frac{d^2\sigma_{Data}}{dxdQ^2} &= \frac{N_{Data} - N_{BG}}{\mathcal{L}\cdot\mathcal{A}} \cdot \delta^{bc} \cdot \delta^{rc} \\
&= \frac{N_{Data} - N_{BG}}{\mathcal{L}\cdot\mathcal{A}} \cdot \frac{1}{\langle\tilde{\sigma}^N_{Gen}\rangle} \cdot \frac{d^2\tilde{\sigma}^N_{Gen}}{dxdQ^2} \cdot \frac{\langle\tilde{\sigma}^N_{Gen}\rangle}{\langle\tilde{\sigma}^R_{Gen}\rangle} \\
&= \frac{(N_{Data} - N_{BG})\cdot N^R_{Gen}}{\mathcal{L}\cdot N^R_{Rec}} \cdot \frac{d^2\tilde{\sigma}^N_{Gen}}{dxdQ^2} \cdot \frac{1}{\langle\tilde{\sigma}^R_{Gen}\rangle} \\
&= \frac{(N_{Data} - N_{BG})\cdot\langle\tilde{\sigma}^R_{Gen}\rangle}{N^R_{Rec}} \cdot \frac{d^2\tilde{\sigma}^N_{Gen}}{dxdQ^2} \cdot \frac{1}{\langle\tilde{\sigma}^R_{Gen}\rangle} \\
&= \frac{N_{Data} - N_{BG}}{N^R_{Rec}} \cdot \frac{d^2\tilde{\sigma}^N_{Gen}}{dxdQ^2}
\end{aligned} \tag{7.8}$$

Using equation 7.8 the differential cross section measurement can be performed in a single step by adjusting a generator level theoretical prediction ($d^2\tilde{\sigma}^N_{Gen}/dxdQ^2$) according to the deviation of the uncorrected data ($N_{Data} - N_{BG}$) from the reconstructed level theoretical prediction including radiative effects (N^R_{Rec}).

7.4 Systematic Uncertainties

While it is possible to reduce the statistical error of a measurement by taking a larger data-sample, it is impossible to completely remove the measurement's susceptibility to systematic uncertainties. All the sources of systematic uncertainties lead to a corresponding error on the final measurement. Systematic errors fall into two categories, those which are correlated between all bins and those which are uncorrelated from bin to bin. The correlated errors are found to be symmetric to good approximation and are assumed to be so in the following discussion.

Many systematic errors are treated as partially correlated and partially uncorrelated, with the total systematic error formed by adding the individual correlated and uncorrelated errors in quadrature. The systematic errors are discussed briefly below (see [22, 39, 72, 75, 78, 79] for more details).

- There is a global 1.5% uncertainty on the luminosity measurement [22, 72].
- There is an uncertainty on the electron energy scale that is dependent on the position of z impact. For the backward region, $z < -150$cm, the uncertainty is 1%. It drops to 0.7% for $-150 < z < 20$cm, rises to 1.5% for $20 < z < 100$cm and finally increases to 3% in the forward region $z > 100$cm. The correlated part of this uncertainty is mainly due to the possible bias of the calibration method, and is estimated at 0.5% throughout the LAr. It results in a correlated systematic error which is typically below 1%, but increases to $\sim 3\%$ at low y and $Q^2 \lesssim 1,000$GeV, and $\sim 8\%$ for larger Q^2 [22, 75].
- The correlated uncertainty on the electron polar angle, θ_e, is 1 mrad in the region $\theta_e > 135°$. It rises to 2 mrad in the region $120 < \theta_e < 135°$ and then 3 mrad for $\theta_e < 120°$. This results in a typical uncertainty of less than 1%, increasing to $\sim 5\%$ at high x [22, 75].
- The electron identification efficiency results in a 0.5% uncorrelated error for the region $z < -5$cm. This inefficiency rises to 2% for higher values of z, because the precision of the efficiency is estimated using an independent track-based electron identification algorithm, which is statistically limited for $z > -5$cm [22, 75].
- The inefficiency of the scattered electron track-cluster link requirement results in a 0.5% uncorrelated error [22, 75].
- There is a 1% correlated error on the hadronic energy measurement in the LAr, due to the uncertainty in the reference scale and the calibration method. There is also an uncorrelated 1% uncertainty in the region $12 < P_{T,h} < 50$ GeV and $\gamma_h > 15°$ and a 1.7% uncertainty outside that region. The errors add in quadrature, and result in a total uncertainty of 1.4% and 2% for the respective regions [22, 75].
- There is a 5% uncertainty on the hadronic scale of the SPACAL. The uncertainty on the hadronic energy measurement due to the inclusion of low momentum tracks

can be calculated by shifting their contribution by 3%. The resulting systematic error is small compared to that from the uncertainty of the LAr energy scale. The LAr, SPACAL and track contributions are combined, yielding a single, correlated, error on the hadronic energy scale which is typically $\lesssim 1\%$ but rises to $\sim 5\%$ at low y [22, 75].

- There is a 25% uncertainty assigned to the amount of energy recorded in the LAr which is due to noise. This gives rise to a large correlated error at low y, reaching $\simeq 10\%$ at $x = 0.65$ and $Q^2 \lesssim 2,000\text{GeV}^2$ [22, 72].

- A 30% correlated systematic uncertainty on the subtracted photoproduction background is determined by comparing the photoproduction simulation with data for a region of phase space that is dominated by photoproduction. The resulting systematic error is typically $\lesssim 1\%$ [22, 72].

- There is a 0.3% uncorrelated error due to the trigger efficiencies [22].

The total systematic error typically amounts to about 3% [22].

Chapter 8

Neutral Current Cross Section Measurement and Extraction of $x\tilde{F}_3$

8.1 Introduction

In this chapter the results of the reduced NC cross section measurement are presented and compared to model predictions and recent H1 published data. The results are obtained from an analysis of 99-00 e^+p data, which amounts to a luminosity of $\mathcal{L}$=65.2 pb^{-1}. The single differential cross sections are presented first, both as a function of x and Q^2. The double differential reduced cross section is then presented as a function of x at fixed values of Q^2. Finally, a new method of determining $x\tilde{F}_3$ is presented and the extraction results are compared with previously published data and the H1 PDF 2000 fit results (described in section 2.6).

8.2 The x and Q^2 dependence of the cross section

The reduced NC cross section as a function of Q^2, calculated in the range $y < 0.9$, is shown in figure 8.1. Over three orders of magnitude in Q^2 the reduced cross section falls by seven orders of magnitude. This effect is due to the γ propagator, discussed in chapter 2. The decrease with Q^2 is steeper at higher values of Q^2. In this region the neutral current interaction occurs via Z^0 boson exchange and the magnitude of the neutral current cross section is of the same order as that of the charged current cross section, as shown in figure 2.2. This behaviour is well modelled by the H1 PDF 2000 fit (full line). The statistical error is typically 1-2%, but increasing to 40% at the highest values of Q^2. At low Q^2 the calculated systematic errors are approximately equivalent to the statistical errors, with the total error ranging from 2 to 4%.

The reduced NC cross section as a function of x, calculated in the $Q^2 > 60$ GeV^2 range, is shown in figure 8.2. The cross section is well described by the NLO QCD prediction (full

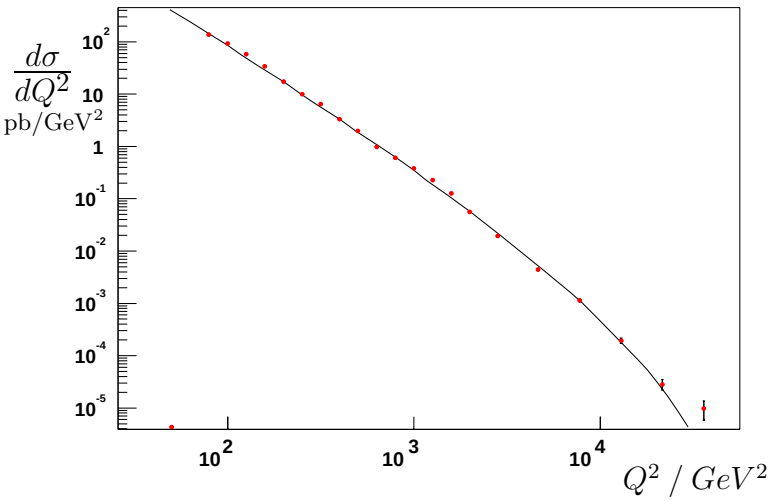

Figure 8.1: The single differential cross section as a function of Q^2. The points are measured using 99-00 e^+p data, with the error bars delimiting the statistical uncertainty (inner) and total uncertainty (outer) including the systematic errors added in quadrature. The solid line is the theoretical prediction of the H1 PDF 2000 fit.

line). It is seen to fall with increasing x, reflecting the behaviour of the quark densities. Typically the statistical uncertainties are about 1-3%, increasing at high x, with the total error ranging from 2 to 4%.

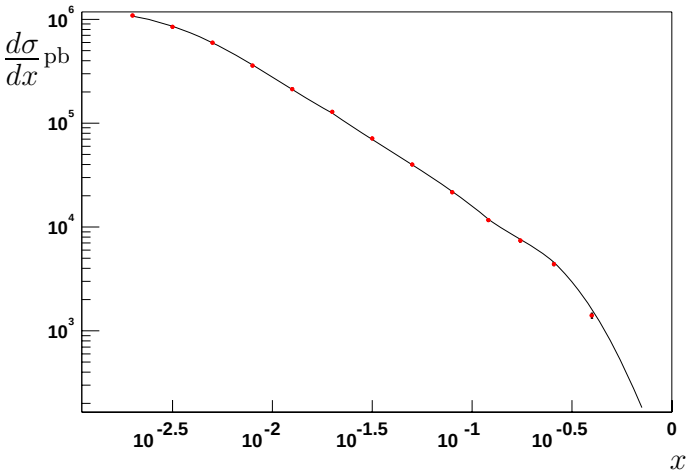

Figure 8.2: The single differential cross section as a function of Bjorken-x. The points are measured using 99-00 e^+p data, with the error bars delimiting the statistical uncertainty (inner) and total uncertainty (outer) including the systematic errors. The solid line is the theoretical prediction of the H1 PDF 2000 fit.

8.3 The double differential Neutral Current cross section

Figures 8.3, 8.4 and 8.5 show the double differential reduced cross section, plotted as a function of x, in bins of Q^2. The reduced cross section is measured over three orders of magnitude in x and three orders of magnitude in Q^2. The results are also tabulated in Appendix A. In total the measurement comprises 156 measured points, which are shown in figures 8.3-8.5. The statistical error on the measurement is typically 2-3% at low Q^2, with the total error being typically 1% higher. The uncertainty increases significantly for higher Q^2 where the precision is statistically limited and the statistical contribution to the errors reach ∼10%. The plot also shows the NLO QCD fit (the solid line) and the results obtained in the latest published measurement [22] (the blue points). The data are well described by the fit, and also agree with the published data.

In all Q^2 bins, the data exhibit a strong rise with decreasing x. Because of the dominant cross section contribution of $\tilde{F}_2$, which is sensitive to the sea quark distribution (see section 2.3.2), this behaviour can be understood as being due to the increase of the sea quark distribution at low x. The slight damping of this rise at the lowest values of x (highest y) indicates a contribution of the longitudinal structure function, $\tilde{F}_L$.

The double differential reduced cross section measurement has larger systematic uncertainties than the single differential measurement. This is partly due to the purity, stability and acceptance being lower, such that events in the double differential binning can migrate in two dimensions (four directions) and not one (two directions), as was the case in single differential binning. The larger migrations lead to larger uncertainties in the acceptance corrections.

The neutral current double differential cross section measurement shows the strong level of agreement between the FORTRAN and OO analyses for the first time. The OO measurement results give us confidence that the analysis package can be used to accurately analyse future HERA II data. With the level of agreement attained, it is also possible to use the OO double differential reduced cross section, measured in the integrated Q^2 bins, to extract a value of $x\tilde{F}_3$ from the data.

8.4 The $x\tilde{F}_3$ Extraction

Using similar ideas to those used to extract $\tilde{F}_L$ (see section 2.5.4), it is also possible to extract a value for $x\tilde{F}_3$ using only the 99-00 high Q^2 e^+p NC cross section, measured in section 8.3. In the region of phase space measured the contribution of $\tilde{F}_L$ is small and may be neglected. Neglecting $\tilde{F}_L$, equation 2.8 can be re-arranged to give us the formula to extract $x\tilde{F}_3$ from positron data only

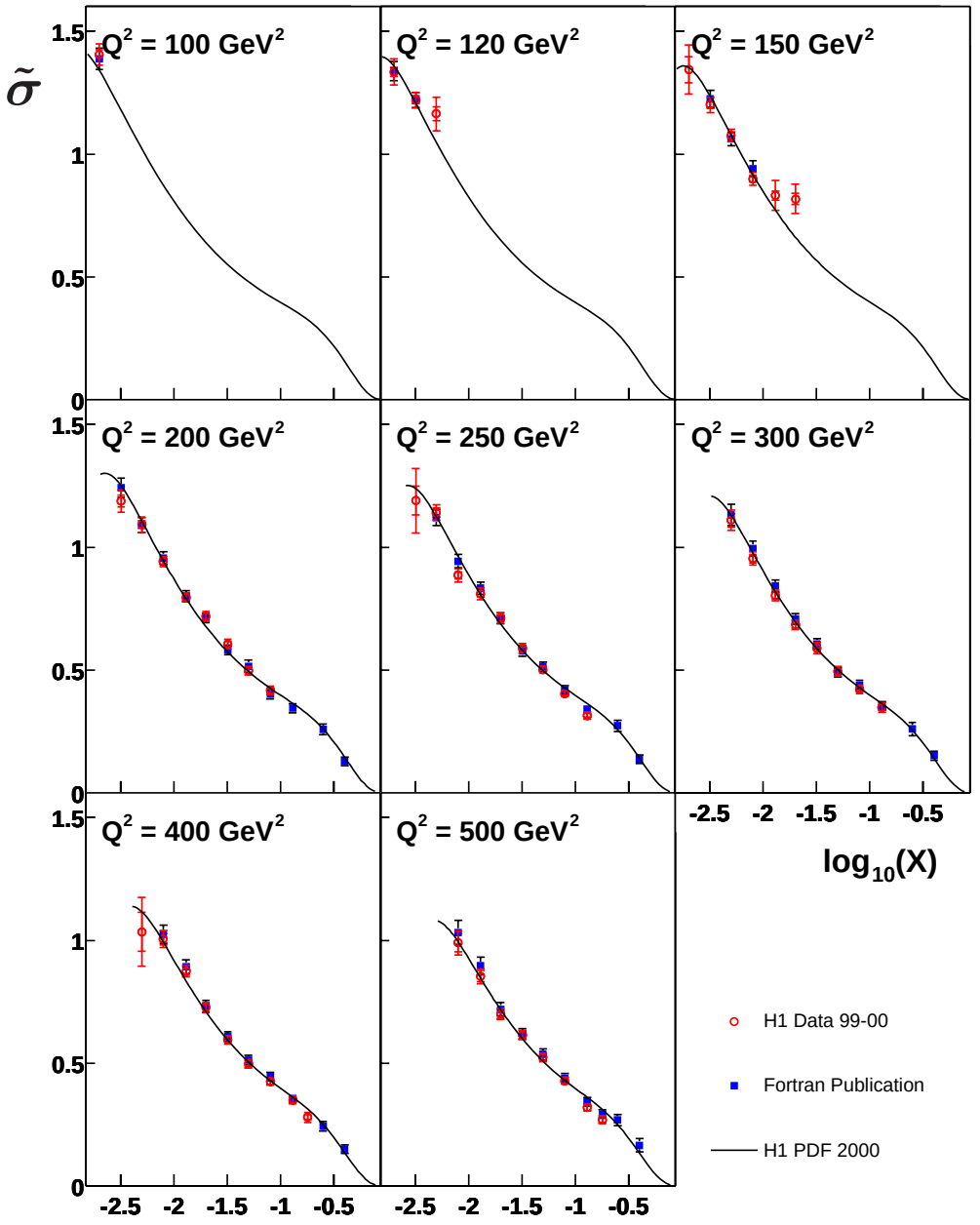

Figure 8.3: The reduced cross section, plotted against x in bins of Q^2. The red points are the results of the object orientated analysis using 99-00 e^+p data, with the error bars delimiting the statistical uncertainty (inner) and total uncertainty (outer) including the systematic errors. The blue points are the results from the latest H1 paper, with the error bars showing the total error. The solid line is the theoretical prediction of the H1 PDF 2000 fit. The bins shown in this figure range from $Q^2 = 100$ GeV^2 to $Q^2 = 500$ GeV^2

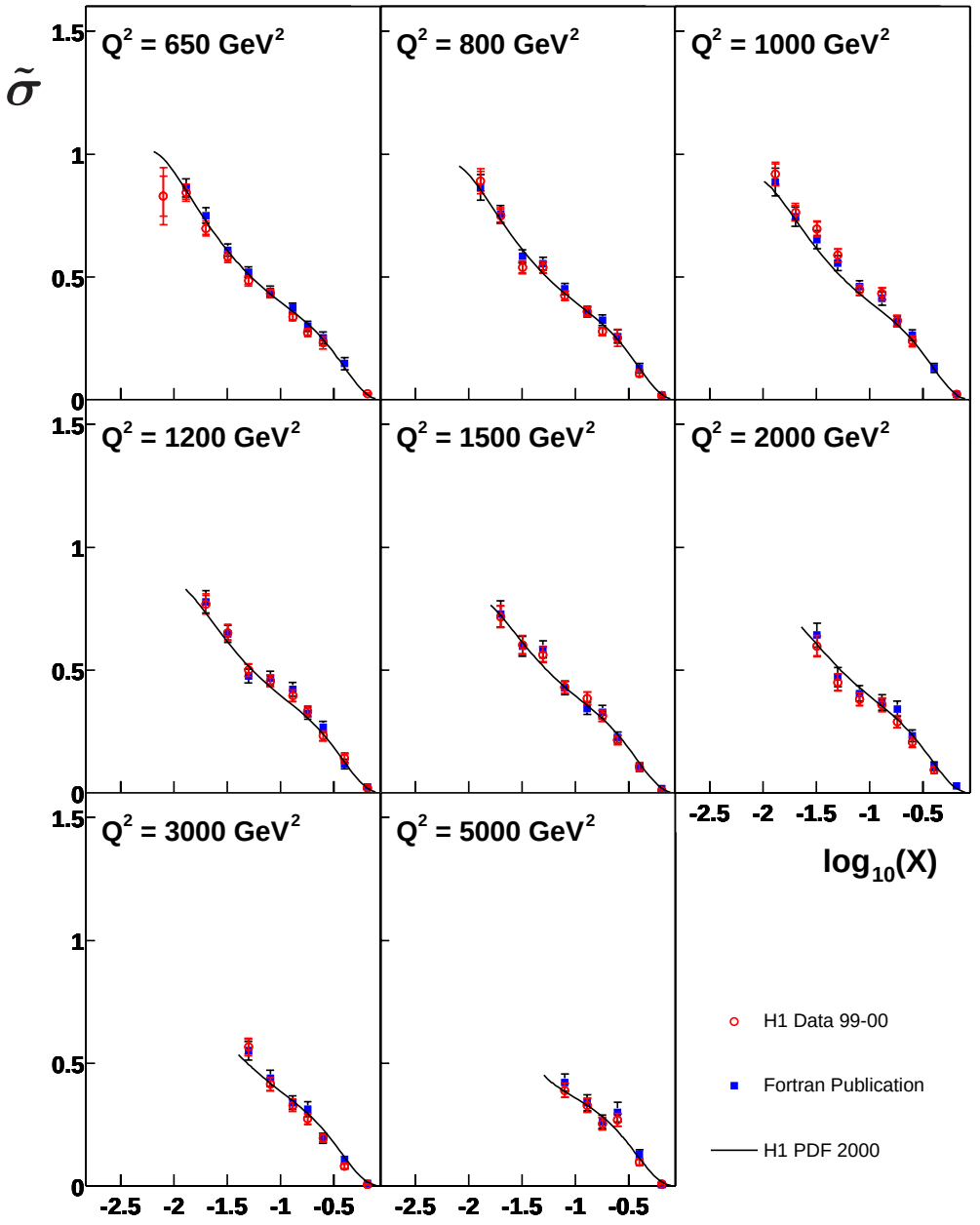

Figure 8.4: The reduced cross section, plotted against x in bins of Q^2. The red points are the results of the object orientated analysis using 99-00 e^+p data, with the error bars delimiting the statistical uncertainty (inner) and total uncertainty (outer) including the systematic errors. The blue points are the results from the latest H1 paper, with the error bars showing the total error. The solid line is the theoretical prediction of the H1 PDF 2000 fit. The bins shown in this figure range from $Q^2 = 650$ GeV^2 to $Q^2 = 5000$ GeV^2

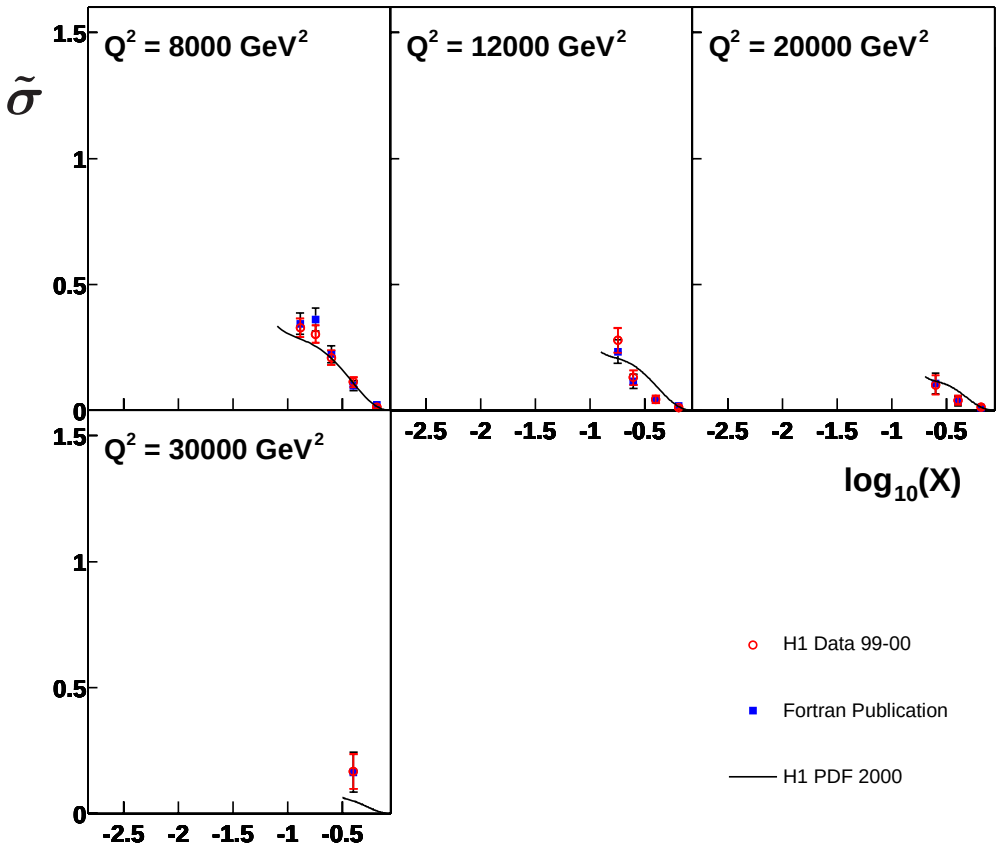

Figure 8.5: The reduced cross section, plotted against x in bins of Q^2. The red points are the results of the object orientated analysis using 99-00 e^+p data, with the error bars delimiting the statistical uncertainty (inner) and total uncertainty (outer) including the systematic errors. The blue points are the results from the latest H1 paper, with the error bars showing the total error. The solid line is the theoretical prediction of the H1 PDF 2000 fit. The bins shown in this figure range from $Q^2 = 8000$ GeV^2 to $Q^2 = 30000$ GeV^2

$$x\tilde{F}_3^{\,extracted} = \frac{Y_+}{Y_-}\left[\tilde{F}_2^{\,fit} - \tilde{\sigma}^{NC}(e^+p)\right]. \tag{8.1}$$

Although the extraction of $x\tilde{F}_3$ is strongly dependent on our theoretical understanding of $\tilde{F}_2$, we can simulate $\tilde{F}_2$ to a high precision, as was shown in section 2.5.2. Additionally, by using only the e^+p sample, it is possible to exclude completely the large errors due to low statistics of the e^-p data.

The reduced cross section has been measured in the present analysis using the Q^2 integrated binning. Figure 8.6 (top) compares the results of the measurement (the red-circle data points) with the H1 PDF 2000 fit prediction (solid line) and a H1 PDF 2000 fit prediction which excludes the $x\tilde{F}_3$ contribution to the total cross section (dashed line). The small separation suggests that the error on $x\tilde{F}_3$ will generally be large. The total error is typically of the order of $\sim 4\%$, ranging from 3% to 6%, but increasing to $10-40\%$ for the highest points in x of the highest Q^2 bin.

The $x\tilde{F}_3$ extraction results are plotted in figure 8.6 (bottom), comparing the extraction results to those measured using both e^+ and e^- data. The extraction method errors are typically of the same order of magnitude as those obtained from the measurement method. The errors on the extraction are almost entirely due to the errors on the integrated NC cross section measurement. This is because to obtain the magnitude of the error on the extraction of $x\tilde{F}_3$ the magnitude of the error on the measurement of $\tilde{\sigma}(e^+p)$ is multiplied by the y ratio $\frac{Y_+}{Y_-}$, which is always greater than 1. As $x\tilde{F}_3$ is at most a 10% contribution to the total cross section, the low errors of the NC cross section measurement result in a typical total error of 40% on the extraction of $x\tilde{F}_3$, ranging from 30% up to 400% in the least advantageous regions of phase space, where the y ratio can be greater than 30. The longitudinal structure function, $\tilde{F}_L$, only has a significant effect on the lowest point in x of the lowest Q^2 bin and has a negligible effect in all other bins.

8.5 Conclusion

A measurement of the NC cross section in high Q^2 e^+p scattering has been presented. The results were presented as both double differential and single differential cross sections in x and Q^2. The results using this independent OO analysis framework are consistent with published H1 values for the same data set, giving confidence that the OO code can be used in future analysis.

$x\tilde{F}_3$ can be measured using both e^+p and e^-p data by subtracting the NC cross sections. The error on the measurement using this method is statistically limited and can only be significantly reduced with further e^-p running. An extraction of $x\tilde{F}_3$ from the 99-00 e^+p data alone has been performed, using the NC cross section measured in the integrated Q^2 binning scheme. The technique involves using the results of a NLO QCD fit (H1 PDF 2000) to subtract the contribution of the generalised structure function, $\tilde{F}_2$. The resulting

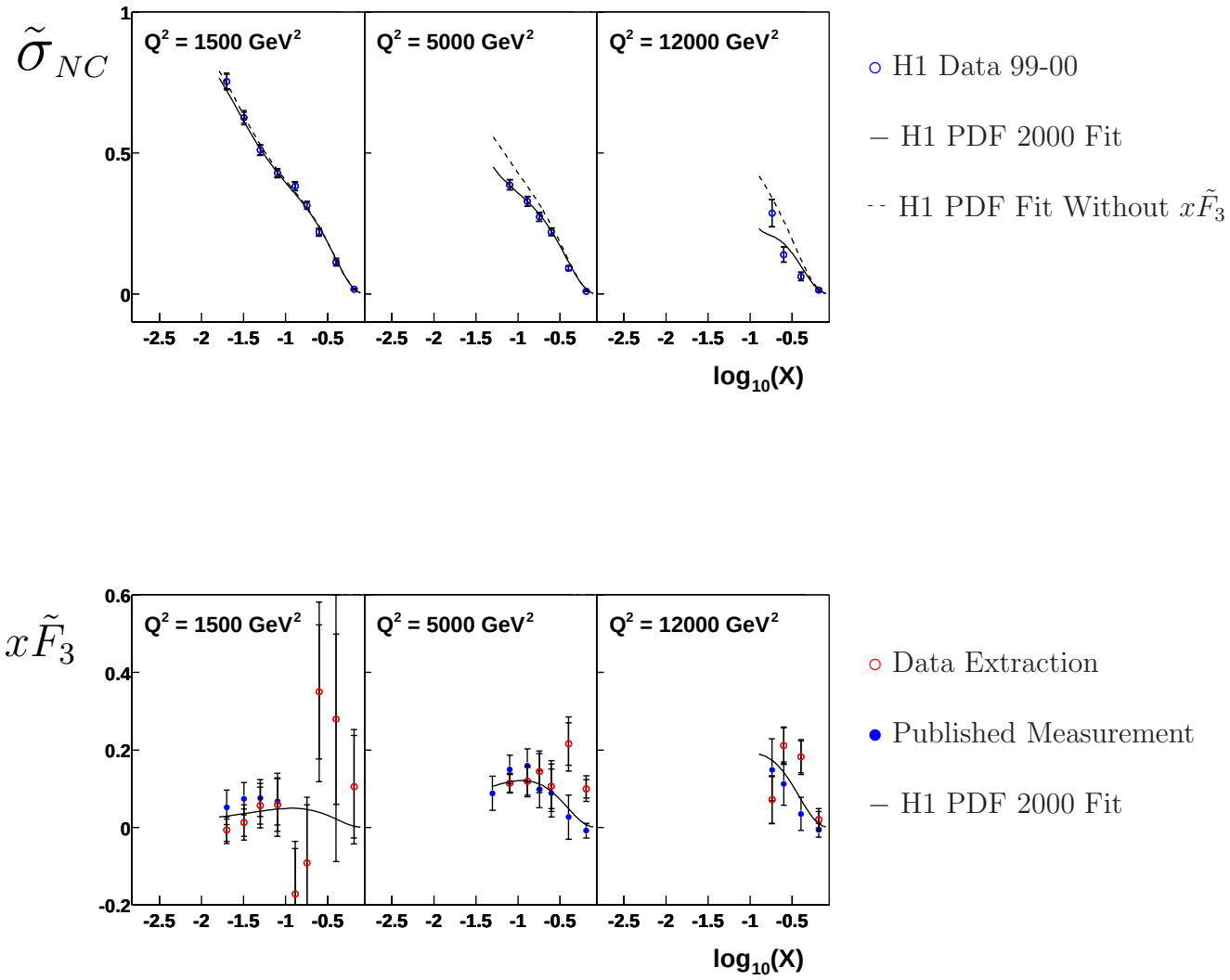

Figure 8.6: Top: The reduced cross section, measured in integrated bins of Q^2 plotted against x. The blue circles are the results of the Object Orientated analysis using 99-00 e^+p data. The solid line is the theoretical reduced cross section prediction of the H1 PDF 2000 fit. The dashed line is the theoretical prediction of the reduced cross section without a contribution from the $x\tilde{F}_3$ term. Bottom: The $x\tilde{F}_3$ extraction measured in integrated bins of Q^2 plotted against x. The red circles are the results of the Object Orientated analysis using 99-00 e^+p data, with the error bars delimiting the statistical uncertainty (inner) and total uncertainty (outer) including systematic errors. The blue points are the results of the latest H1 $x\tilde{F}_3$ measurement, with the error bars showing the total uncertainty. The solid line is the theoretical prediction of the H1 PDF 2000 fit.

extraction of $x\tilde{F}_3$ is found to be in good agreement with the measurement from e^+p and e^-p data. The combined statistical and systematic uncertainties of the extraction are found to be comparable to the measurement method. The results are also well described by the NLO QCD fit. The extraction relies on the theoretical understanding of $\tilde{F}_2$, but still serves as an interesting cross-check of the internal consistency of the data and our understanding of NLO QCD.

Chapter 9

Hera II Data

9.1 Introduction

This chapter describes the recent data recorded following the H1 and HERA upgrades and the new Data Quality tools developed in 2002-2003. The chapter begins with a description of the luminosity upgrade and a brief overview of the changes made to the H1 detector. This is followed by a discussion of the possible new physics accessible with a polarised electron beam. The Neutral Current Data Quality tool is then described and the resulting trigger efficiency evaluations and data quality plots are shown. The chapter finishes with an outline of the future of the Data Quality tools at H1 and the current role that the tool plays.

9.2 The Upgrade Project

9.2.1 The HERA Upgrade

From September 2000 to October 2002 HERA underwent an extensive upgrade project. The main aim of the upgrade was to increase the instantaneous luminosity by approximately a factor of 5. The instantaneous luminosity ($\mathcal{L}$) has the dependences

$$\mathcal{L} \propto \frac{I_e I_p}{\delta_x \delta_y} \tag{9.1}$$

where I_p is the proton current, I_e is the electron current and δ_x and δ_y are the beam spot widths such that $\delta_x \delta_y$ is the cross sectional area of the interaction region. From equation 9.1 we see that there are two ways to increase luminosity: the first is to increase the beam currents, which increases the number of interactions and the second is to reduce the

size of the interaction region in the transverse plane. It was decided to reduce the beam interaction region as a significant increase in the beam currents requires significant modifications to the detector and pre-accelerators [81]. Reducing the beam interaction region was accomplished by using superconducting focusing magnets. As this was expected to bring about an increase in synchrotron radiation, radiation masks and new collimators were added to H1 and the circular beampipe was exchanged for an elliptical one. The specifications for the second phase, HERA II, running are compared to those achieved for HERA I running in 2000 in table 9.1.

	HERA I (2000)		HERA II	
	e-beam	p-beam	e-beam	p-beam
Energy	27.5 GeV	920 GeV	27.5 GeV	920 GeV
N of Bunches total/colliding	189/174	180/174	189/174	180/174
Particles per bunch	$3.5{\cdot}10^{10}$	$7.3{\cdot}10^{10}$	$4.0{\cdot}10^{10}$	$10.3{\cdot}10^{10}$
Beam Current	50 mA	100 mA	58 mA	140 mA
Beam Size $\delta_x \times \delta_y$ (in μm)	192×50	189×50	112×30	112×30
Luminosity	$1.69 \cdot 10^{31}\text{cm}^{-2}\text{s}^{-1}$		$7.57 \cdot 10^{31}\text{cm}^{-2}\text{s}^{-1}$	
Luminosity (Specific)	$0.66 \cdot 10^{30}\text{cm}^{-2}\text{s}^{-1}\text{mA}^{-2}$		$1.82 \cdot 10^{30}\text{cm}^{-2}\text{s}^{-1}\text{mA}^{-2}$	
Luminosity Increase	4.5			

Table 9.1: A comparison of the design parameters for HERA I and II.

9.2.2 The H1 Upgrade

During the HERA upgrade period, many parts of the H1 detector were also upgraded, with an emphasis on improving the tracking and triggering.

The FTD was upgraded, to increase the precision and efficiency of measurements in the forward region. Three new planar drift chambers were added to the detector, replacing the transistor radiators, FWPCs and three of the radial drift chambers. A silicon tracker (the FST) was also added in the forward region. The increased track-finding precision and efficiency in the forward region will allow a more accurate determination of the hadronic final state which is needed, for example, in the investigation of the heavy flavour quark content of the proton. The increased forward sensitivity can also be used to detect electrons in high Q^2 events and reconstruct the interaction vertex for events at low y.

The CIP was extended from two to five layers and its coverage was also extended in z. The increased z coverage will help to increase the efficiency to reject beam-gas and beam-wall background events in which the particles emanate at a large distance from the nominal interaction region.

With the luminosity upgrade it will no longer be possible to trigger on inclusive low Q^2 DIS and photoproduction events. Therefore, to facilitate the triggering of interesting final states such as vector mesons and and heavy flavour particles a new track-based trigger was devised. This Fast Track Trigger (FTT) [45] aims to make decisions using fast

pattern recognition processes based on track multiplicities and the transverse momentum of tracks, allowing online identification of decays, such as $D^{*+} \rightarrow K^-\pi^+\pi^+$, at the now implemented third trigger level (i.e. within 100 μs)

The luminosity detector was re-designed to withstand the higher radiation rates that result from higher luminosity running. In the new design, the luminosity is measured by a radiation hard Cherenkov tungsten-fibre calorimeter.

9.3 Polarisation

At HERA the electrons are naturally transversely polarised by the emission of synchrotron radiation. For HERA II running it was planned to achieve longitudinal electron polarisation at the H1 and ZEUS interaction points, as well as HERMES. Spin rotators were added along the beampipe at either side of the interaction point to convert the transversely polarised beam to a longitudinally polarised beam and back again.

The level of polarisation is measured at the fixed target detector sites, the now vacant east area and HERMES. The polarimeters use polarised laser light (alternately left and right circularly polarised) to measure the Compton scattering of polarised light off the electron beam. The electron beam transverse polarisation is measured in the east area by the transverse polarimeter (TPOL) and the longitudinal polarisation of the beam is measured at HERMES with the longitudinal polarimeter (LPOL). The level of electron beam polarisation achieved at H1 can be considered to be the same as that achieved at the east and west interaction sites, since the absolute value of the degree of polarisation of the electron beam is the same everywhere in the ring [82]. Two measurements of the beam polarisation are made in order to allow redundancy in the polarisation measurement and to study systematic effects.

A polarised electron beam opens up the possibility to explore a whole new dimension of proton physics. The most obvious polarisation effect occurs in the CC interaction, where the standard model cross section is directly dependent on the electron polarisation, P:

$$\frac{d^2\sigma^{\pm}_{CC}(P)}{dxdQ^2} = (1-P)\frac{G_F^2 M_W^2}{2\pi x}\left[\frac{1}{Q^2+M_W^2}\right]^2\left(Y_+\tilde{W}_2^{\pm} + y^2\tilde{W}_L^{\pm} \mp Y_- x\tilde{W}_3\right) \tag{9.2}$$

The strong dependence of the standard model cross section on the polarisation can be established with relatively small luminosities, as shown in figure 9.1. Any future deviation from the expected linear trend will represent a clear signal of physics beyond the standard model.

The Neutral Current interaction has a less dramatic dependence on the electron polarisation. Lepton polarisation is expected to have a significant effect only in the very high Q^2 region due to sensitivity to the structure functions representing the polarisation dependence, $\tilde{F_2}^P$ and the truly parity violating structure function, $x\tilde{F_3}^P$. The Neutral Current

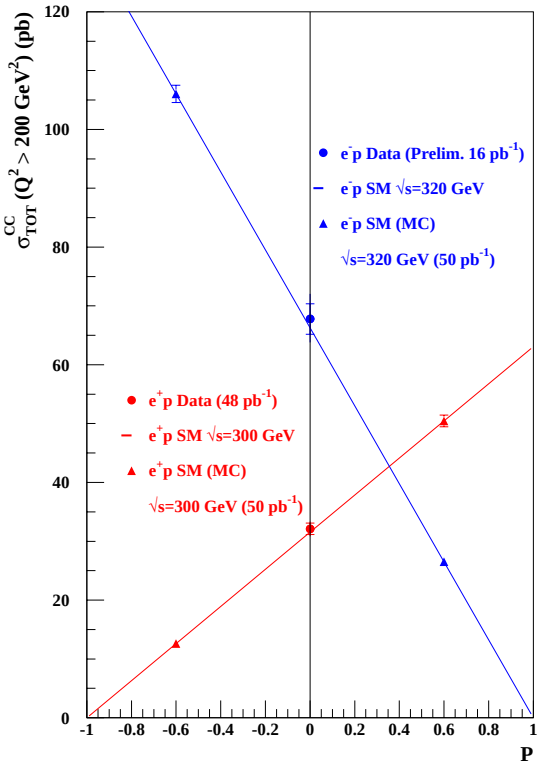

Figure 9.1: The theoretical prediction for CC measurements with a polarised electron beam, for both e^+ and e^- running. The points at P $= \pm 0.6$ are simulated predictions, while the points at P $= 0$ are the measured cross section results.

Cross section, with a polarised lepton beam, is expressed in terms of structure functions in equation 9.3 (neglecting the $\tilde{F}_L$ term, which is not expected to contribute significantly at high Q^2) and the predicted cross section is plotted in figure 9.2.

$$\frac{d^2\sigma^{\pm}_{NC}(P)}{dxdQ^2} \propto \left[Y_+\tilde{F}_2 \mp Y_- x\tilde{F}_3 + P(\pm Y_+ \tilde{F_2}^P + Y_- x\tilde{F_3}^P)\right] \tag{9.3}$$

$\tilde{F_2}^P$ and $x\tilde{F_3}^P$ can be expressed in term of their electromagnetic, electroweak (γZ^0) mixing and purely weak (Z^0) components [83], using the same definitions used to express $\tilde{F}_2$ and $x\tilde{F}_3$ in equations 2.9 and 2.10:

$$\tilde{F_2}^P = -a_e \frac{k_w Q^2}{Q^2 + {M_Z}^2} F_2^{\gamma Z^0} + 2 v_e a_e \left[\frac{k_w Q^2}{Q^2 + {M_Z}^2}\right]^2 F_2^{Z^0} \tag{9.4}$$

$$x\tilde{F_3}^P = v_e \frac{k_w Q^2}{Q^2 + {M_Z}^2} x F_3^{\gamma Z^0} - (v_e^2 + a_e^2) \left[\frac{k_w Q^2}{Q^2 + {M_Z}^2}\right]^2 x F_3^{Z^0} \tag{9.5}$$

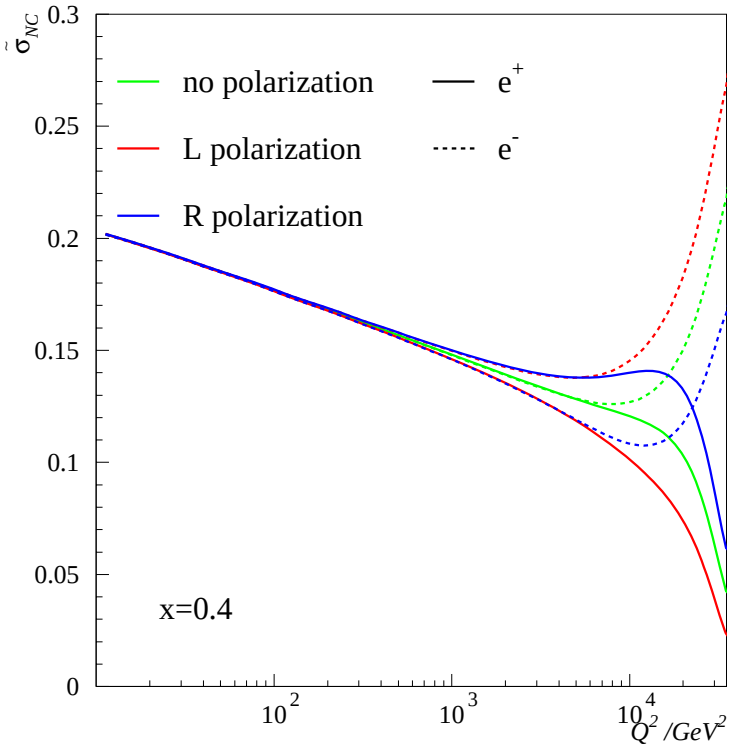

Figure 9.2: The theoretically predicted NC Cross Section for electron and positron beams with left and right handed polarisation, compared to the unpolarised theoretical curve.

With the definitions of the polarised structure functions, it is possible to obtain a value for the polarisation asymmetry function in terms of the structure function components (remembering that $a_e \gg v_e$, as was shown in equation 2.11)

$$A^{\pm} = \frac{\tilde{\sigma}^{\pm}(P) - \tilde{\sigma}^{\pm}(P)}{\tilde{\sigma}^{\pm}(P) + \tilde{\sigma}^{\pm}(P)} \simeq \pm P \frac{k_w Q^2}{Q^2 + {M_Z}^2} a_e \frac{F_2^{\gamma Z^0}}{F_2} \tag{9.6}$$

$$\rightarrow \pm P \frac{k_w Q^2}{Q^2 + {M_Z}^2} \frac{1 + (d_v/u_v)}{4 + (d_v/u_v)}\Big|_{(lim:x\rightarrow 1)}$$

which will allow neutral current events to be used to probe the d quark contribution to the valence quarks of the proton at high x [84].

9.4 Data Quality Tools

The HERA II data-taking started in October 2002 and it was important to monitor the early data to ensure that the detector was performing as planned and data-taking was proceeding correctly. For this purpose an analysis package was devised to monitor the new data as it became available.

The framework used to monitor the data quality was a modified version of the neutral current analysis package used to obtain the results outlined in chapter 8, with some cuts loosened and others removed. The list of cuts used in this package is outlined in table 9.2 below.

Cut	*Description*
$E_e > 11$ GeV	Unchanged from HERA I analysis
$y_e < 0.9$	Unchanged from HERA I analysis
$E - P_z > 35$ GeV	Unchanged from HERA I analysis
$\|z-$vertex$\| < 50$ cm	Cut loosened as nominal vertex uncertain
$Q^2 > 133$ GeV^2	LAr acceptance cut
Track-Cluster Link <12 cm	Simplified DTRA Track Cluster Cut
LAr On & CJC On	Basic HV requirement
Require LAr electron	Unchanged from HERA I analysis

Table 9.2: A list of the cuts used to monitor the data quality.

The background finders were not used, as it could not be assumed that the detector would work in the same way as it did in 2000 and there was not enough data taken to check the background finder efficiency. All the run-dependent cuts were also dropped and the subtrigger selection was changed, as the subtriggers used in HERA II running do not match those used in previous running. The nominal interaction position could also have changed during the upgrade and therefore the z-vertex cut was loosened. The analysis was restricted to a region of high, and well understood, acceptance. For this reason a cut of $Q^2 > 133$ GeV^2 was imposed. This cut also made it possible to run with a subset of the Model MC, increasing analysis speed while maintaining a high MC to data statistics ratio. The track-cluster cut required linking within 12 cm and did not accept events with a poor track-cluster link in the forward region.

9.5 Data Quality Plots and New Data Efficiencies

In the early data-taking period the CIP was still being commissioned. Additionally, as part of the FTD upgrade, the FWPCs were replaced with two layers of plastic scintillators, FTI1 and FTI2. Unfortunately, one of the two scintillators (FTI1) suffered a hardware failure, rendering it useless for triggering purposes so far. These two setbacks combined to leave a gap in track-based timing triggering, formerly filled by the Ray_T0 trigger (see section 3.8.2). The DCRϕ trigger system was the only usable track-based trigger for the 2002-2003 data-taking.

Following the upgrade it was crucial to ensure that the detector was running with the highest possible trigger efficiency for high Q^2 NC processes. A subtrigger combining the DCRϕ and LAr trigger elements was used to select NC events.

The DCRϕ_T0 trigger element was monitored by an independent monitor trigger, which is comprised of LAr_el1 && LAr_T0. The LAr_T0 trigger element was monitored by a

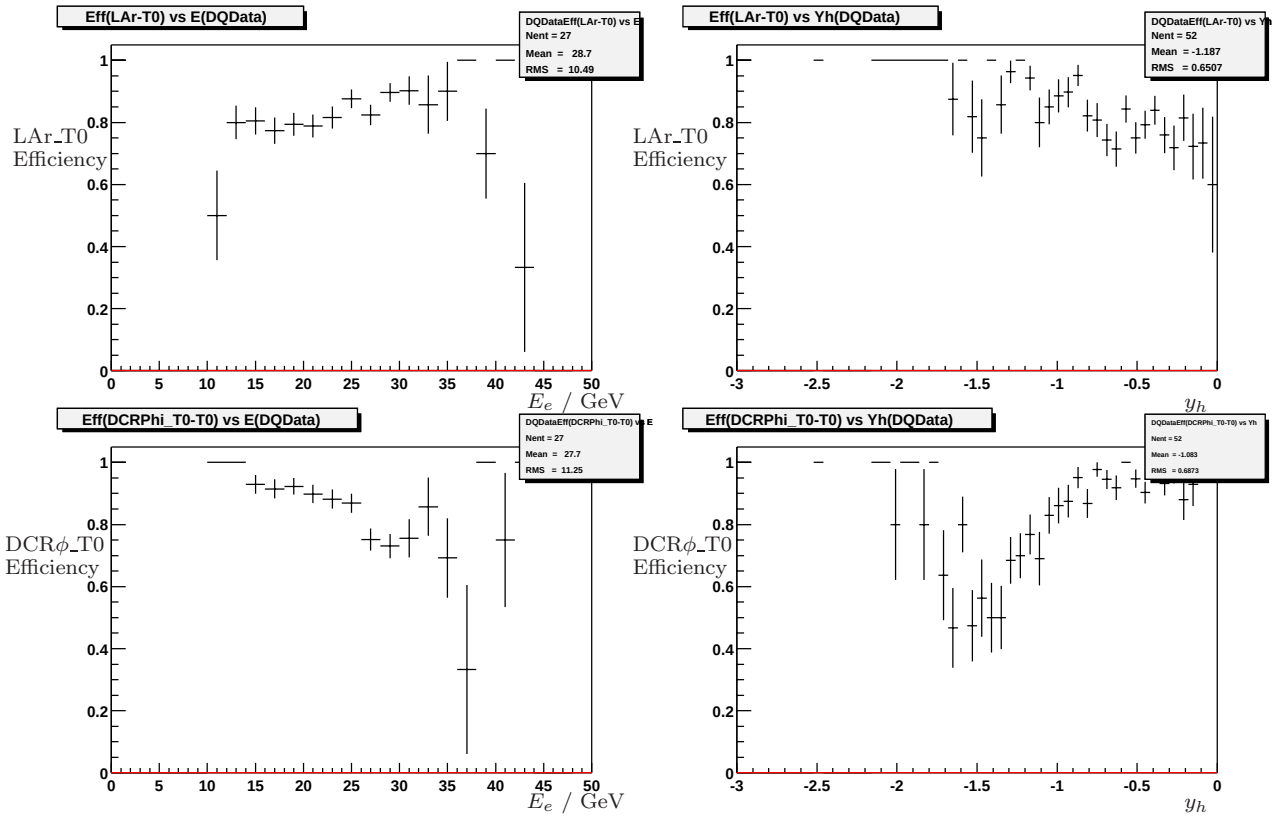

Figure 9.3: Top: The HERA II LAr_T0 Trigger Efficiency, plotted as a function of scattered electron energy (left) and y_h (right). Bottom: The HERA II DCRϕ_T0 Trigger Efficiency, plotted as a function of scattered electron energy (left) and y_h (right).

subtrigger formed by LAr_el1 &&(LAr_T0||DCRϕ_T0). The calculated trigger efficiencies are shown in figure 9.3. The LAr_T0 is seen to perform at 85% efficiency (compared to 90% for HERA I running, described in section 6.4). The DCRϕ_T0 has a 83% efficiency. Without the Ray_T0 trigger it was not possible to monitor the LAr_el(1&2) trigger elements.

While accounting for the uncertainty of the unmeasured LAr_el trigger efficiencies, it is possible to compare the data with the MC model prediction scaled to the cross section measured in the HERA I analysis. The following plots show the $\log Q^2$, z-vertex, scattered electron energy and $E - Pz$ distributions for data taken between October 2002 and February 2003, for an integrated luminosity of about 3 pb^{-1}. During this data-taking period, the spin-rotators were not in use and the data were therefore not polarised.

The data lie below the MC prediction by approximately 13%, with no strong dependence on any of the kinematic variables. This is in keeping with the data-taking inefficiency predicted by the studies of the LAr_T0 efficiency. Additionally, the preliminary uncertainty of the luminosity measurement was estimated to be approximately 10% for this data.

The plots show the expected trends. The $\log_{10} Q^2$ distribution peaks at $Q^2 = 200$ GeV^2, with the highest Q^2 event measured at $Q^2 = 16000$ GeV^2. The z-vertex distribution

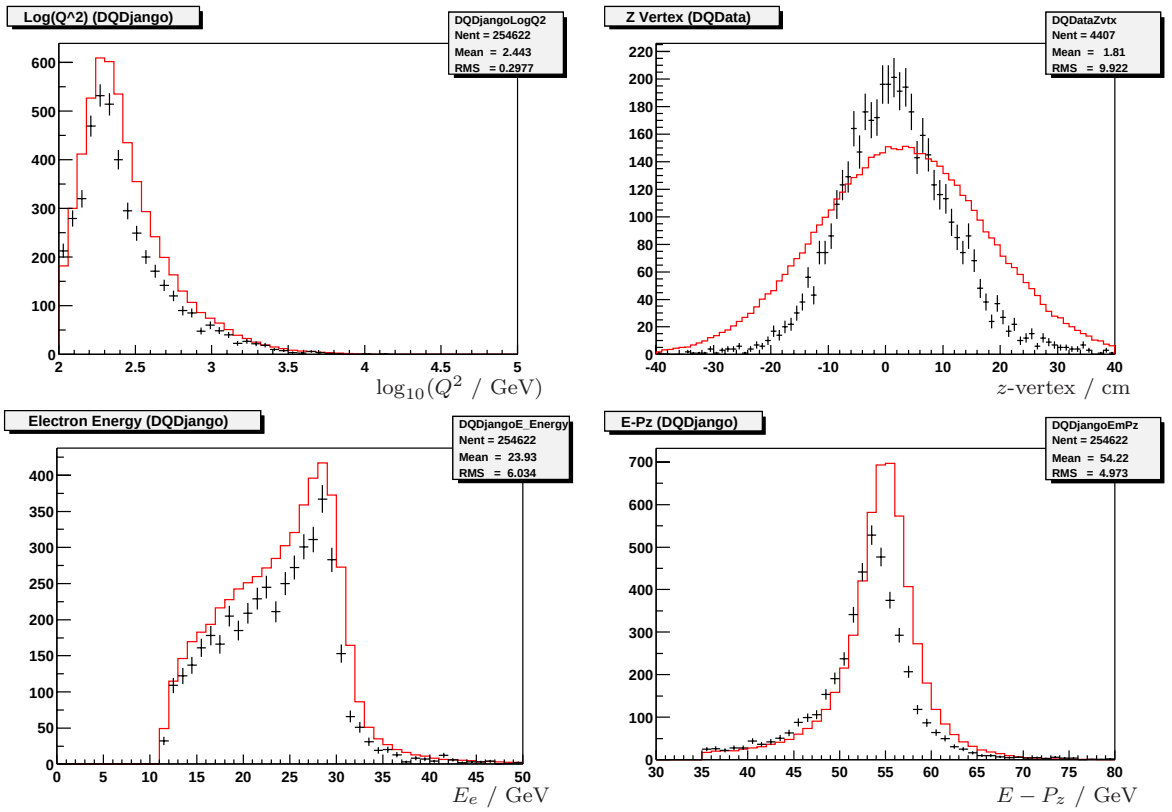

Figure 9.4: Data quality variable plots, showing the distributions for $log_{10}Q^2$ (top left), the z-vertex distribution, the scattered electron energy (bottom left) and the total $E-Pz$ (bottom right).

is Gaussian in shape, symmetrical and roughly centred about +1 cm. It is immediately apparent that the MC has not been reweighted to fit the data distribution (see section 6.5). The electron energy distribution starts at the cut value of 11 GeV and peaks at 27.5 GeV, followed by a sharp drop. Finally, the $E - P_z$ distribution is symmetrical, peaking at the expected 55 GeV for the MC, but somewhat lower for the data, which are uncalibrated. The z-vertex reweight and electron and hadronic calibrations are all dependent on the running conditions and have not been applied to the data quality analysis.

9.6 Recent Developments

The package was initially used to monitor data as part of the Data Quality Representative duties for the Inclusive Measurements group and then was used as a part of the Data Quality group's online data quality tool. It performed an important task, verifying the detector performance, especially that of the LAr. It was subsequently adopted by other analysis groups. The Data Quality Package outlined in this chapter is still being used by the Inclusive Measurements group, in addition to the online tool. It was also used

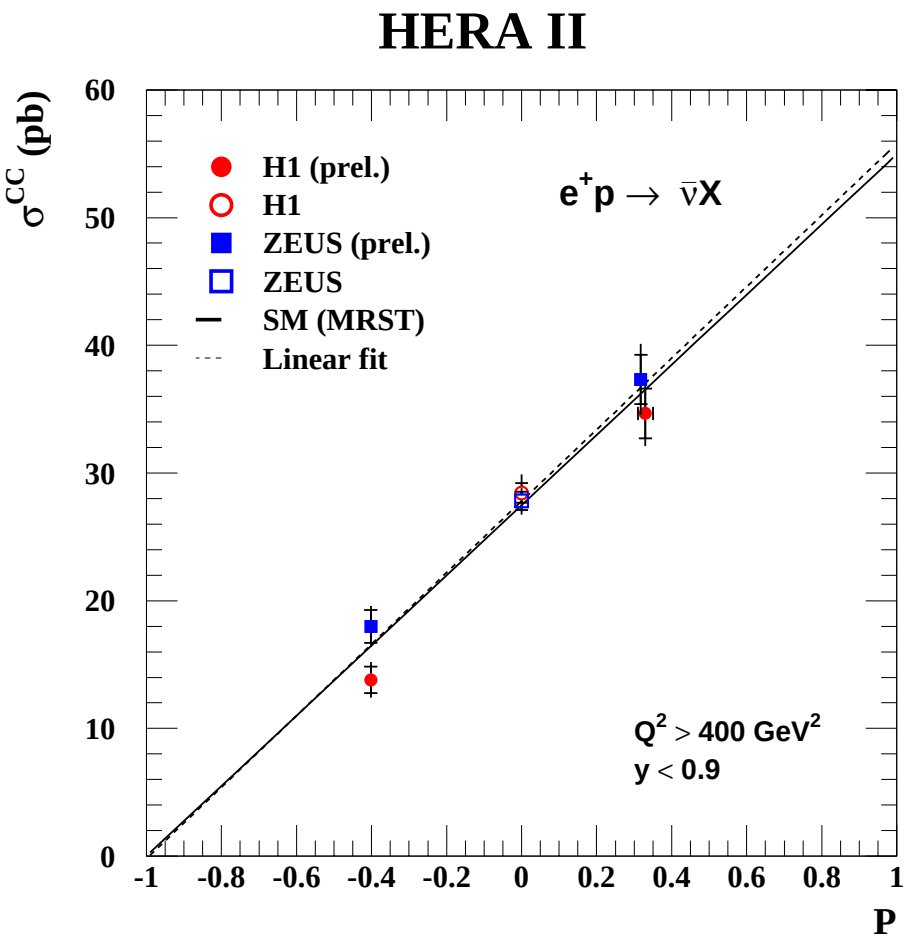

Figure 9.5: The preliminary polarised CC cross section measurements using HERA II data.

as a starting point for the subsequent analysis of the most recent data [85], to make a measurement of HERA II neutral current interactions with polarised electron beams [86] and to obtain preliminary polarised charged current results [86], plotted in figure 9.5. The results were obtained using left and right handed polarised e^+ beams. The left handed data achieved a mean polarisation of -40% and totalled an integrated luminosity of 21.7 pb^{-1}. The right handed data achieved a mean polarisation of 33% and totalled an integrated luminosity of 15.3 pb^{-1}. The results are found to be consistent with the standard model expectations within the experimental errors.

Chapter 10

Summary

In this thesis measurements of the e^+p inclusive neutral current deep inelastic scattering cross section have been presented. The analysis was performed on e^+p collision data with a centre of mass energy of $\sqrt{s} = 319$ GeV. The data were taken using the H1 detector in the 1999-2000 running period and correspond to an integrated luminosity of $\mathcal{L} = 65.2$ pb^{-1}. The analysis was performed using the latest Object Orientated, C++, analysis framework, which replaces and supersedes previously existing techniques. The single and double differential cross sections were measured as a function of Bjorken-x and the momentum transfer squared, Q^2.

The measurement of the single differential cross section, $d\sigma/dQ^2$, covers a Q^2 range of over three orders of magnitude and the cross section falls by seven orders of magnitude. At the highest values of Q^2, comparable to the Z^0 and $W^{\pm}$ masses, the NC cross section is of similar size to that of the CC cross section. This illustrates the unification of the electromagnetic and weak forces in the deep inelastic scattering. The results are well described by the predictions of the NLO QCD fit to H1 data. The typical uncertainties on the measurement are of the order of a few percent, but rise significantly for high Q^2 values, where the measurement is statistically limited. The reduced NC cross section, $d\sigma/dx$, is also well described by the NLO QCD prediction. The accuracy of the measurement has reached the level of a few percent.

The double differential reduced cross section was measured over three orders of magnitude in both x and Q^2. The uncertainties on the measurement are typically a few percent in the medium Q^2 range, increasing significantly for the points measured at the highest values of Q^2, where the measurement is statistically limited. The results obtained are in good agreement with the latest published results of a FORTRAN analysis on the entire e^+p data-set. The results are also well modelled by the NLO QCD fits to the same dataset.

In the high Q^2 region the cross section is sensitive to the valence quark structure function, $x\tilde{F}_3$. $x\tilde{F}_3$ was extracted from the double differential cross section, subtracting the contribution of the generalised structure function, $\tilde{F}_2$, predicted by the latest H1 NLO QCD fit. The extraction is found to be in good agreement with the previous measurement from e^+p and e^-p data. The combined statistical and systematic uncertainties of the extraction are

found to be comparable to those of the measurement method. The results are also well described by the NLO QCD fit.

The HERA luminosity upgrade has also been described, as well as the initial efforts at monitoring the post-upgrade data and the first efforts at creating a data quality analysis package, using a simplified version of the analysis code used in this thesis. The trigger efficiencies and detector performance during data commissioning at the start of the HERA II running were also studied.

Appendix A

Q^2	x	$d\tilde{\sigma}/dQ^2dx$	Statistical Error	Total Error
100	0.002	1.40485	0.0189517	0.0440067
120	0.002	1.33428	0.0190185	0.052455
150	0.002	1.34344	0.053609	0.0995827
120	0.0032	1.2211	0.0156436	0.0300295
150	0.0032	1.20001	0.0147969	0.0315334
200	0.0032	1.18831	0.0234722	0.0457942
250	0.0032	1.18951	0.0585322	0.131145
120	0.005	1.16325	0.0281716	0.0682962
150	0.005	1.07586	0.0134693	0.0251729
200	0.005	1.09192	0.014829	0.0314589
250	0.005	1.14083	0.0189718	0.0320191
300	0.005	1.10972	0.0271797	0.0402667
400	0.005	1.03457	0.079348	0.139888
150	0.008	0.899669	0.0145984	0.0257184
200	0.008	0.941739	0.0125132	0.0213963
250	0.008	0.88533	0.0144535	0.0264164
300	0.008	0.954006	0.017783	0.0267343
400	0.008	1.00474	0.0224329	0.034981
500	0.008	0.989656	0.0367043	0.0492623
650	0.008	0.828971	0.0812873	0.115625
150	0.013	0.83151	0.0187104	0.0601702
200	0.013	0.795659	0.0111458	0.0190105
250	0.013	0.810203	0.0126087	0.0230821
300	0.013	0.803943	0.0155848	0.0222335
400	0.013	0.875234	0.0181087	0.0245951
500	0.013	0.854497	0.0221667	0.0304382
650	0.013	0.842205	0.0264876	0.0341651
800	0.013	0.88944	0.039777	0.0506849
1000	0.013	0.919199	0.0410259	0.0475298
1200	0.013	0.886288	0.0607275	0.0747136

Table A.1:

Q^2	x	$d\tilde{\sigma}/dQ^2dx$	Statistical Error	Total Error
150	0.02	0.817749	0.0236656	0.0588335
200	0.02	0.718817	0.0112137	0.0187366
250	0.02	0.711889	0.0109677	0.0212294
300	0.02	0.68422	0.0133267	0.0201916
400	0.02	0.726632	0.016248	0.0216112
500	0.02	0.700166	0.0174389	0.022471
650	0.02	0.696484	0.0226327	0.0304744
800	0.02	0.749269	0.0261816	0.0328461
1000	0.02	0.762446	0.0291103	0.0358566
1200	0.02	0.767989	0.0360833	0.041391
1500	0.02	0.717628	0.0417819	0.0447536
2000	0.02	0.804234	0.0713642	0.0827378
150	0.032	0.642412	0.0234889	0.0690017
200	0.032	0.606183	0.0105619	0.0195152
250	0.032	0.588842	0.00968704	0.0191868
300	0.032	0.589455	0.0113927	0.0227261
400	0.032	0.595187	0.0141232	0.0180262
500	0.032	0.615794	0.0154383	0.0185467
650	0.032	0.581543	0.0175742	0.0233845
800	0.032	0.539146	0.0216352	0.0254461
1000	0.032	0.695385	0.0272753	0.031879
1200	0.032	0.652691	0.0292478	0.0331444
1500	0.032	0.601418	0.0343808	0.0384502
2000	0.032	0.597145	0.0383069	0.0427668
3000	0.032	0.602698	0.038118	0.0438287
150	0.05	0.555662	0.0247757	0.0625694
200	0.05	0.497935	0.00984901	0.0172905
250	0.05	0.502213	0.0086886	0.0137186
300	0.05	0.495221	0.0102837	0.0188418
400	0.05	0.497516	0.0126903	0.0173037
500	0.05	0.523511	0.0139467	0.0167852
650	0.05	0.483659	0.0150557	0.0204784
800	0.05	0.538715	0.0207659	0.0231017
1000	0.05	0.588163	0.0245709	0.0274195
1200	0.05	0.499746	0.0236108	0.0253614
1500	0.05	0.563152	0.0293165	0.032237
2000	0.05	0.450583	0.0326887	0.0348306
3000	0.05	0.56616	0.0302194	0.035335
5000	0.05	0.450595	0.0395198	0.045111

Table A.2:

200	0.08	0.417404	0.00938047	0.0171497
250	0.08	0.405017	0.0076067	0.0116655
300	0.08	0.421901	0.00895033	0.0167407
400	0.08	0.424933	0.0113044	0.0147656
500	0.08	0.429132	0.0122211	0.0148275
650	0.08	0.432403	0.0136738	0.0177022
800	0.08	0.423775	0.0170605	0.0204458
1000	0.08	0.446591	0.0209595	0.0222126
1200	0.08	0.455641	0.0221279	0.0240801
1500	0.08	0.430478	0.0232436	0.0247655
2000	0.08	0.38126	0.0258816	0.0275358
3000	0.08	0.414123	0.0256335	0.0272757
5000	0.08	0.389587	0.0267569	0.0291062
8000	0.08	0.368809	0.0537963	0.0563611
200	0.13	0.31787	0.0105085	0.0171565
250	0.13	0.315639	0.00783245	0.0157741
300	0.13	0.346941	0.00917141	0.0197948
400	0.13	0.349368	0.0112524	0.0148646
500	0.13	0.318729	0.0114417	0.0130295
650	0.13	0.336262	0.0128761	0.015253
800	0.13	0.357918	0.0163537	0.0196816
1000	0.13	0.432196	0.0226222	0.0249347
1200	0.13	0.395299	0.0229376	0.0243128
1500	0.13	0.385259	0.024464	0.0260484
2000	0.13	0.358455	0.0260738	0.0272946
3000	0.13	0.328692	0.0236598	0.0248535
5000	0.13	0.329163	0.0272417	0.0286605
8000	0.13	0.328202	0.0360249	0.0370891
12000	0.13	0.074871	0.024957	0.0252978
200	0.18	0.273222	0.0116291	0.0187272
250	0.18	0.288367	0.00920685	0.0225844
300	0.18	0.278952	0.00959624	0.0185964
400	0.18	0.27991	0.0113239	0.0201422
500	0.18	0.270027	0.0113702	0.0165145
650	0.18	0.272978	0.0119251	0.0155606
800	0.18	0.277779	0.0148267	0.0166418
1000	0.18	0.322198	0.0206266	0.0221346
1200	0.18	0.331586	0.0213152	0.0223077
1500	0.18	0.313757	0.0216513	0.0225804
2000	0.18	0.290079	0.0237642	0.0250292
3000	0.18	0.2729	0.0216424	0.0223495
5000	0.18	0.253964	0.0236823	0.0254995
8000	0.18	0.302919	0.0334518	0.0358551
12000	0.18	0.277816	0.0483616	0.0493641

Table A.3:

250	0.25	0.213196	0.00907424	0.0158918
300	0.25	0.260857	0.0117247	0.0237127
400	0.25	0.219545	0.0122538	0.019409
500	0.25	0.268804	0.0145141	0.0242716
650	0.25	0.23215	0.013164	0.0249682
800	0.25	0.251748	0.0161165	0.0346021
1000	0.25	0.238671	0.0180936	0.0223523
1200	0.25	0.231616	0.0180313	0.0212065
1500	0.25	0.215425	0.0174733	0.0192447
2000	0.25	0.207498	0.0194339	0.0214777
3000	0.25	0.194986	0.0167199	0.0174732
5000	0.25	0.269079	0.0246664	0.0260444
8000	0.25	0.209417	0.0279845	0.0297826
12000	0.25	0.129822	0.0283295	0.0296556
20000	0.25	0.101294	0.0382857	0.0385077
300	0.4	0.135589	0.0084251	0.0117626
400	0.4	0.130075	0.0102197	0.0148753
500	0.4	0.123942	0.0109981	0.0137376
650	0.4	0.118185	0.0123892	0.0150843
800	0.4	0.107266	0.012386	0.0137471
1000	0.4	0.116819	0.0150813	0.0205363
1200	0.4	0.141744	0.0171889	0.0214281
1500	0.4	0.106347	0.0133985	0.0184483
2000	0.4	0.0944632	0.0127374	0.0150485
3000	0.4	0.0801057	0.00978647	0.0107695
5000	0.4	0.0971496	0.0126478	0.0138719
8000	0.4	0.11231	0.0184637	0.0212375
12000	0.4	0.0436425	0.0145475	0.0152636
20000	0.4	0.0403882	0.0180621	0.0184017
30000	0.4	0.166672	0.0680434	0.0695146
400	0.65	0.0214014	0.00209858	0.00255264
650	0.65	0.024348	0.00319705	0.0041259
800	0.65	0.0175609	0.00351217	0.00385575
1000	0.65	0.0220672	0.00493437	0.00512201
1200	0.65	0.019697	0.00508574	0.00535748
1500	0.65	0.00973632	0.00435421	0.0043747
2000	0.65	0.0198646	0.00598939	0.00691731
3000	0.65	0.0069666	0.0023222	0.00265253
5000	0.65	0.0101819	0.00359983	0.00408837
8000	0.65	0.0144214	0.00456046	0.00544778
12000	0.65	0.0114901	0.00513854	0.00596326
20000	0.65	0.014117	0.0070585	0.00833364
60000	0.65	0.0427106	0.0427106	0.0442683

Table A.4:

Bibliography

[1] G. D. Coughlan and J. E. Dodd, "The Ideas of particle physics: An Introduction for scientists.", Cambridge University Press, second edition 1994.

[2] D. Rutherford, Phil. Mag. **21** (1911) 669.

[3] R. Hofstader, Rev. Mod. Phys. **28** (1956) 214.

[4] E. D. Bloom *et al.*, "High-Energy Inelastic E P Scattering At 6-Degrees And 10-Degrees.", Phys. Rev. Lett. **23** (1969) 930.

[5] M. Breidenbach *et al.*, "Observed Behavior Of Highly Inelastic Electron - Proton Scattering.", Phys. Rev. Lett. **23** (1969) 935.

[6] J. D. Bjorken, "Asymptotic Sum Rules At Infinite Momentum.", Phys. Rev. **179** (1969) 1547.

[7] R. P. Feynman, "Very High-Energy Collisions Of Hadrons.", Phys. Rev. Lett. **23** (1969) 1415.

[8] M. Gell-Mann, "A Schematic Model Of Baryons And Mesons.", Phys. Lett. **8** (1964) 214.

[9] F. J. Hasert *et al.*, "Observation Of Neutrino-Like Interactions Without Muon Or Electron In The Gargamelle Neutrino Experiment.", Phys. Lett. B **46** (1973) 138.

[10] S. L. Glashow, "Partial Symmetries Of Weak Interactions.", Nucl. Phys. **22** (1961) 579;

A. Salam, "Weak And Electromagnetic Interactions."; Elementary Particle Physics: Proc. 8th Nobel Symposium, Almiquist and Wiksell, Stockholm (1968), 367;

S. Weinberg, "A Model Of Leptons.", Phys. Rev. Lett. **19** (1967) 1264.

[11] G. Arnison *et al.*, "Experimental Observation Of Isolated Large Transverse Energy Electrons With Associated Missing Energy At S**(1/2) = 540-GeV.", Phys. Lett. B **122** (1983) 103;

M. Banner *et al.*, "Inclusive Charged Particle Production At The Cern Anti-P P Collider.", Phys. Lett. B **122** (1983) 322.

[12] G. Arnison *et al.*, "Experimental Observation Of Lepton Pairs Of Invariant Mass Around 95-GeV/C**2 At The Cern Sps Collider.", Phys. Lett. B **126** (1983) 398;

P. Bagnaia *et al.*, "Evidence For Z0 → E+ E- At The Cern Anti-P P Collider.", Phys. Lett. B **129** (1983) 130.

[13] D. J. Fox *et al.*, "Test Of Scale Invariance In High-Energy Muon Scattering.", Phys. Rev. Lett. **33** (1974) 1504;

Y. Watanabe *et al.*, "Test Of Scale Invariance In Ratios Of Muon Scattering Cross-Sections At 150-GeV And 56-GeV.", Phys. Rev. Lett. **35** (1975) 898;

H. L. Anderson *et al.*, "Measurement Of The Proton Structure Function From Muon Scattering.", Phys. Rev. Lett. **38** (1977) 1450;

B. A. Gordon *et al.*, "Muon Scattering At 219-GeV And The Proton Structure Functions.", Phys. Rev. Lett. **41** (1978) 615;

J. J. Aubert *et al.*,"Production Of Charmed Particles In 250-GeV Mu+ - Iron Interactions.", Nucl. Phys. B **213** (1983) 31;

M. R. Adams *et al.*,"Shadowing in inelastic scattering of muons on carbon, calcium and lead at low x(Bj).", Z. Phys. C **67** (1995) 403.

[14] A. C. Benvenuti *et al.*,"A High Statistics Measurement Of The Proton Structure Functions F(2) (X,Q**2) And R From Deep Inelastic Muon Scattering At High Q**2.", Phys. Lett. B **223** (1989) 485.

[15] M. Arneodo *et al.*,"Measurement of the proton and the deuteron structure functions, F2(p) and F2(d).", Phys. Lett. B **364** (1995) 107.

[16] K. Varvell *et al.*,"Measurement Of The Structure Functions F2 And Xf3 And Comparison With QCD Predictions Including Kinematical And Dynamical Higher Twist Effects.", Z. Phys. C **36** (1987) 1.

[17] P. Z. Quintas *et al.*, "A Measurement of Lambda (MS) from muon-neutrino - Fe nonsinglet structure functions at the Fermilab tevatron.", Phys. Rev. Lett. **71** (1993) 1307.

[18] H. Abramowicz *et al.*, "Measurement Of Neutrino And Anti-Neutrinos Structure Functions In Hydrogen And Iron.", Z. Phys. C **25** (1984) 29;

J. P. Berge *et al.*, "A Measurement Of Differential Cross-Sections And Nucleon Structure Functions In Charged Current Neutrino Interactions On Iron.", Z. Phys. C **49** (1991) 187.

[19] F. Halzen and A. D. Martin, "Quarks And Leptons: An Introductory Course In Modern Particle Physics.", New York, USA: Wiley (1984) 396.

[20] R. K. Ellis, W. J. Stirling and B. R. Webber "QCD and Collider Physics", Cambridge Univ. Press (1996).

[21] D. H. Perkins, "Introduction to High Energy Physics 3rd ed.", Addison-Wesley (1987).

[22] C. Adloff *et al.*,"Measurement and QCD analysis of Neutral and Charged Current Cross Sections at HERA", DESY 03-038.

[23] C. Adloff *et al.*,"Measurement of neutral and charged current cross sections in electron proton collisions at high Q**2", Eur. Phys. J. C **19** (2001) 269.

[24] S. Bethke, "Determination of the QCD coupling alpha(s).", J. Phys. G **26** (2000) R27.

[25] Y. L. Dokshitzer, "Calculation Of The Structure Functions For Deep Inelastic Scattering And E+E- Annihilation By Perturbation Theory In Quantum Chromodynamics. (In Russian).", Sov. Phys. JETP **46** (1977) 641 Zh. Eksp. Teor. Fiz. **73** (1977) 1216;

V. N. Gribov and L. N. Lipatov, "E+ E- Pair Annihilation And Deep Inelastic E P Scattering In Perturbation Theory.", Yad. Fiz. **15** (1972) 1218 Sov. J. Nucl. Phys. **15** (1972) 438 and 675;

G. Altarelli and G. Parisi, "Asymptotic Freedom In Parton Language.", Nucl. Phys. B **126** (1977) 298;

G. Curci, W. Furmanski and R. Petronzio, "Evolution Of Parton Densities Beyond Leading Order: The Nonsinglet Case.", Nucl. Phys. B **175** (1980) 27;

W. Furmanski and R. Petronzio, "Singlet Parton Densities Beyond Leading Order.", Phys. Lett. B **97** (1980) 437.

[26] I. Abt *et al.*,"The Tracking, calorimeter and muon detectors of the H1 experiment at HERA.", Nucl. Instrum. Meth. A **386** (1997) 310 and 348.

[27] M. Derrick *et al.*,"A Measurement of sigma(t) (gamma p) at s**(1/2) = 210-GeV", Phys. Lett. B**293** (1992) 465.

[28] HERMES Collaboration Web Page

[29] HERA-B Collaboration Web Page

[30] W. Bartel *et al.* Proc. of the 1996 HERA Workshop, Vol. 2, DESY (1996) 1095

[31] B. Andrieu *et al.*,"Results from pion calibration runs for the H1 liquid argon calorimeter and comparisons with simulations.", Nucl. Instrum. Meth. A **336** (1993) 499.

[32] B. Andrieu *et al.*,"Electron / pion separation with the H1 LAr calorimeters.", Nucl. Instrum. Meth. A **344** (1994) 492;

B. Andrieu *et al.*,"Beam tests and calibration of the H1 liquid argon calorimeter with electrons.", Nucl. Instrum. Meth. A **350** (1994) 57.

[33] H. P. Wellisch, J. P. Kubenka, H. Oberlack and P. Schacht, "Hadronic Calibration Of The H1 Lar Calorimeter Using Software Weighting Techniques.",

[34] J. Gayler, "Improvement of Resolution in Non-Compensating Calorimeter by Energy Weighting.", H1 internal note, H1-05/85-019, 1985.

[35] B. Andrieu *et al.*,"Results from pion calibration runs for the H1 liquid argon calorimeter and comparisons with simulations.", Nucl. Instrum. Meth. A**336** (1993) 499.

[36] V. Shekelyan, H1 internal report, H1-01/93-288.

[37] M. Fleischer, "The performance of the H1 liquid argon calorimeter.", DESY-98-005A One of three related talks included in DESY-98-005 and given at the 7th International Conference on Calorimetry in High-Energy Physics (ICCHEP 97), Tucson, AZ, 9-14 Nov 1997 .

[38] R. D. Appuhn *et al.*,"Hadronic response and e/pi separation with the H1 lead/fibre calorimeter.", Nucl. Instrum. Meth. A **382** (1996) 395.

T. Nicholls *et al.*,"Performance of an electromagnetic lead / scintillating fiber calorimeter for the H1 detector.", Nucl. Instrum. Meth. A **374** (1996) 149.

[39] Z. q. Zhang, "New insights into the proton structure with e p collider HERA.", Habilitation Thesis (2000).

[40] S. Burke, R. C. W. Henderson, S. J. Maxfield, J. V. Morris, G. D. Patel, D. P. C. Sankey and I. O. Skillicorn, "Track finding and fitting in the H1 forward track detector.", Nucl. Instrum. Meth. A **373** (1996) 227.

[41] H1 Collaboration, "Technical Proposal to Build Silicon Tracking Detectors for H1.", DESY Internal Report **PRC-92-01** (July 5, 1992).

[42] S. Levonian, A. Panitsch, H1 internal report, **H1-09/95-454 (1995)**.

[43] J. C. Bizot *et al.*, "Status of Simulation for a Topological Level 2 Trigger.", H1 Internal Note, **H1-IN-212 (02/1992)**;

J. C. Bizot *et al.*, "Strategy Studies for the H1 Topological Level 2 Trigger (L2TT).", H1 Internal Note, **H1-IN-508 (01/1997)**.

[44] J. H. Köhne *et al.*, "Realisation of a Second Level Neural Network Trigger for the H1 experiment at HERA.", H1 Internal Note, **H1-IN-509 (01/1997)**.

[45] H1 Collaboration, "A Fast Track Trigger with High Resolution for H1.", DESY Internal Report, **PRC-99-06**;

Y. H. Fleming, "The H1 first level fast track trigger.", Thesis (2003).

[46] H1 Collaboration, "ep Physics Beyond 1999.", H1 Internal Note, **H1-IN-531 (10/1997)**.

[47] T. Carli *et al.*, H1 Internal Report, **H1-07/95-445**.

[48] S. Eichenberger *et al.*, "A fast pipelined trigger for the H1 experiment based on multiwire proportional chamber signals.", Nucl. Instrum. Meth. A **323** (1992) 532.

[49] J. Riedlberger, H1 Internal Report,**H1-01/95-419**.

[50] T. Sjostrand and M. Bengtsson, "The Lund Monte Carlo For Jet Fragmentation And E+ E- Physics: Jetset Version 6.2.", Comput. Phys. Commun. **39** (1986) 347.

[51] B. Andersson, G. Gustafson, G. Ingelman and T. Sjostrand, "Parton Fragmentation And String Dynamics.", Phys. Rep. **97** (1983) 31.

[52] H1 Collaboration;S. Aid *et al.*, "Guide to Simulation Program, H1SIM.", H1 Internal Report (1995).

[53] R. Brun, F. Bruyant, M. Maire, A. C. McPherson and P. Zanarini, "Geant3.", CERN-DD/EE/84-1

[54] G. A. Schuler and H. Speisberger, Proc. of the Workshop 'Physics at HERA', Vol. 3, DESY (1992) 1419.

[55] A. Kwiatkowski, H. Spiesberger and H. J. Mohring, "Heracles: An Event Generator For E P Interactions At Hera Energies Including Radiative Processes: Version 1.0.", Comput. Phys. Commun. **69** (1992) 155.

[56] L. Lonnblad, "ARIADNE version 4: A Program for simulation of QCD cascades implementing the color dipole model.", Comput. Phys. Commun. **71** (1992) 15.

[57] G. Gustafson and U. Pettersson, "Dipole Formulation Of QCD Cascades.", Nucl. Phys. B **306** (1988) 746.

[58] B. Andersson, G. Gustafson, L. Lonnblad and U. Pettersson, "Coherence Effects In Deep Inelastic Scattering.", Z. Phys. C **43** (1989) 625.

[59] B. Andersson, G. Gustafson and L. Lonnblad, "Gluon Splitting In The Color Dipole Cascades.", Nucl. Phys. B **339** (1990) 393.

[60] C. Adloff *et al.*,"Measurement of neutral and charged current cross-sections in positron proton collisions at large momentum transfer.", Eur. Phys. J. C **13** (2000) 609

[61] T. Sjostrand, L. Lonnblad, S. Mrenna and P. Skands, "PYTHIA 6.3 physics and manual.";

T. Sjostrand, "The PYTHIA and JETSET programs.", Prepared for Particles & Fields 92: 7th Meeting of the Division of Particles Fields of the APS (DPF 92), Batavia, Illinois, 10-14 Nov 1992;

T. Sjostrand, "High-energy physics event generation with PYTHIA 5.7 and JETSET 7.4.", Comput. Phys. Commun. **82** (1994) 74.

[62] M. Glück, E. Reya and A. Vogt, "Photonic parton distributions.", Phys. Rev. D **46** (1992) 1973.

[63] M. Erdmann, DESY preprint 96-090, 1996

[64] A. Courau and P. Kessler, "QED Compton scattering in high-energy electron - proton collisions.", Phys. Rev. D **46** (1992) 117.

[65] S. P. Baranov, O. Duenger, H. Shooshtari and J. A. M. Vermaseren, "LPAIR: A generator for lepton pair production.";

S. Baranov *et al.*, Proc. of the Workshop 'Physics at HERA', Vol. 3, DESY (1992) 478

J. A. M. Vermaseren, "Two Photon Processes At Very High-Energies.", Nucl. Phys. B **229** (1983) 347.

[66] U. Baur, J. A. M. Vermaseren and D. Zeppenfeld, "Electroweak vector boson production in high-energy e p collisions.", Nucl. Phys. B **375** (1992) 3.

[67] M. Rudowicz, "Algorithmen zur Kalorimetersimulation mit parametrisierten Schauern am Beispiel des H1-Detektors (In German).", Diploma, MPI Munich (1989).

[68] S. Bentvelsen, J. Engelen and P. Kooijman, "Reconstruction of (x, Q**2) and extraction of structure functions in neutral current scattering at HERA.", NIKHEF-H-92-02.

[69] A. Blondel and F. Jacquet, Proc. of the "Study of an *ep* Facility for Europe.", ed. U. Amaldi, DESY 79/48 (1979) 391.

[70] S. Bentvelsen *et al.*, Proc. of the Workshop "Physics at HERA" vol. 1, eds. W. Buchmüller and G. Ingelman, DESY (1992) 23.

[71] U. Bassler and G. Bernardi, "On the kinematic reconstruction of deep inelastic scattering at HERA: The Sigma method.", Nucl. Instrum. Meth. A **361** (1995) 197.

[72] B. Heinemann, "Measurement of Charged Current and Neutral Current Cross Sections in Positron-Proton Collisions at sqrt(s)=300 GeV." Thesis (1999).

[73] U. Bassler and G. Bernardi, "Structure function measurements and kinematic reconstruction at HERA.", Nucl. Instrum. Meth. A **426** (1999) 583.

[74] P. Bruel, "Recherche d'interactions au-delà du Modèle Standard à HERA (In French)." Thesis (1998).

[75] A. Dubak, "Measurement of the e+p Neutral Current DIS Cross Section and the F2, FL, xF3 Structure Functions in the H1 Experiment at HERA.", Thesis, MPI Munich (2003).

[76] C. Wissing, "Entwicklung eines Simulationsprogramms und Implementierung schneller Spurfitalgorithmen fuer den neuen H1-Driftkammertrigger (In German).", Thesis (2003) .

[77] E. Cabert *et al*,H1 internal note, H1-1198-556.

[78] B. Reisert, "Elektron-Proton-Streuung bei hohen Impulsuebertraegen am H1-Experiment (In German).", Thesis, MPI Munich (2000).

[79] J.Rauschenberger, "Prozesse des geladenen Stromes in tief-unelastischer Positron-Proton Streuung bei HERA (In German).", Thesis, Hamburg University (2002).

[80] A. L. Kataev, A. V. Kotikov, G. Parente and A. V. Sidorov, "Next to next-to-leading order QCD analysis of the 'old' CCFR data for xF3 structure functions of the deep inelastic neutrino - nucleon scattering." *Published in the Proceedings of the 3rd International Conference on Renormalization Group 96, Dubna, Russia, 26-31 Aug 1996. Edited by D.V. Shirkov, DI. Kazakov, V.B. Priezzhev. Dubna, 1997. pp. 209-223*;

A. L. Kataev, A. V. Kotikov, G. Parente and A. V. Sidorov, "Next-to-next-to-leading order QCD analysis of the 'old' CCFR data for xF3 and F2 structure functions of the deep-inelastic neutrino nucleon scattering: The brief discussion," *Prepared for 9th International Seminar on High-energy Physics: Quarks 96, Yaroslavl, Russia, 5-11 May 1996.*

[81] H1 Collaboration, "*ep* Physics beyond 1999.", H1 Internal Note H1-10/97-531 (1997).

[82] H1 Polarization 2000 Group, "Polarization 2000.", DESY Internal Report, **PRC-98-07**.

[83] M. Klein and T. Riemann, "Electroweak Interactions Probing The Nucleon Structure.", Z. Phys. C **24** (1984) 151.

[84] M. Klein, "Future deep inelastic scattering with HERA and THERA.", *Prepared for 9th International Workshop on Deep Inelastic Scattering (DIS 2001), Bologna, Italy, 27 Apr - 1 May 2001.*

[85] O. Henshaw, "A First Measurement of the Neutral Current Polarised Cross Section.", THESIS (In production).

[86] H1 Collaboration, "First Measurement of the Polarised Dependence of the Total Charged Current Cross Sections.", *H1 Preliminary.*

"This isn't right. This isn't even wrong."
- Wolfgang Pauli(1900-1958)

The truth is rarely pure and never simple.
- Oscar Wilde, The Importance of Being Earnest, 1895, Act I

Acknowledgements

This PhD would never have been possible without a crack team of supervisors led by Eram Rizvi (who bore the brunt of it), with the help of Paul Thompson (who supervised the writing of the thesis, much to his chagrin) and Paul Newman (who went on record as being my supervisor). Paul Newman is also responsible for inspiring me to do this PhD in the first place, if it wasn't for him I'd probably be a rich accountant by now.

As an EU student I got as many groups (partially) funding me as I had supervisors. I am thankful to PPARC for meeting my tuition fees ($\sim$10000 pounds), the University of Birmingham for funding my yearly grant (totalling $\sim$ 25000 pounds over the three years) and finally RAL/CLRC for covering my LTA and frequent STA costs, I could never have completed the PhD without all that time in Hamburg, and they easily matched the University's costs pound for pound.

Additional "supervision" was provided by the esteemed Drs Laycock and South, who mostly managed to stay calm at my goldfish like lack of comprehension when it came to C++ (and yes, I have still not had a single course on the subject). Andy Mehta and Nick Malden also crossed the university divide to provide much needed RA assistance, thanks Nick for letting me play with the FMD (you fool).

Thank you Bob Olivier for giving me an active role in the Data Quality group and not letting me leave the office before 2am. Arnd Specka was a king amongst group leaders and one of the few who can get confused as to which language he should be speaking (fluently might I add). Emmanuel Sauvin gets an honorary mention for not understanding Arnd.

Matts Beckingham and Lightwood are responsible for introducing me to Rugby, bringing me to a Potato Bar and a first-hand experience of time dilation, I'll miss you crazy guys! The brace of Yves provided a nice Benelux safety net to my stay in Birmingham, thanks to them I looked upbeat and dynamic. The crew from the years below are also responsible for keeping me sane and giving me an over-inflated sense of self-importance; in no particular order Aweys, Mudi, Andy_R, Carl Chris and Christian, thank you. Oliver "The Boy" gets special mention for an office "musical mufti day" that degraded into a period of mutually assured destruction at 4 am, the morning of an important presentation.

Craig and Karen-Bert gave me a place to stay for my first few months back in the UK, and then redecorated once I left (got something you want to tell me?). The Barrettyman let me take over his home (and broadband connection) while he worked in London, thanks! A big heads up to Luke, Charlotte, Little James, Bert(Michael), Sarah, Jaffa "The Cat", Rory "The Crusher" Clarke, Steve "Go into the Light" Bull, Uncle Dan, Auntie Sarah, Mark and Kit for still being there after two years in Hamburg.

I would never have gone through with a PhD if it hadn't been for the great 4 years as an undergraduate, and for this I have to thank the Boys from Rookery road: Dave, Dom, John and Mad Alan. I was blessed with numerous excellent teachers, but special mention goes to Alisdar Ray who was a tutor as well as (repeatedly) a Lecturer (a perfect lecturer, if it wasn't for his ns and ms ... and corrections to the corrections of the corrections of his

handouts). A masked lecturer gets an anonymous mention for courageously comparing the Higgs theory to that of Ether, you know who you are and someone had to do it. Terry Sloan gets an honorary mention for many a back of the envelope calculation in Hamburg, good luck listening for neutrinos, a pity you'll never be able to tell us if you do "for reasons of national defence". The last Physics "heads up" goes to Dr Ratcliffe, a devotee of Richard Feynman who taught me Physics at the European School. His enthusiasm propelled me into Physics and I'd probably be a lawyer or biologist now if it wasn't for him - you never forget a good teacher.

Finally my family were there throughout, be it Mom, Papa, Eric, Léo, les Woehrlings d'Alsace et du Quebec, the Arizona Simons (pronounced Haertala), the people I adopted (aunt Moe, die Spoeris et les Poncins to name a few), or the Huggins/Wrights. A big hello to the latest additions Sophie, Jon, Eve, Saul and James-Dahvin.

Finally, and most importantly, thanks to Liz for putting up with months of absence, three years of separation and still being there at the end. That wasn't fun, let's not do it again.

This thesis is dedicated to Eileen and John, Eve, Saul and James-Dahvin and to the memory of Christine, Dot and Lea.